Indian Institute of Science Education & Research Pune

Magnetism in Non-Magnetic Materials

by

Kshitij Narendra Karanjekar

A thesis submitted in fulfillment of the requirements for
the degree of Master of Science

under supervision of

Prof. A. Sundaresan
Professor, Chemistry & Physics of Materials Unit
Jawaharlal Nehru Centre of Advanced Scientific Research

Dedicated to my Parents.

You’ve never left the existence ***before nor will in the future. The one who leaves is somebody else; the body leaves*** *it’s* ***just an encapsulation, mind too leaves its microencapsulation. In between these two, there resides a master who never takes birth and never leaves the existence; he is eternal.***

- Osho

Certificate

This is to certify that this dissertation entitled "**Magnetism in Non-magnetic materials**" towards the partial fulfilment of the BS-MS dual degree programme at the Indian Institute of Science Education and Research, Pune represents study/work carried out by "Kshitij Narendra Karanjekar at Jawaharlal Nehru Centre of Advanced Scientific Research" under the supervision of "Prof. A Sundaresan, Professor, Chemistry and Physics of Materials Unit" during the academic year 2018-2019.

Kshitij N. Karanjekar

Prof. A. Sundaresan

(Research Supervisor)

Declaration

I hereby declare that the matter embodied in the report entitled "Magnetism in Non-Magnetic Materials" are the results of the work carried out by me at the Chemistry & Physics of Materials Unit, Jawaharlal Nehru Centre of Advanced Scientific Research, under the supervision of Prof. A Sundaresan and the same has not been submitted elsewhere for any other degree.

Kshitij N. Karanjekar

Prof. A. Sundaresan

(Research Supervisor)

Acknowledgements

- First of all, I am grateful to Prof. A. Sundaresan for giving me the golden opportunity to work under his supervision. I am thankful for the precious time that he has given me for planning & executing the studies throughout the project. The freedom he gives to the students is to be appreciated. His immense knowledge of the subject & calmness in character inspires me a lot and will continue to do so in the future.
- Many thanks to Prof. Sean Langridge ISIS, UK for SANS measuerments.
- I am grateful to my parents who raised me to see this point in my life.
- Prof V. Nagaraja, President (JNCASR) for approving my stay at JNCASR.
- JNCASR for providing the good research environment.
- Sincere thanks to Prof. C.N.R. Rao & Prof. Eswaramoorthy for their lab facilities.
- Sincere thanks to my co-supervisor Mr. Ravishankar P. N. who helped me consistently in the work carried out throughout the period of nine months.
- I would like to thank all my lab mates Mr. Abhijit, Mr. PremaKumar, Ms. Pavitra, Mr. Ravishankar, Mr. Debendra, Ms. Swarnamayee, Dr. Chandriah, Dr. Shivani, Ms. Sanchayita & Dr. Chandan for their constant help and suggestions.
- Many thanks to Mr. Bibekananda, Mr. Subramanyam, Dr. Shivanna, Mr. Mehraj, Ms. Surishi, Ms. Nijita, Ms. Soumita, Ms. Nijita, Ms. Suchismita, Ms. Divya, Mr. K.P. Sonu, Mr. Arunava, Mr. Momin, Mr. Dheeraj, Dr. Sreedhara, Ms. Manaswee, Mr. Mohd. Ayyub, Mr. Anand, Mr. Reetendra, Dr. K Pramoda, Dr. K Manjunath & Mr. Rohit for helping me with the instruments.
- Dr. Surjeet Singh for his valuable suggestions.
- Sincere thanks to Mr. Sudheer Kumar, Dr. Jitendra Kumar from IISER Pune for their constant moral support.
- Mr. Anil & Mr Vasu for XRD photoluminescence & FT-IR measurements.
- Mr. Rahul & JEOL TEM 2100 PLUS and ZEISS Gemini 500 FESEM facilities at AMRL
- I am also thankful to my batch mates Mr. Shilbhushan Shambharkar, Mr. Gaurav Joshi & Mr. Sandeep Joy for their immense help.

Table of Contents

Chapter 1: Introduction.

Chapter 2: Sol gel Synthesis.

Chapter 3: Experimental Techniques.

Chapter 4: Synthesis of SiO_2 Nanoparticles.

Chapter 5: Synthesis of doped SiO_2 Nanoparticles.

Chapter 6: Magnetism in $BaTiO_3$.

Chapter 7: Conclusion & Outlook.

List of figures

List of tables

Abstract

The origin of magnetism in otherwise nonmagnetic materials sounds interesting. Prof. Sundaresan et al. have already shown that the ferromagnetism exists in nanoparticles of MgO, GaN, CdS, Al_2O_3, ZnO, CeO_2, In_2O_3, SnO_2, etc. due to defects on their surface. In this project, the main focus is on SiO_2 & $BaTiO_3$. SiO_2 is the most abundant oxide on the earth and biocompatible as well so if we can induce magnetism in it; it can be extensively used (instead of other nonbiocompatible magnetic particles) in biomedical applications while $BaTiO_3$ nanoparticles can also be used as vectors in nanomedicine.

In this project, we have successfully synthesized $BaTiO_3$ nanoparticles and different phases of SiO_2 nanoparticles. Different characterizations such as SQUID, photoluminescence and small angle neutron scattering (SANS) were essential for understanding the origin of ferromagnetism. The highest magnetic moment obtained was 0.006 emu/g in both SiO_2 & $BaTiO_3$. SANS data of $BaTiO_3$ shows that ferromagnetism indeed is coming from the surface oxygen vacancies. The reduction of magnetic moment after annealing in the air also shows that oxygen vacancies are primary source of ferromagnetism.

Chapter 1: Introduction.

1.1 Introduction.

Ferromagnetism in conventional materials arises due to the presence of unpaired electrons. However, recently it is evident that even in the absence of such unpaired electrons various oxides, nitrides, and chalcogenides (e.g.: CeO_2, Al_2O_3, NbN, CdS, etc.) show ferromagnetism at room temperature [1-3]. In the case of oxides, it has been established that only the nanoparticles behave ferromagnetically, their bulk counterpart being diamagnetic [2]. The source of the ferromagnetism has been postulated due to exchange interactions between localized electron spin moments. This might be due to the influences of the oxygen vacancies at the surface of nanoparticles [4]. However, this case should not be confused with that of dilute magnetic oxides which are wide bandgap materials that become ferromagnetic only when doped with cation having partially filled d orbital [5]. The ferromagnetism shown by thin films of HfO_2 is speculated to be a consequence of lattice defects and oxygen vacancies (induced due to preparatory conditions), and since neither Hf^{4+} nor O^{2-} are magnetic the ferromagnetism is termed as d^0 ferromagnetism [6]. These types of materials can find their application in spintronics. Spintronics is the area in which along with the charge dependent electronics, spin degree of freedom can also be utilized to facilitate the manufacture of high-end devices with the increased speed of data processing and low electric power consumption [7]. The ferromagnetism observed in CaB_6 even though the constituent atoms Ca & B are nonmagnetic is surmised to be due to defects which may have formed during the synthesis of CaB_6[8]. The ferromagnetism in CaB_6 was speculated to be due to Fe based impurities which may be in the phase of Fe-B [9]. But the studies done in the single crystalline CaB_6 with a couple of different purities of Boron has ruled out the fact that the ferromagnetism is originated from Fe based impurities [10]. The role played by these surface oxygen vacancies of nanomaterials in their origin of ferromagnetism and how it differs from conventional ferromagnetic materials is to be understood in great detail.

The oxide of current interest is SiO_2. The possibility of magnetic properties in the SiO_2 may open new avenues in spintronics as well as in the field of Nano medicine. The biological applications of SiO_2 are high of interest because of its biocompatibility. It is a consensus that the properties of nanoparticles are very much different than their bulk counterparts. Similar is the case with silica. The magnetic nanoparticles which have high saturations (i.e., up to 80 emu/g) are required for the Magnetic Resonance(MR) contrast agents for MR diagnosis of cancer [11]. The Fe_3O_4 nanocrystals have already been observed as good intracellular labeling agents and good MR trackers [12].

The magnetic materials with high magnetic saturations and their oxides are considered mainly for therapeutic applications [11]. In biomedical applications the Nano phase is always preferred, because of smaller size it is easier for nanomaterials to travel in veins and arteries. But along with having benefits of Nano level dimensions, there is a probability of these particles getting penetrated through membranes only to pass through the bloodstream to other organs [13]. Fe_3O_4 nanoparticles are found to induce an inflammation, cellular poisoning and respiratory damage [13]. So the magnetic materials in such applications are required to be biocompatible. SiO_2 nanoparticles can be better candidates for such biomedical applications due to their biocompatibility. Experimental studies on the effects of SiO_2 upon cellular uptake doesn't show any cytotoxic activity up to 2.5nM of concentration [14]. While the mesoporous silica (silica containing the high specific surface area and pores) are effective in drug delivery [15], So these SiO_2 nanoparticles if made somehow magnetic then they can replace the otherwise toxic materials in biomedical applications such as hyperthermia, MR labeling agents, magnetic separation of biological molecules, cell labeling, drug carriers, radionuclide and gene delivery as well as tissue engineering and magnetic bio sensing [16].

But as is known that the commercial pyrogenic SiO_2 Nano powder (NP) is diamagnetic [17]. But the synthesis of various phases of SiO_2 can be carried out to explore the possibilities of magnetic properties. Nano powders produced by Vladislav et al. shows d0 magnetism [17]. The studies which were done by Gregory Kopnov et al. have shown that the etching of the silicon wafers by HF and KOH have shown relatively large magnetic moment. Their studies suggest that the magnetism is co-related to surface roughness; the exact correlation is unknown. The precise mechanism of this magnetism is currently an open question [18]. But there is another phase of SiO_2 which is that of SiO_2 Nano spheres which are also shown to exhibit weak ferromagnetism. The hole-bridge structures of which were obtained by etching the already sintered Nano spherical array with HF. In the work of Xing Wang et al. the origin of weak ferromagnetism in this phase was assumed to be none other than oxygen vacancies. They have speculated that HF-etching may have contributed to weak ferromagnetism in these Nano spherical arrays [19].

Another oxide of interest is $BaTiO_3$. The nanoparticles of which show ferromagnetic order and also hold a promising future in the biomedical field [20-21].

In this project, the synthesis of $BaTiO_3$ nanoparticles & various phases of SiO_2 nanoparticles will be carried out. The characterization of which will be done by XRD. The size and shape will be studied using scanning electron microscopy(SEM). The magnetic moment will be measured with SQUID.

References

1. Sundaresan et al. Ferromagnetism as a universal feature of nanoparticles of the otherwise nonmagnetic oxides Phys. Rev. B 74, 161306.
2. A. Sundaresan and C. N. R. Rao Ferromagnetism as a universal feature of inorganic nanoparticles Nanotoday 4, 96- 106.
3. Nitesh Kumar, D. Sanyal and A. Sundaresan, Defect induced ferromagnetism in MgO nanoparticles studied by optical and positron annihilation spectroscopy Chem. Phys. Lett., 477, 360 – 364.
4. Sundaresan et al.Ferromagnetism as a universal feature of nanoparticles of the otherwise nonmagnetic oxidesPHYSICAL REVIEW B 74, 161306R 2006.
5. J.M.D. CoeyDilute magnetic oxidesCurrent Opinion in Solid State and Materials ScienceVolume 10, Issue 2, April 2006, Pages 83-92.
6. Nguyen Hoa Hong Magnetism due to defects/oxygen vacancies in HfO2 thin films phys. stat. sol. (c) 4, No. 3, 1270–1275 (2007)
7. Tian et al. Oxide nanowires for spintronics: materials and devices Nanoscale, 2012,4, 1529-1540.
8. Lofland et al. Defect driven magnetism in calcium hexaboridePHYSICAL REVIEW B 67, 020410® (2003)
9. Matsubayashi et al. Extrinsic Origin of High-Temperature Ferromagnetism in CaB_6Journal of the Physical Society of Japan, 72(8), 2097–2102. doi:10.1143/jpsj.72.2097
10. Jong-Soo Rhyee and B. K. Cho The effect of boron purity on electric and magnetic properties of CaB6 Journal of Applied Physics, 95(11), 6675–6677.
11. Huh et al. In Vivo Magnetic Resonance Detection of Cancer by UsingMultifunctional Magnetic NanocrystalsJournal of the American Chemical Society, 127(35), 12387–12391.

12. Song et al. (2005). Surface Modulation of Magnetic Nanocrystals in the Development of Highly Efficient Magnetic Resonance Probes for Intracellular Labeling. Journal of the American Chemical Society, 127(28), 9992–9993.
13. Hurbankova et al. Respiratory toxicity of Fe_3O_4nanoparticles: experimental studyReviews on Environmental Health, 32(1-2).
14. Malvindi, M. A., Brunetti, V., Vecchio, G., Galeone, A., Cingolani, R., &Pompa, P. P. (2012). SiO_2nanoparticles biocompatibility and their potential for gene delivery and silencing. Nanoscale, 4(2), 486–495.
15. Wang, Y., Zhao, Q., Han, N., Bai, L., Li, J., Liu, J., … Wang, S. (2015). Mesoporous silica nanoparticles in drug delivery and biomedical applications. Nanomedicine: Nanotechnology, Biology and Medicine, 11(2), 313–327.
16. Pankhurst, Q. A., Connolly, J., Jones, S. K., & Dobson, J. (2003). Applications of magnetic nanoparticles in biomedicine. Journal of Physics D: Applied Physics, 36(13), R167–R181.
17. Il'ves, V. G., Zuev, M. G., &Sokovnin, S. Y. (2015). Properties of Silicon Dioxide Amorphous Nanopowder Produced by Pulsed Electron Beam Evaporation. Journal of Nanotechnology, 2015, 1–8.
18. Kopnov, G., Vager, Z., &Naaman, R. (2007). New Magnetic Properties of Silicon/Silicon Oxide Interfaces. Advanced Materials, 19(7), 925–928.
19. Wang, X., Zhen, C., Liu, X., Liu, X., Li Ma, Pan, C., &Hou, D. (2014). A new hole-bridge structure based on a SiO2 nanoarray and its ferromagnetism. Colloids and Surfaces A: Physicochemical and Engineering Aspects, 446, 151–155.
20. Mangalam, R. V. K., Ray, N., Waghmare, U. V., Sundaresan, A., & Rao, C. N. R. (2009). Multiferroic properties of nanocrystalline BaTiO3. Solid State Communications, 149(1-2), 1–5.
21. Genchi et al. Barium titanate nanoparticles: promising multitasking vectors in nanomedicine

Chapter 2: Sol-Gel Synthesis.

2.1 Background.

Since in this thesis we are mainly concerned about nanoparticles we will discuss general methods of synthesis of nanoparticles. There are two main approaches which are top-down & bottom-up approaches [1-2] former being costlier than the latter. In the bottom-up approach the atoms or molecules are allowed to self-assemble naturally or through an externally driven force in a chemical reaction to form more organized Nano structures while in top-down approach starting with a larger piece finer and finer structures are made by using various tools and methods [2]. Here we are mainly concerned about the bottom-up approach that too particularly sol-gel and precipitation methods.

2.2 Bottom-up approach.

The bottom-up approach is again divided into several methods such as molecular self-assembly, molecular beam epitaxy, sol-gel, etc. [3-13] In molecular self-assembly molecules are allowed to form definite structures naturally, i.e., without external driving force [14]. Molecular self-assembly is much more relevant to biological entities such as peptides & proteins and some extent to polymer science and materials engineering [15-16]. Molecular beam epitaxy is a layer by layer deposition of single crystals to form the thin film under very high vacuum [17]. It is used for the synthesis of single crystal thin films, quantum wells & superlattices [18]. Sol-gel synthesis is the novel method for synthesis of metal oxide nanoparticles or nanocomposites. It is novel as in it has control over the surface properties of as-synthesized nanoparticles [19]. It also is the favored method for studying surface modification by coating a layer, surface doping, coating with organic molecules, etc. [20-24].

2.3 Sol-gel method.

A sol-gel method is a method which uses a solution containing metal compounds such as metal alkoxides as a precursor for the oxide to be prepared, alcohol as a solvent, H_2O as a hydrolyzing agent, any acid or base as a catalyst [25]. A sol is generally referred to as solvent hosting colloidal particles. The process starts with a dissolution of metal precursors which is more often a ‘metal-alkoxide’ in a solvent to form a sol [26]. Except for metal alkoxides such as silicon alkoxide, hydrolysis of other metal precursors yields particulate materials rather than undergoing polymerization; hence much of the sol-gel works are based on silica glass & silica gels [27]. After formation of sol, gelling (formation of gel) takes place by polymerization which generally starts from the surface and proceeds in bulk [28]. So in the following three subsections, we’ll discuss three aspects of our reactions, i.e., hydrolysis, condensation, gelation & drying.

2.3.1 Hydrolysis.

There are two types of precursors generally used one is an aqueous solution of an inorganic salt, and other is a metal organic compound [29]. The most commonly used precursors are metal alkoxides given their high reactivity towards nucleophilic species such as H_2O [30]. When the metal cation is introduced as a salt in the water it is solvated by water molecules as shown below in fig 2.1; the electrons are transferred from the bonding orbitals of H_2O to the transition metal cation which creates a partial charge on H atom making the molecule acidic [29].

fig 2.1 Solvation of transition metal cation.

So, the following equilibrium exists which is dependent on charge transfer and in turn acidity of the H_2O molecule [29].

$$\mathbf{M[(OH)_2]^{z+} \leftrightarrow M[OH]^{(z-1)+} + H^{+} \leftrightarrow [M{=}O]^{(z-2)+} + 2H^{+}}$$

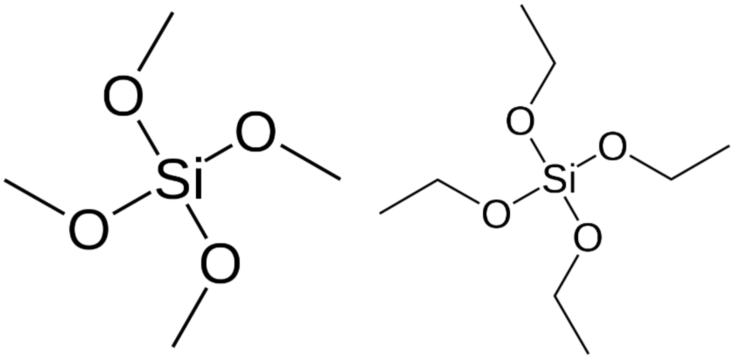

fig 2.2 The chemical structures of TMOS & TEOS respectively.

Precursors typically used for the synthesis of silica nanoparticles are tetramethyl orthosilicate (TMOS) and tetraethyl orthosilicate (TEOS) though we'll use TEOS as our main precursor. Both the reagents come under the category of silanes with four alkoxy groups attached to the Si atom as shown in fig 2.2. These precursors are generally soluble in organic solvents such as ethanol & methanol etc. here we've mostly stuck to the ethanol. The hydrolysis of silanes requires catalyst which is generally of two types acidic or basic, the reactions under both catalysts are shown in fig 2.3 & 2.4 respectively [30].

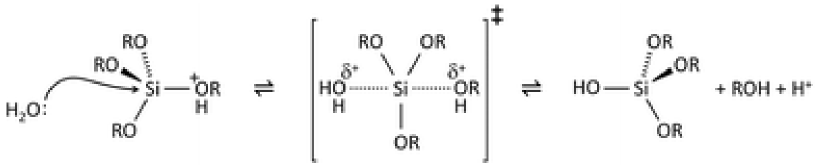

fig 2.3 Acid-catalyzed Hydrolysis.

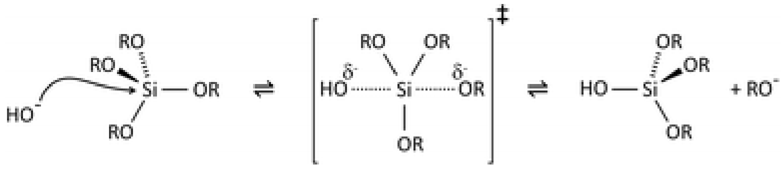

fig 2.4 Base-catalyzed hydrolysis.

2.3.2 Condensation.

Condensation can be proceeded by two modes either nucleophilic substitution (S_N) or nucleophilic addition (A_N) as following [25];

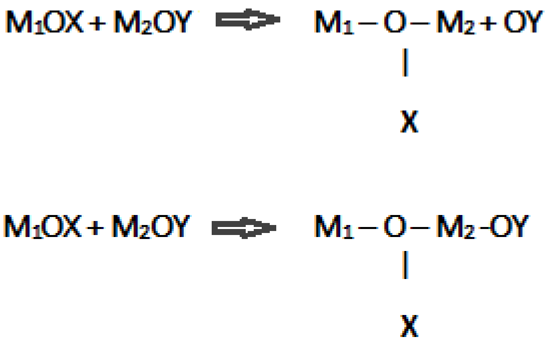

$$M_1OX + M_2OY \Rightarrow M_1-\underset{\underset{X}{|}}{O}-M_2 + OY$$

$$M_1OX + M_2OY \Rightarrow M_1-\underset{\underset{X}{|}}{O}-M_2\text{-}OY$$

fig 2.5 Condensation by S_N & A_N modes.

2.3.2.1 Oleation.

One of the ways by which condensation takes place is by the formation of hydroxyl bridge between two central metal atoms known as oleation [32]. One of the ways the oleation can take place is by the formation of H_3O_2 bridge (fig 2.6) [33-34].

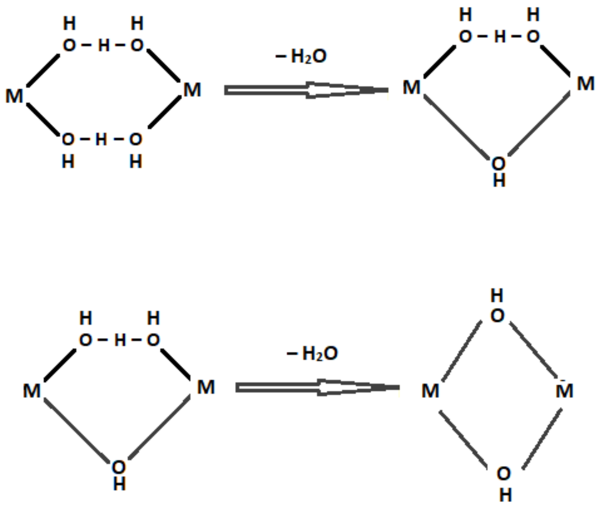

fig 2.6 Oleation by H3O2 bridge formation [25].

But this is not the only way by which the oleation occurs there are other ways too as shown in fig 2.7 [29,25,35] The rate of olation depends upon size, electronegativity & electronic configuration of metal cation M [36-38,52].

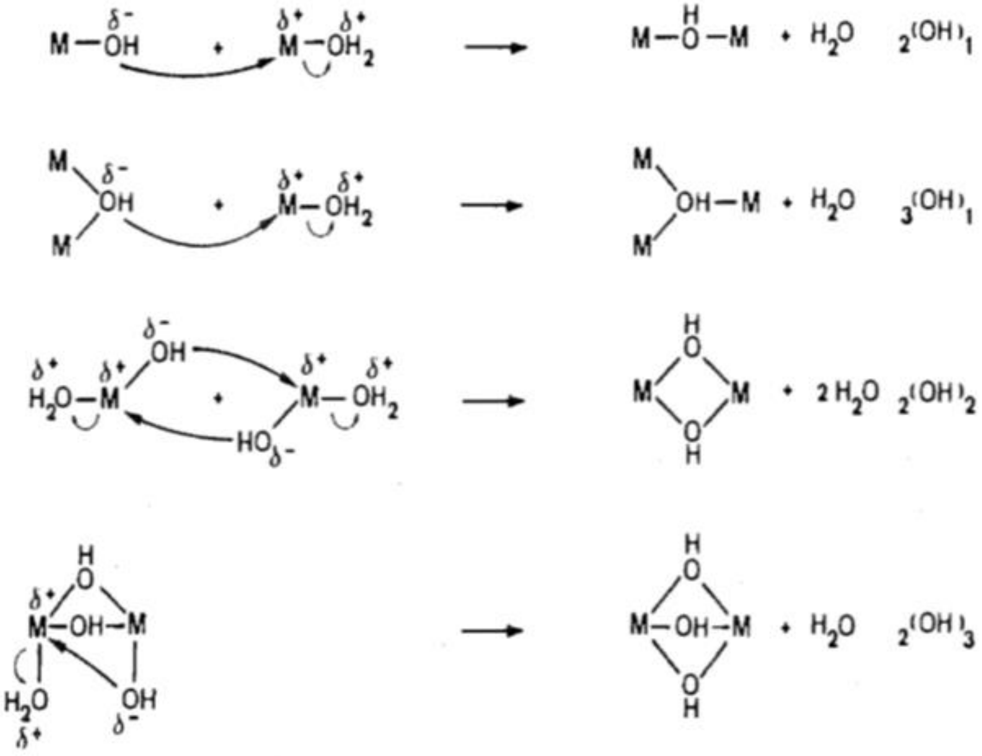

fig 2.7 Different mechanisms of Oleation [25].

2.3.2.2 Oxolation.

In oxolation, the bridge between two central metallic atoms is the -O- (oxo-) group. This type of reaction also takes place in two ways, i.e., S_N & A_N. Former is the case for coordinately saturated metals & latter is for coordinately unsaturated metals [39-41].

2.3.2.3 Condensation of silicates.

After hydrolysis the hydrolyzed silica interact with each other to form ≡ Si – O – Si ≡ bonds resulting in linkage [42] as shown below (fig 2.8);

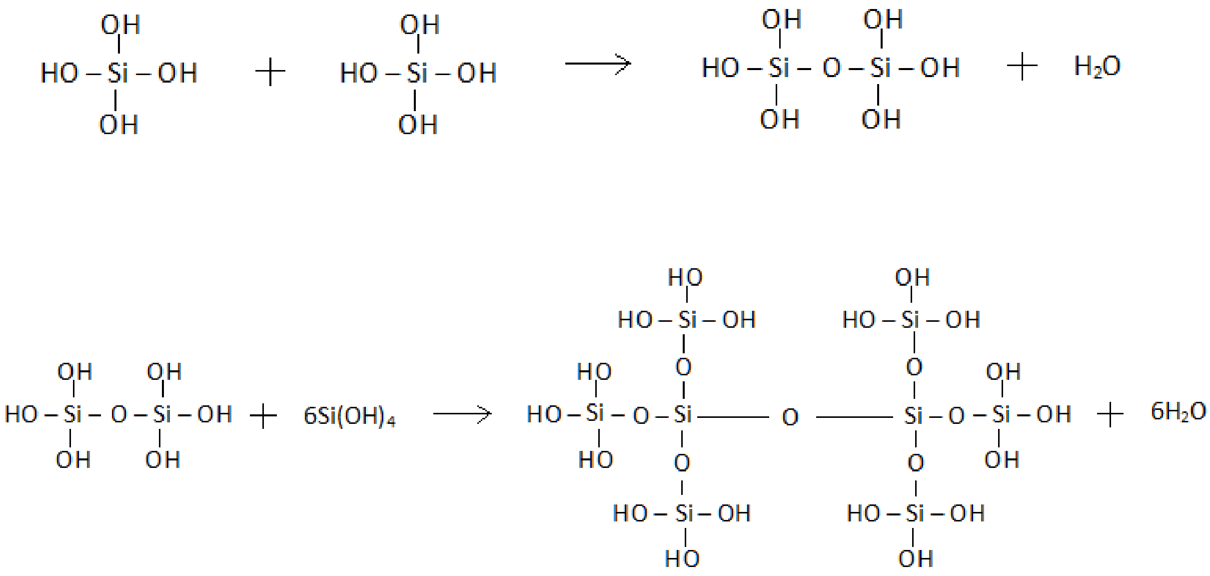

fig 2.8 Condensation.

Former reaction depicts the simplest condensation that can take place between two molecules while the latter shows the poly condensation. But it is not always the case since the silicates are most of the times never fully hydrolyzed (depending on catalyst), i.e., some – OR groups are still present so for such cases condensation takes place by producing alcohols (fig 2.9) [43].

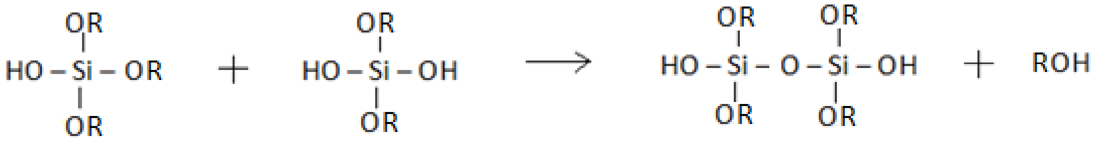

fig 2.9 Condensation.

2.3.3 Gelation & drying.

Gelation can be defined as a formation of a three-dimensional solid network (mostly polymer) in a fluid phase [31]. The turbidity of the solution increases gradually [44]. The simulation studies by using Brownian & Stokesian dynamics have shown that gelation time (t_g) depends on salt concentration & volume fraction of particles [45]. The former affects the gelation time but not the strength of the gel network [45]. Gelation time (t_g) is the time after which the semisolid leftover can bear stress elastically [42]. In the final process of drying the semisolid matter turns into solid also called as Xerogel [44]. After drying; the solid may or may not be calcined to obtain the final product.

2.4 SiO_2.

SiO_2 is an oxide of silicon also known as silica. It is the most abundant oxide on the earth. Silica constitutes 10% of the mass of the earth's crust in the form of crystalline quartz [46]. Silica is most abundant component of sand [47]. In the biological world, it is commonly found in shells of aquatic creatures, in plants and rice husk. It has a wide variety of uses. Almost 95% of commercial production of SiO_2 ends up in construction applications [46]. It is the main constituent of glasses. Silicones are polymers of $\equiv Si - O - Si \equiv$ (siloxane) groups. Silicones are used as coatings & insulators in electrical appliances due to their low thermal & electrical conductivity [46]. It is also used as a defoamer, oil, grease, rubber, dry cleaning solvent, firestop, in medicine particularly ophthalmology, mold making, etc.

Silica is mostly found in tetrahedral co-ordination with oxygen. Silica can be either crystalline or amorphous. Crystalline silica has 14 types of polymorphs. We'll mostly be concerned of amorphous SiO_2.

2.5 Synthesis of Silica Nanoparticles.

Silica nanoparticles were first prepared in 1956 by Kolbe by mixing TEOS in a solvent containing alcohol & water but they were agglomerated & the results were only observed for very pure reagents [48]. But after systematic study of the reaction parameters involved Stober et al. successfully synthesized silica nanoparticles even without using very pure reagents and thus inspired the silica sol-gel syntheses yet to come [49]. The work of Stober was mostly extended by Bogush et al. The Nano spherical SiO_2 particle size depends on multiple factors. It depends on the concentration of TEOS, NH_4OH, H_2O, reaction temperature as well as the ratio of ethanol and aqueous ammonia [50]. The studies have also shown that the average particle size goes through a maximum as a function of water concentrations as shown in figs 2.10 & 2.11 [51]. The maxima of these curves are a function of ammonia concentration.

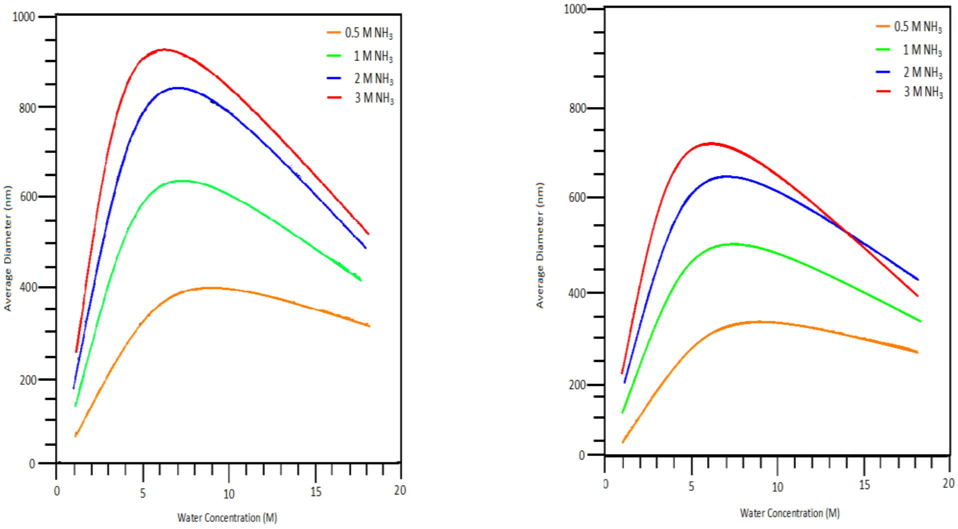

fig 2.10 Average diameter of as-synthesized SiO_2 nanoparticles as a function of water concentration at fixed 0.5,1,2,3 M concentrations of NH_3 & at fixed concentrations of 0.17 M & 0.3 M of TEOS respectively at temperature 298K.

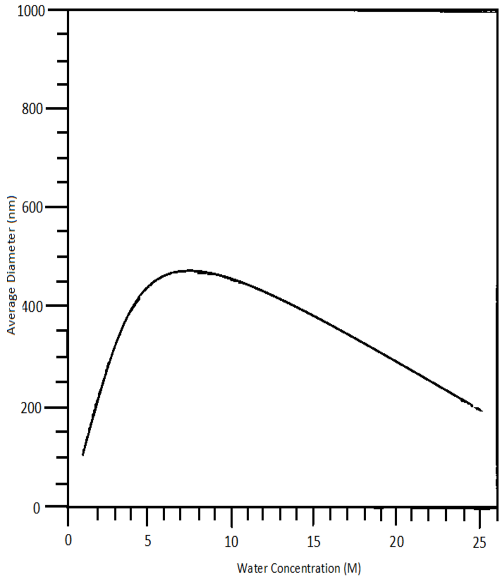

fig 2.11 Average diameter of SiO_2 nanoparticles as a function of water concentration at fixed concentrations, i.e., 0.17M & 1 M of TEOS & NH_3 respectively at 298K.

References

1. Wang et al. Bottom-Up and Top-Down Approaches to the Synthesis of Monodispersed Spherical Colloids of Low Melting-Point Metals Nano Letters 2004, 4, 10, 2047-2050.
2. Rosa et al. Top-down and Bottom-up approaches to nanotechnology.
3. Nan et al. Catalyzed assembly of the hollow silver-sulfide cluster through self-releasable anion template Communications Chemistry volume 1, Article number: 99 (2018).
4. Wang et al. Nanoribbons self-assembled from short peptides demonstrate the formation of polar zippers between ß-sheets Nature Communications volume 9, Article number: 5118 (2018).
5. Chan et al. C-Terminal Residue of Ultrashort Peptides Impacts on Molecular Self-Assembly Hydrogelation, and Interaction with Small-Molecule Drugs Scientific Reportsvolume 8, Article number: 17127 (2018).
6. Vauthey et al. Molecular self-assembly of surfactant-like peptides to form nanotubes and nanovesicles PNAS April 16, 2002 99 (8) 5355-5360.
7. Mandziak et al. Structure and magnetism of ultrathin nickel-iron oxides grown on Ru(0001) by high-temperature oxygen-assisted molecular beam epitaxy Scientific Reportsvolume 8, Article number: 17980 (2018).
8. Tchoe et al. Catalyst-free growth of InAs/InxGa1-1-xAs coaxial nanorod heterostructures on graphene layers using molecular beam epitaxy NPG Asia Materials volume 7, page 206 (2015).
9. Qu et al. Highly anisotropic P3HT films with enhanced thermoelectric performance via organic small molecule epitaxy NPG Asia Materials volume 8, page e292 (2016).
10. Lee et al. Dynamic layer rearrangement during growth of layered oxide films by molecular beam epitaxy Nature Materials volume 13, pages 879–883 (2014).
11. Yang et al. Sol–gel synthesis of TiO2 nanoparticles and photocatalytic degradation of methyl orange in aqueous TiO2 suspensions Volume 413, Issues 1–2, 9 March 2006, Pages 302-306.

12. Hasnidawani et al. Synthesis of ZnO Nanostructures Using Sol-Gel Method Volume 19, 2016, Pages 211-216.
13. Qiu et al. Synthesis of nanocrystalline GaN by the sol–gel method Volume 136, Issue 1, 15 January 2007, Pages 33-36.
14. Dahman, Y. (2017). Nanosensors**By Yaser Dahman, Amira Radwan, Boris Nesic, and Jason Isbister. Nanotechnology and Functional Materials for Engineers, 67–91.
15. Subramani, K., & Ahmed, W. (2012). Self-Assembly of Proteins and Peptides and Their Applications in Bionanotechnology and Dentistry. Emerging Nanotechnologies in Dentistry, 209–224.
16. Zhang, S. (2001). Molecular Self-assembly. Encyclopedia of Materials: Science and Technology, 5822–5828.
17. Alavi, K. (2001). Molecular Beam Epitaxy. Encyclopedia of Materials: Science and Technology, 5765–5780.
18. Shibasaki, I., & Kuze, N. (2013). Mass production of sensors grown by MBE. Molecular Beam Epitaxy, 697–720.
19. Rao, B. G., Mukherjee, D., & Reddy, B. M. (2017). Novel approaches for preparation of nanoparticles. Nanostructures for Novel Therapy, 1–36.
20. Mitra, A., & De, G. (2016). Sol-Gel Synthesis of Metal Nanoparticle Incorporated Oxide Films on Glass. Glass Nanocomposites, 145–163.
21. Muresan, L. M. (2015). Corrosion Protective Coatings for Ti and Ti Alloys Used for Biomedical Implants. Intelligent Coatings for Corrosion Control, 585–602.
22. Mojiri, H., & Aliofkhazraei, M. (2017). 3.19 Effect of Surface Roughness on Wetting Properties. Comprehensive Materials Finishing, 276–305.
23. Hou, P., Liu, B., Guo, Z., Zhou, P., Wang, B., & Zhao, L. (2019). Effect of Ho doping on the crystal structure, surface morphology and magnetic property of BiFeO3 thin films prepared via the sol-gel technology. Journal of Alloys and Compounds, 775, 59–62.
24. Grujic-Brojcin, M., Armakovic, S., Tomic, N., Abramovic, B., Golubovic, A., Stojadinovic, B. Šcepanovic, M. (2014). Surface modification of sol–gel synthesized TiO2 nanoparticles induced by La-doping. Materials Characterization, 88, 30–41.
25. Brinker, C. and Scherer, G. - 1990 - Sol-Gel Science_ The Physics and Chemistry of Sol-Gel Processing.

26. Sol-gel processes in glass science and technology Journal of Non-Crystalline Solids 42 (1980) 477-488.
27. D.P. Partlow and B.E. Yoldas colloidal versus polymer gels and monolithic transformation in glass-forming systems journal of non-crystalline solids 46 (1981) 153-161.
28. Masayuki Yamane, Shinji Aso*, Teruosakaino Preparation of a gel from metal alkoxide and its properties as a precursor of oxide glass journal of materials science 13 (1978) 865-870.
29. J. Livage, M. Henry and C. Sanchez sol-gel chemistry of transition metal oxides Prog. Solid St. Chem. Vol, 18, pp. 250341, 1988.
30. D.C. Bradley, R.C. Mehrotra and D.P. Gaur, Metal Alkoxides, Academic Press, London (1978).
31. A. E. Danks a, S. R. Hall b and Z. Schnepp The evolution of ‘sol–gel’ chemistry as a technique for materials synthesis Review Article Mater. Horiz., 2016, 3, 91-112.
32. The chemistry of the coordination compounds by Bailar, John C. (John Christian), 1904-1991.
33. M. Ardon & B. Magyar, J. Am. Chem. Soc., 106 (1984) 3359-3360.
34. M. Ardon, A. Bino, and K. Michelson, J. Am. Chem. Soc., 109 (1987) 1986-1990.
35. V. Baran, Coordin, Chem., 6 (1971) 65.
36. M Eigen, Pure Appl. Chem., 6 (1963) 97.
37. H. Kruger, Chem. Soc. Rev., 11 (1982) 227.
38. R.G. Pearson, J. Chem Educ., 38 (1961) 164.
39. M.L. Freedman, J. Am. Chem. Soc., 80 (1958) 2072.
40. D.L. Kepert, Prog. Inorg. Chem., 4 (1962) 199.
41. R.H. Tytko and O. Glemser, Adv, Inorg. Chem, Radiochem, 19 (1976) 239.
42. The Sol-Gel Process LARRY L. HENCH and JON K. WEST Chem. Rev, 1990, 90, 33-72.
43. Hydrolysis and condensation of silicates: Effects on Structure C.J. Brinker Journal of Non-Crystalline Solids 100 (1988) 31-50.
44. Characterization and Chemical Modification of the Silica Surface Edited by E.F. Vansant, P. Van Der Voort, K.C. Vrancken Volume 93, Pages 3-556 (1995).

45. Aggregation and Gelation of Silica Nanoparticles Cao, Xiujuan Publication Number: AAT 3481485; ISBN: 9781267006813; Advisor: Morris, Jeffrey F.
46. "Silica" Ullmann's Encyclopedia of Industrial Chemistry.
47. Berslien, Elisa (2012). An Introduction to Forensic Geoscience. Wiley & Sons. p. 138.
48. Das komplexchemische Verhalten der Kieselsa¨ure Thesis by Gerhard Kolbe 1956.
49. Controlled Growth of Monodisperse Silica Spheres in the Micron Size Range Werner Stober, Arthur Fink and Ernst Bohn, journal of colloid and interface science 26, 62--69 (1968).
50. Bogush, G.H., & Zukoski, C. (1991). Studies of the kinetics of the precipitation of uniform silica particles through the hydrolysis and condensation of silicon alkoxides. Journal of Colloid and Interface Science, 142(1), 1–18.
51. Bogush, G. H., Tracy, M. A., & Zukoski, C. F. (1988). Preparation of monodisperse silica particles: Control of size and mass fraction. Journal of Non-Crystalline Solids, 104(1).
52. C.F Baes and R.E. Mesmer, The Hydrolysis of Cations (Wiley, New York, 1976).

Chapter 3: Experimental Techniques.

3.1 Overview.

This chapter is dedicated to the understanding of different characterization techniques & working principle behind them. We'll mainly discuss x-ray diffraction (XRD), scanning electron microscopy (SEM), fourier transform infrared spectroscopy (FT-IR), photoluminescence spectroscopy (PL), and ultraviolet spectroscopy (UV).

3.2 X-ray diffraction (XRD).

XRD is a characterization technique which is extensively used in solid-state sciences. X-ray diffraction in crystals was first observed by Max Van Laue et al. [1] & the development of bragg equation as well as usage of this phenomenon to characterize the Zinc Blend structure was done by both W. H. Bragg & W.L. Bragg a father & son duo for which they were awarded Nobel prize for physics in 1915 [2]. On the electromagnetic spectrum, the range of wavelength from 0.01 nm to 10 nm is termed as x-ray. X-rays have a relatively high penetrating power as is evident for their application in medical imaging of bones [3]. When a charged particle decelerates it emits radiation, this radiation is often termed as bremsstrahlung. So in an XRD instrument, the high voltage is applied between cathode and anode, so the electrons upon being incident on anode decelerate and emit x-rays, above certain threshold voltage molybdenum will show two characteristic lines Kα & Kβ which are evident as two sharp peaks under the continuous background of bremsstrahlung [4-5]. The relation between the x-rays and the spacing between lattice planes is given by Bragg's law i.e.

$$n\lambda = 2d\ sin\theta$$

Where n is an integer, λ is a wavelength, d is interplanar distance, θ is the angle of diffraction. The more rigorous mathematical treatment by Max von Laue using reciprocal lattice is also equivalent to the Bragg's law but will not be discussed here. There are two main ways to produce electrons, one way is by ionization of the gas, and another way is by deceleration of electrons on the target by applying voltage [6]. As can be seen in fig 3.2 the target acts as an anode while

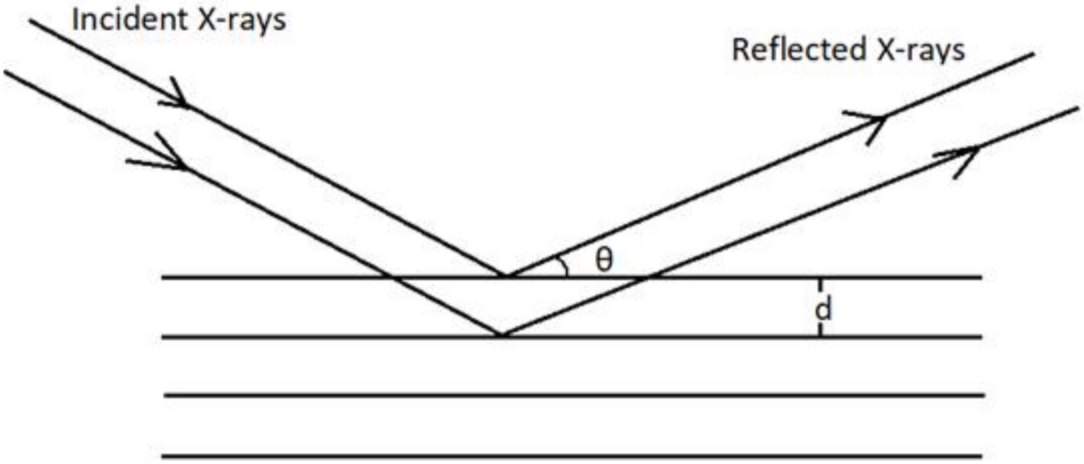

fig 3.1 Incident X-rays are diffracted from lattice.

there is a tungsten filament which acts as a cathode & is pumped with a current of 3 ampere to provide the heating for ejection of electrons while the target receives the electron [6]. The target gets heated so to cool it down water is flowed in an adjacent channel [6]. The x rays are scattered in all the directions and are used for the diffraction.

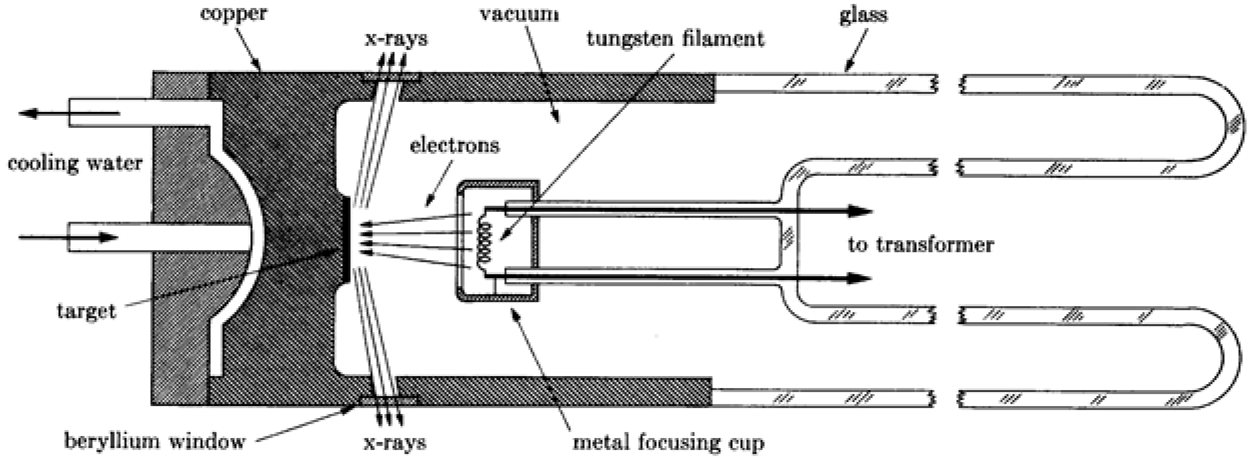

fig 3.2 Cross section of X-ray tube.

3.3 Scanning electron microscopy.

Scanning electron microscope (SEM) uses electrons to probe the microscopic structure of matter, unlike optical microscope which uses light radiation. The resolving power of SEM is higher because of the smaller wavelength associated with electrons (0.005 nm) rather than light (200-250nm) [7]. The electrons upon incidence on sample interact with it through various interactions which involve emission of photons as well as the scattering of electrons [8]. Among these, we will mainly discuss back scattered electrons and secondary emission of electrons. Secondary electron emission is the emission of the electron when radiation is incident on a metal surface which was first observed by Lenard et al. [9]. The secondary electrons (SE) are mainly the valence electrons that are inelastically scattered upon the impact of primary beam of electrons [10]. The secondary emission electrons are collected by a detector, and the topography of material is scanned and imaged on CRT display (nowadays LCD) [11]. The SE have energies which are usually less than 50 eV with mean free path approximately 1 nm [12]. The electrons which are emitted are not only SE but also the inelastically back scattered & elastically scattered, i.e., reflected electrons [12]. An Everhart-Thornley detector is used for detecting the secondary as well as back scattered electrons [13]. Everhart-Thornely detector is a cylindrical brass whose end is fitted with copper mesh with positive voltage so upon incidence the electrons are accelerated to this copper mesh only to find themselves incident on scintillator which gives rise to number of photons and these photons are incident on the photomultiplier tube which thanks to photoelectric effect gives rise to multiple electrons which are then raster scanned on cathode ray tube (CRT) [14]. But the instrument which we have used has an LCD. Fig 3.3 depicts the construction of the scanning electron microscope [15]. The electron gun emits the electrons which are to be accelerated by so-called electromagnetic lenses for focusing [16]. These electrons are incident on the specimen which is kept in high vacuum [17]. And the secondary electron detector collects the SE [18].

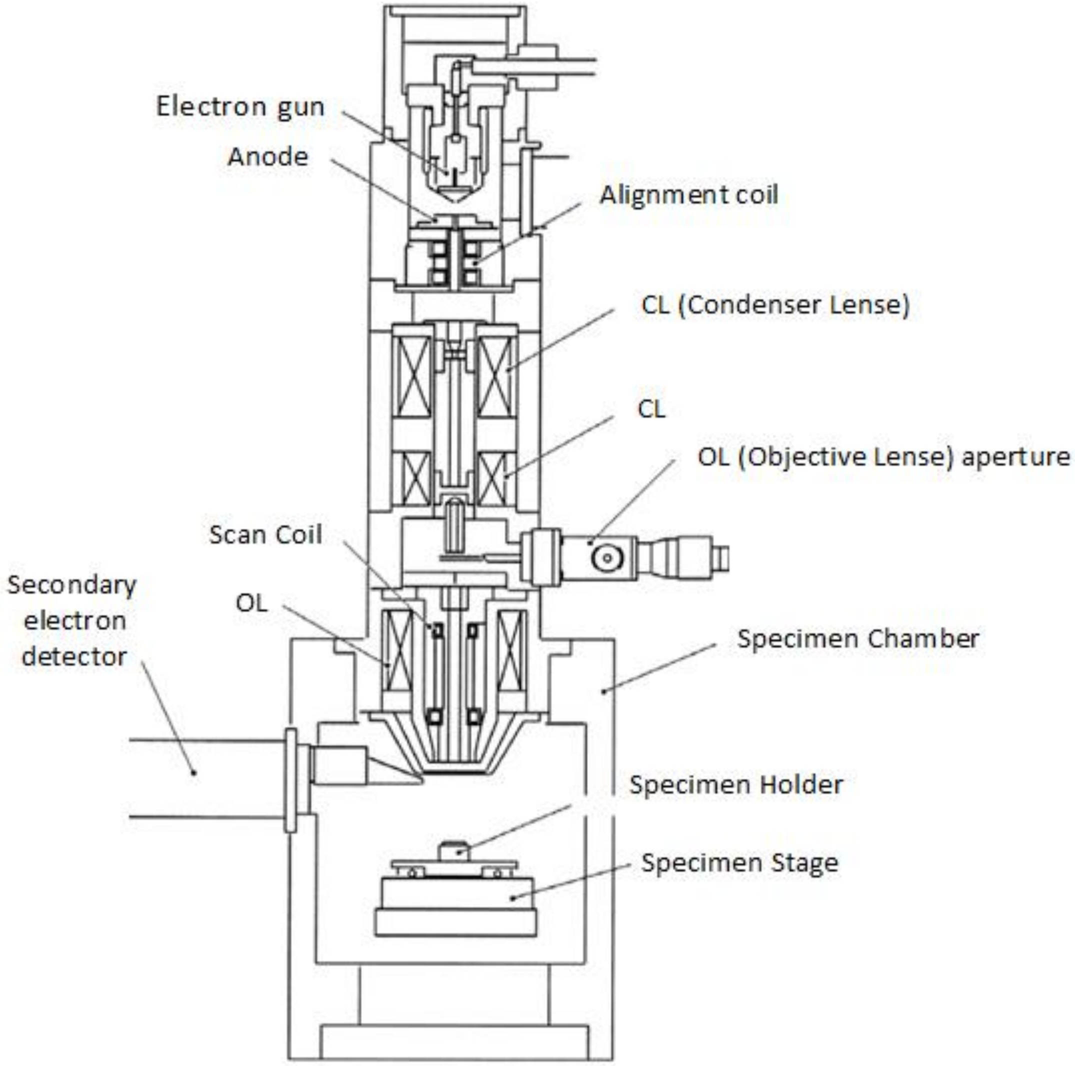

fig 3.3 Anatomy of Scanning Electron Microscope.

3.4 UV visible Spectroscopy.

UV visible spectroscopy operates in UV & visible range (200-800 nm) [19]. The parameters which are measured are absorbance in case of liquids and reflectance in case of solids. In the case of solids, this spectroscopy is referred to as diffuse reflectance spectroscopy. Bohr's model defines atoms as consisting of n number of shells (each having its specific energy) in which the electrons revolve around the nucleus, among these, there is also a state which is called as the ground state from which the electrons go to excited state upon incident radiation [20]. In the case of molecules σ, π and non-bonding electrons are present [21]. Upon incident radiation transition from filled orbital to empty orbital (usually antibonding orbital) can occur [21]. These transitions require high energy to be excited, i.e., lower wavelengths (near UV region) [21]. When light passes through a solution, its initial intensity (I_0) decreases to some final intensity (I) because of absorbance which according to Beer lambert's law is directly proportional to concentration & path length of light through solution [22].

$$A = \alpha \, l \, c$$

Where A is absorbance, l is path length of light through solution & c is the concentration of solute. Transmittance (T) is given in terms of I & I_0 as [23];

$$T = \frac{I}{I_0}$$

& related to absorbance (A) as [23];

$$A = log_{10}\left(\frac{1}{T}\right)$$

Since our samples are powder, we will be mostly concerned about reflectance. To measure reflectance, we will utilize the Diffuse reflectance UV visible spectroscopy technique. Specular Fresnel reflection is the one in which angle of incidence is the same as the angle of reflection. When light is incident on the irregular sample surface, the individual Fresnel reflections give rise to an apparent phenomenon (where the angle of reflection doesn't depend on the angle of incidence) called diffuse Fresnel reflection as shown in fig 3.4 [24-25]. The widely accepted theory explaining Diffuse reflectance spectra is Kubleka-Munk (KM) theory. A solid sample consists of many particles/grains randomly distributed when light radiation is incident on the sample apart from diffuse Fresnel reflectance it can also undergo refraction, and after refraction, it may undergo many reflections or diffractions and exit the sample surface [26]. This type of radiation is termed as Kubleka-Munk reflectance as shown in fig 3.5 [26].

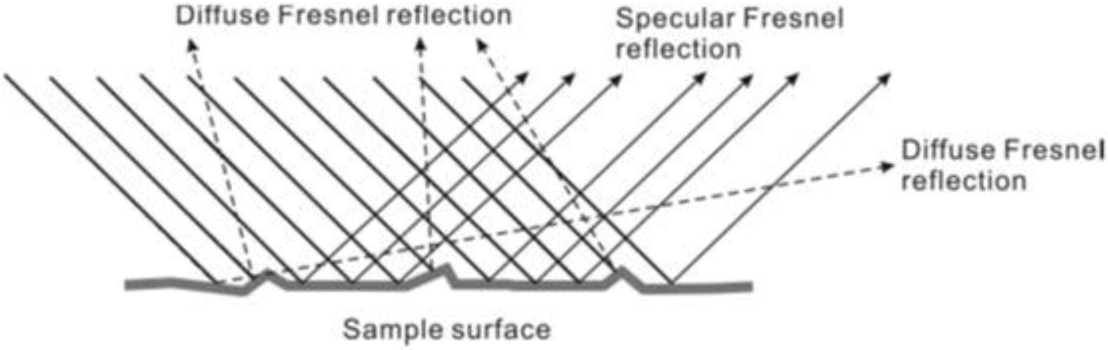

fig 3.4 Difference between Diffuse Fresnel & Specular Fresnel reflections.

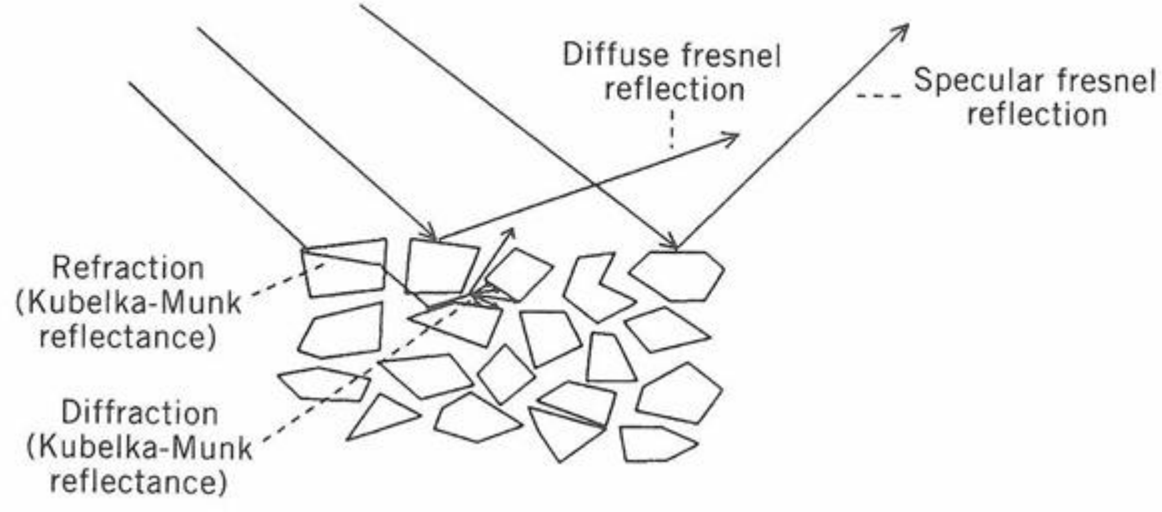

fig 3.5 KM reflectance in contrast to Specular & Diffuse Fresnel reflections.

KM theory is mainly a two flux theory, i.e., it deals with the radiation incident from two opposite directions on the layer of a material [27]. There are two components to this theory which are absorption coefficient (K) & scattering coefficient (S) as is apparent from KM function given as [28];

$$\frac{K}{S} = \frac{(1 - R_\infty)^2}{2\, R_\infty}$$

Where R_∞ is absolute remittance. The ∞ symbol denotes that the sample/material thickness should be infinite, i.e., none of the light radiation should completely penetrate the sample. The assumptions of KM theory are as follows [26,29];

1. Fresnel reflection is to be ignored.
2. The constituent grains/particles are smaller than the thickness of the sample.
3. The light radiation does not penetrate the sample.
4. The sample area should be much larger than the thickness.

Now we will discuss the instrumentation of the diffuse reflectance spectrophotometer. An integrating sphere is used for data acquisition. An integrating sphere is a hollow spherical container coated with a nearly 100% reflecting surface from inside to diffuse the input light radiation uniformly on the inside surface [30]. The reference sample (one with nearly 100% reflectance) is first situated in a holder as shown in fig 3.6 for the auto-correction then the sample of interest is placed in the holder to determine the relative reflectance [26].

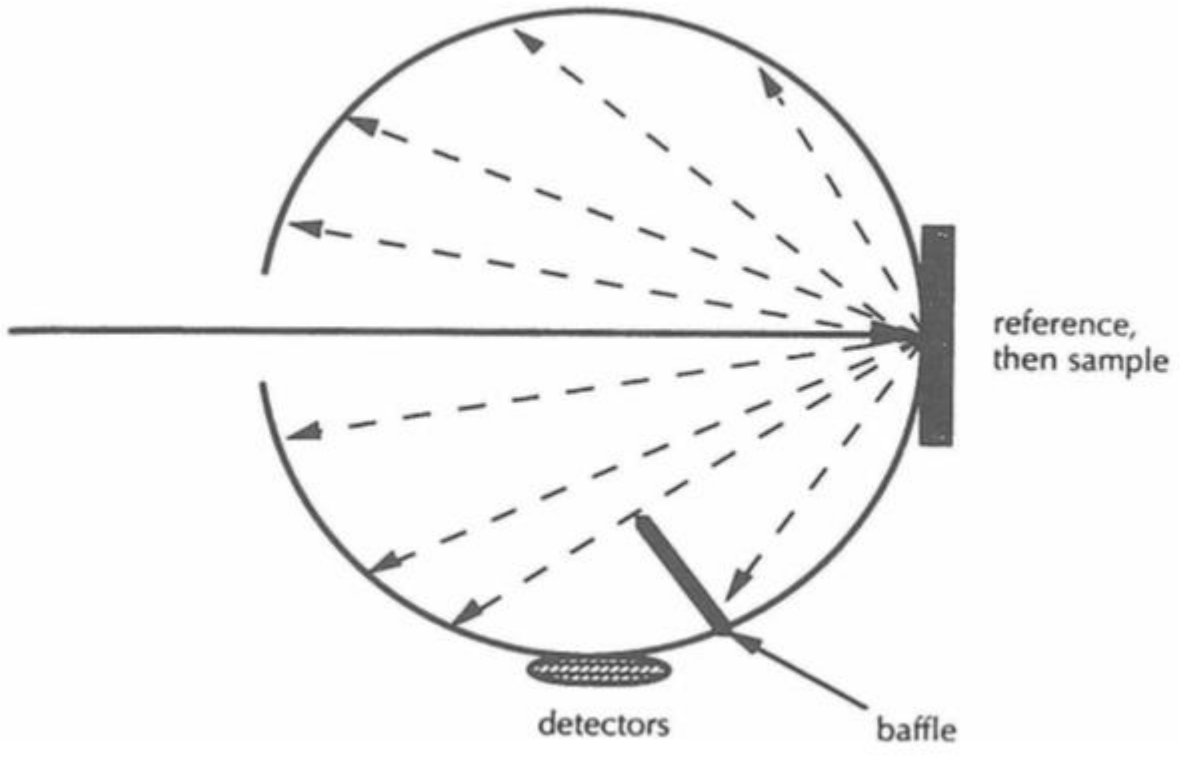

fig 3.6 Integrating sphere; an optical component to diffuse the incoming light radiation.

The detector detects the radiation intensity & we thus obtain the reflectance spectra of the sample.

3.5 Fourier Transform Infra-Red Spectroscopy.

The energy of the molecule consists of electronic, rotational, vibrational & translational energy [31]. The electronic transitions occur atUV-visible region, rotational transitions at the microwave region while the vibrational at infra-red region of the electromagnetic spectra [31]. The infra-red region occurs between 700nm – 1mm [32]. So study in this region is important to understand the types of bonds present in a given compound. The vibrational and rotational motions of the molecules are the ones responsible for the infra-red spectra [33]. In a classical mechanics' point of view, a dipole can be visualized as a simple harmonic oscillator in which the force between the two atoms follow the linear relationship with a distance (Hooke's Law) where the vibrational frequency ν is given as [34];

$$\nu = \frac{1}{2\pi c}\sqrt{\frac{k}{\mu}}$$

Where c is the speed of light, k is the force constant & μ is the reduced mass of the dipole. In quantum mechanical domain when the Schrodinger equation is solved using simple harmonic oscillator the obtained energy eigen values are quantized [35];

$$E_n = (n + \frac{1}{2})\hbar\omega$$

Where ђ is Planck's constant, ω is the frequency of oscillation and n = 0, 1, 2, 3…. Thus the energy difference between the two states is ђω as shown in fig 3.7. But in reality, the simple harmonic oscillation is just an approximation, so anharmonicity should also be considered. The solid curve shown in fig 3.8 [37] is the one which accounts for this anharmonicity (Morse curve) as opposed to the dashed curve (simple harmonic approximation). The potential is given as [36]

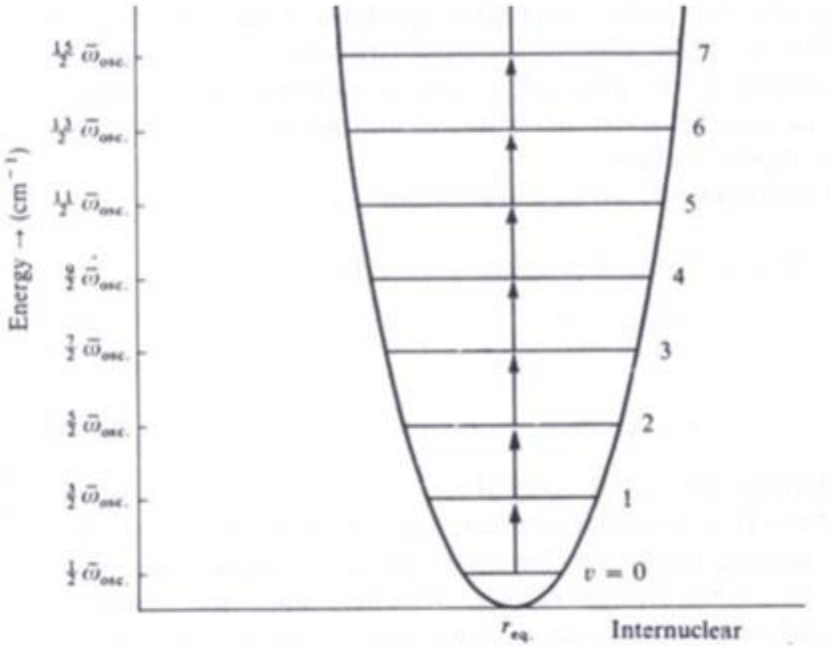

fig 3.7 The allowed vibrational transitions are shown for a diatomic molecule in simple harmonic approximation.

$$V(r) = D\,\{1 - \exp[-b(r - r_e\,)]\}^2 - D$$

Where D is the dissociation energy, b is constant, r is inter nuclear distance & r_e is the equilibrium internuclear distance [36-37]. The energy levels now are given as [37]

$$E_v = \left(n + \frac{1}{2}\right)\tilde{\omega}_e - \left(n + \frac{1}{2}\right)^2 \tilde{\omega}_e \chi_e cm^{-1}$$

The energy levels are now contained within the Morse potential where $\tilde{\omega}_e$ is oscillation frequency & χ_e is anharmonicity constant.

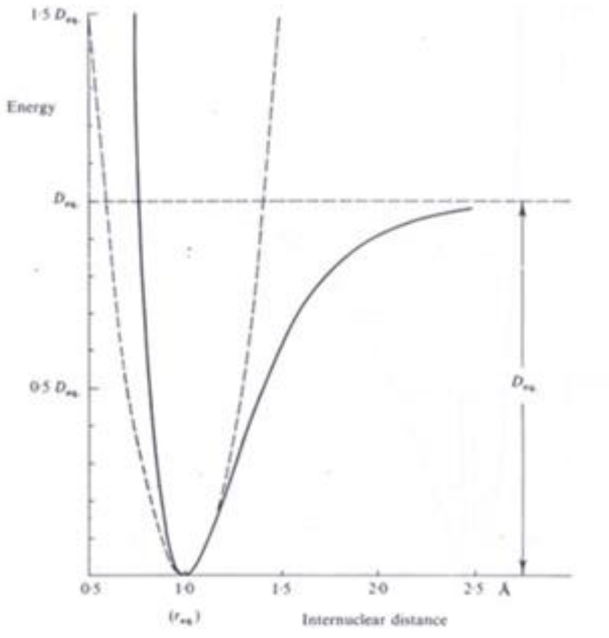

fig 3.8 The curve with dashed line is for ideal simple harmonic oscillator while the solid curve is due to Morse potential.

3.5.1 Working of FT-IR.

FT-IR is based on Michelson interferometry [38-39]. The set up consists of beam splitter, fixed & moving mirror, detector & IR source [39]. The IR source emits radiation in the direction of a beam splitter which reflects the incident beam towards fixed & moving mirrors (the splitting is 50-50%) [39]. The mirrors again reflect the radiation towards beam splitter which in turn again reflects half the beam towards detector and half towards the IR source [39]. The format in which the signal is recorded is known as interferogram which is then converted to spectrum by Fast fourier transform algorithm [39]. The stretching, bending modes are thus probed by their characteristic frequencies [40-41].

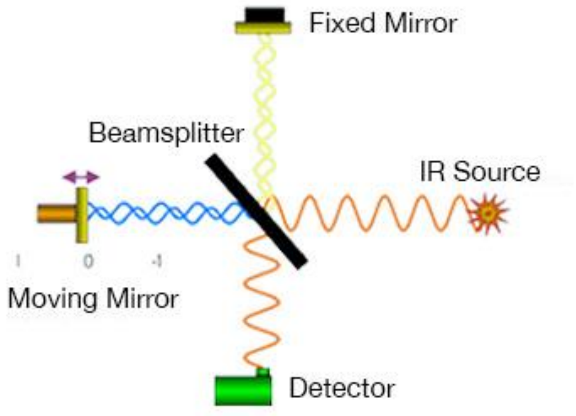

fig 3.9 Typical set up of FT-IR spectrometer [38].

3.6 Energy dispersive x-ray spectroscopy (EDS).

EDS is a technique which is used along with SEM for characterization of elements present (along with their respective proportions) in the sample [42]. There are electron distributions around the atomic nucleus which are referred to as shells, i.e., K, L, M, etc. [43]. When an electron beam is incident on a sample two types of radiations are realized: one is characteristic x-ray & other is continuum x-ray [42]. Both are the result of inelastic interactions [42]. Characteristic x rays are the ones which are emitted by atoms due to electronic transitions upon bombardment of incident electrons [44]. While the continuum x-ray/bremsstrahlung is the radiation emitted by electrons upon deceleration [45], they represent the background [42]. So characteristic x rays are the ones who give useful information about the elemental composition of the sample as can be inferred from following equation (Moseley's equation) which relates atomic number Z to frequency ν [6].

$$\sqrt{\boldsymbol{\nu}} = \boldsymbol{C}\ (\boldsymbol{Z} - \boldsymbol{\sigma})$$

Where C & σ are constants. The characteristic x rays which are emitted by the sample are taken up by the detector which converts the signal into the voltage pulse which in turn is converted in digital signal to give the spectrum [46]. The data can also be represented in an image format also known as elemental mapping.

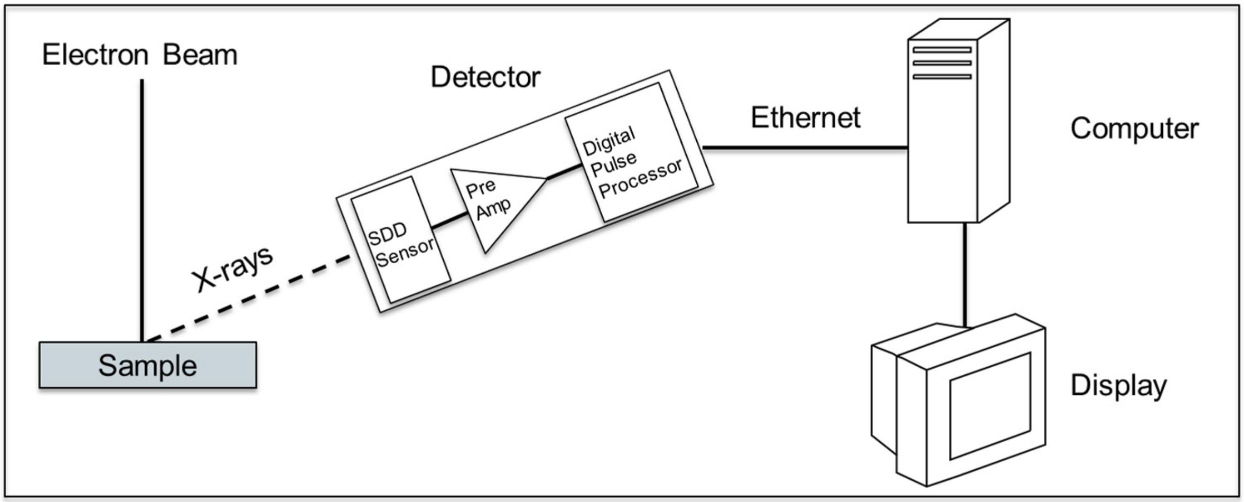

fig 3.10 Construction of EDS [46].

3.7 Small angle neutron scattering (SANS).

3.7.1 Scattering (background).

When particles are incident on some target; due to interactions with the target's potential their path is deviated. This phenomenon is known as scattering. Scattering is a useful tool in physics to probe the microscopic matter. Scattering cross section is the quantity which is determined in any scattering experiment. Scattering cross section is the number of particles scattered per unit time per unit flux of incident radiation [47]. When we are interested in detecting the number of particles in a small element of solid angle $(d\Omega)$, then this quantity is referred to as differential cross section [48]. In the case of classical Rutherford scattering the differential cross section is given by [49];

$$\frac{d\sigma}{d\Omega} = \frac{Z^2 e^4}{(4\pi\varepsilon_0)^2 m^2 {v_0}^4 sin^4(\frac{\theta}{2})}$$

Where Z is a nuclear charge of the target atoms, e is the electronic charge, ε_0 is the permittivity of free space, m is the mass of incident particles, v_0 is the velocity of incident particles & θ is the angle at which particles are deflected. Integrating the above equation will give us the idea of the total scattering cross section [49]. Quantum mechanical treatment of scattering deals with the wave functions & square of their moduli; as trajectories (as in Rutherford scattering) make no sense in quantum mechanics. The wavefunction has two parts one an incident part and other the scattered part given as [48];

$$\Psi(\vec{r}) = \Phi_{inc}(\vec{r}) + \Phi_{sc}(\vec{r}) \simeq A\left[e^{i\,\vec{k}_0.\vec{r}} + f(\theta,\phi)\frac{e^{i\,\vec{k}.\vec{r}}}{r}\right]$$

Where $\Phi_{inc}(\vec{r})$ & $\Phi_{sc}(\vec{r})$ are incident and scattered wave functions, A is normalization constant $\vec{k}_0$ & $\vec{k}$ are incident and scattered wave vectors, $f(\theta,\phi)$ is scattering amplitude. Differential scattering cross section is related to scattering amplitude as [48]

$$\frac{d\sigma}{d\Omega} = \frac{k}{k_0}|f(\theta,\phi)|^2$$

After solving the Schrödinger's equation in a potential V in center of mass frame we get [48];

$$\frac{d\sigma}{d\Omega} = \frac{\mu^2}{4\pi^2\hbar^4}|\langle\phi \mid V \mid \Psi\rangle|^2$$

The methods such as Born approximation (for weak potential) & partial wave analysis can be used for further treatment on differential cross section [50-51].

3.7.2 Neutron scattering.

Neutrons are electrically neutral spin 1/2 particles with an atomic mass of 1.00866491560, the magnetic moment of -1.91304273 nucleon magneton (μ_N) & a lifetime of 885.7 sec [52]. The scattering of neutrons can occur due to either the nucleus or the magnetic moment of the target atoms [53]. The former is referred to as nuclear scattering and the latter is referred to as magnetic scattering [53]. Because of neutron's interaction with the magnetic field, neutron scattering has been an influential tool for the understanding of magnetism [54]. There are different techniques based on neutrons which one can use such as neutron diffraction, small angle neutron scattering, inelastic neutron scattering & quasi-elastic neutron scattering [55]. Neutron diffraction is used for studying crystalline structure of matter [56], inelastic neutron scattering to study vibrational modes [57], quasi-elastic neutron scattering to study the rotational & translational motion of molecules [58-59], small angle neutron scattering (SANS) to determine sizes & morphologies of materials [60]. SANS is the technique used to characterize the $BaTiO_3$ nanoparticles (chapter 6).

The atoms can be represented as an ensemble of different scattering lengths b_i (same as scattering amplitude defined earlier) [53]. In general, for an atomic ensemble a new quantity can be defined known as scattering length density (SLD) as [53];

$$\rho = \frac{\sum_i^n b_i}{V}$$

Where V is the volume of target atoms & b_i's are the scattering lengths of individual atoms in a molecule. Macroscopic scattering cross section then is given as [53];

$$\frac{d\Sigma}{d\Omega}(q) = \frac{1}{V}\left|\int \rho(\vec{r}) e^{i\vec{q}.\vec{r}} d\vec{r}\right|^2$$

Where q is a wave vector given as $q = \frac{4\pi}{\lambda}\sin(\frac{\theta}{2})$, λ is the wavelength of incident radiation & θ is scattering angle.

In an actual experiment, the sample is not suspended in a vacuum, but it is surrounded by external media such as a solvent. So now we have to take into account the role of solvent too that's where the concept of contrast variation emerges. So the actual scattering length density can be given after removing the solvent's contribution as [61];

$$g(\vec{r}) = \rho(\vec{r}) - \rho_s$$

Where ρ_s is scattering length density of the solvent. The more the difference between SLD of particles & solvents more is the contrast, and more clearly we can determine the particle's properties [61]. There are two regimes of scattering one due to Porod & other due to Guinier. Porod's law states that at large q (i.e., larger than the inverse of scattering dimension of the particle) [53,62];

$$I(q) \alpha\, q^{-4}$$

follows. While the low q regime is dealt by Guinier's law which states [53];

$$I(q) \simeq I(0)\exp(\frac{q^2R_g^2}{3})$$

Where $I(0)$ is forward scattering intensity & R_g is radius of gyration [63].

Form factor $P(q)$ & structure factor $S(q)$ are one of the most important quantities in any scattering experiment. Former refers to scattering by different spatial regions of same particle and latter refers to scattering by different particles [53].

Every particle shape (like sphere, cylinder etc.) has its own form factor. For e.g. spherical particles are identified with form factor [64].

$$P(q) = \frac{3\sin(qr) - qr\ cos(qr)}{qr^3}$$

And when the particles are simple (i.e., no interaction between two particles) structure factor is given as [53];

$$S(q) = 1 + 4\pi N_p \int_0^\infty [g(r) - 1]\frac{\sin(qr)}{qr} r^2\,dr$$

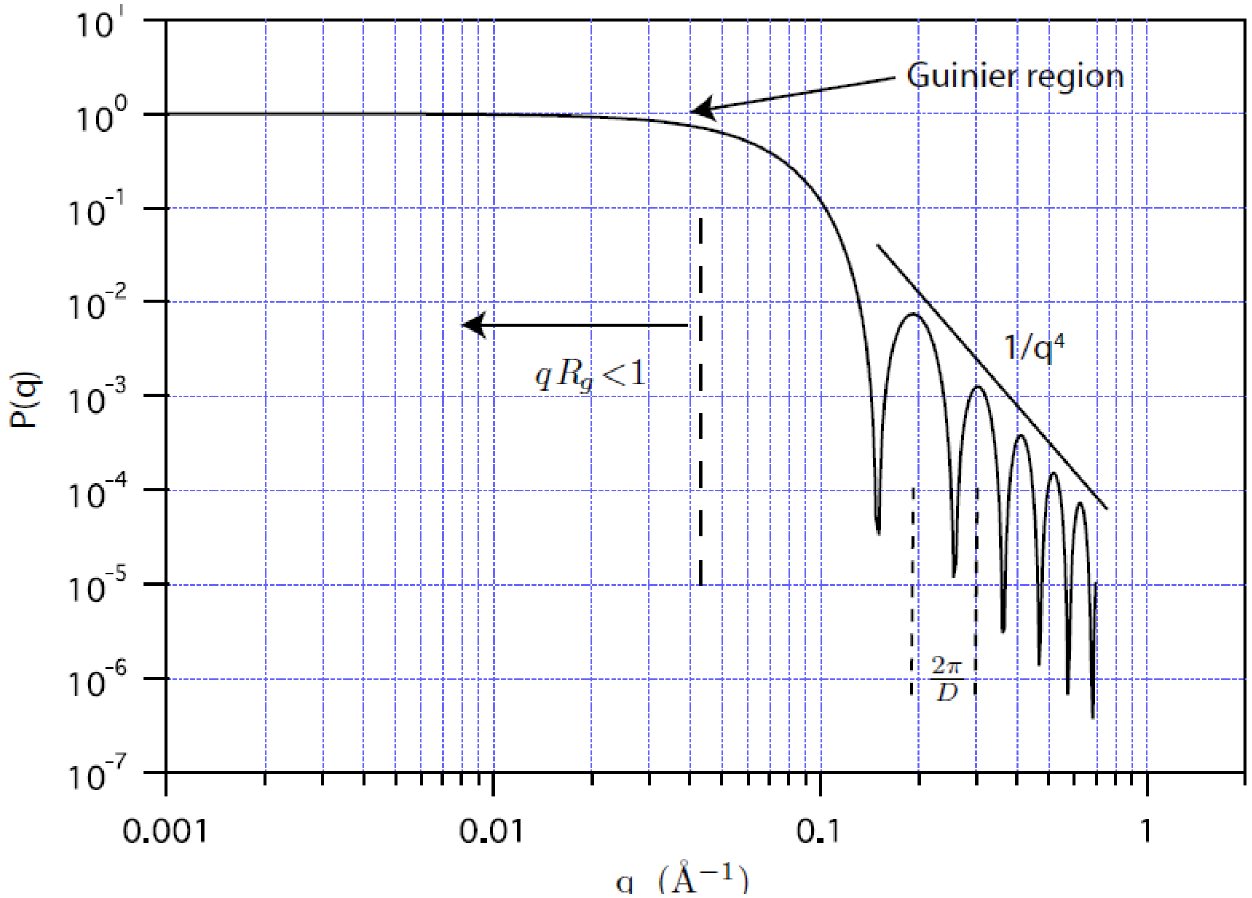

fig 3.11 Plot of P(q) vs q showing guinier & Porod regions.

So in actual analysis, appropriate form factor can be used for fitting to determine the shape of the particles since intensity is directly proportional to both $P(q)$ & $S(q)$ [53];

$$\frac{d\Sigma}{d\Omega}(q) = \frac{N}{V}(\rho - \rho_s)^2 V_p^2 P(q) S(q)$$

Where $V_p = \frac{4}{3}\pi R_g^3$. The fitting of SANS data was done with SASfit software.

3.8 Photoluminescence spectroscopy.

Photoluminescence spectroscopy is a very essential tool to characterize the defects [65]. No crystalline substance is perfect. Every crystalline structure present in nature has defects of some kind or the other that the crystal is to be imperfect is very important by a point of view of material science and engineering because of the properties they exhibit [65]. The defects have a physical explanation in the view of statistical thermodynamics that due to the increased number of microstates the entropy S is maximized and nature favors the same. The defects present in crystals are mainly of 3 types: point defects, line defects, and surface defects. We are mostly concerned about point and surface defects in this discussion. A point defect in the crystal is a defect due to missing atom from lattice site or extra atom introduced in a lattice site [66]. While the surface defects are the presence of vacancies (atoms missing from their lattice position) or interstitials (atoms acquiring extra lattice positions) on the surface among which the former trap one or more electrons leading to the formation of charged states [67], to probe these defects, the photoluminescence spectroscopy may be a valuable technique. It is a spectroscopic technique involved in the characterization of intrinsic and extrinsic properties of semiconductors and nanostructures, nondestructiveness being an advantage [68].

References

1. M. Eckert Max von Laue and the discovery of X-ray diffraction in 1912 Ann. Phys. (Berlin) 524, No. 5, A83-A85 (2012).
2. J. M. Bijvoet, W.G. Burgers, G. Hagg The History of crystal gazing, eds. 372 pp. A. oostoek's Uitgeversmaatschappij N. V., The Netherlands, 1969.
3. Medical Applications of X Rays by OTHA W. LINTON.
4. M. Deutsch,G.Holzer,J.Hartwigs,J.Wolf,M.Fritsch and E.Forster K alpha and K beta x-ray emission spectra of copper Physical Review A 51(1):283-296 · February 1995.
5. Arthur H. Compton the spectrum of scattered x-rays the physical review Second Series November 1923 Vol.22 No.5.
6. Elements of X-Ray Diffraction by B.D. Cullity.
7. Hay and Sandberg 1967; Pease 1968.
8. Principles and practice of variable pressure/environmental scanning electron microscopy (VP-ESEM) Book by Debbie Stokes.
9. P. Lenard ; Quantitatives iiber Kathodenstrahlen, Heidelberg 1918 and 1925.
10. Scanning Electron Microscopy and X-Ray Microanalysis By Joseph I. Goldstein, Dale E. Newbury, Joseph R. Michael, Nicholas W.M. Ritchie, John Henry J. Scott, David C. Joy.

11. Bernard M. Collett Scanning electron microscopy: a review and report of research in wood science Forest Products Laboratory, University of California, Richmond 94804.
12. H. Seiler Secondary electron emission in the scanning electron microscope Institut fur Physik der Universitiit Hohenheim, D-7000 Stuttgart-70, Garbenstr. 30, West Germany
13. Ludwig Reimer Imaging with Secondary and Backscattered Electrons Scanning Electron Microscopy pp 227-271.
14. T. E. Everhart and R. F. M. Thornley Wide-band detector for micro-microampere low-energy electron currents 1960 J. Sci. Instrum. 37 246.
15. Weilie Zhou, Robert P. Apkarian, Zhong Lin Wang, and David Joy Fundamentals of Scanning Electron Microscopy.
16. D. Mcmullan Scanning Electron Microscopy 1928–1965 Scanning Vol. 17, 175–185 (1995).
17. Scanning electron microscope A to Z Bsic knowledge for using SEM users manual by JEOL.
18. De Assumpção Pereira-da-Silva, M., & Ferri, F. A. (2017). Scanning Electron Microscopy. Nanocharacterization Techniques, 1–35.
19. ORGANIC CHEMISTRY Spectroscopy of Organic Compounds Prof. Subodh Kumar Dept. of Chemistry Guru Nanak Dev University.
20. Basic UV/Visible Spectrophotometry booklet by Biochrom.
21. Ch. 4 Ultraviolet/visible spectroscopy Modern Chemical Techniques by The Royal Society of Chemistry.
22. Basic UV-Vis Theory, Concepts and Applications manual by Thermospectronic.
23. Beer-Lambert Law: Measuring Percent Transmittance of Solutions at Different Concentrations (Teacher's Guide) © 2012 WARD'S Science. v.11/12.
24. F. M. Mirabella, Modern Techniques in Applied Molecular Spectroscopy, (John Wiley & Sons, 1998).
25. Hai-Bo Liu, Yunqing Chen,Glenn J. Bastiaans,X.-C. Zhang Detection and identification of explosive RDX by THz diffuse reflection spectroscopy.
26. Diffuse Reflectance Spectroscopy by J. Blitz.
27. William E. Vargas and Gunnar A. Niklasson Applicability conditions of the Kubelka–Munk theory APPLIED OPTICS y Vol. 36, No. 22 y 1 August 1997.

28. James H Nobbs Kubelka-Munk Theory and the Prediction of Reflectance Coloration Technology Volume 15, Issue 1 June 1985 Pages 66-75.
29. Li Yang and Bjorn Kruse Revised Kubelka–Munk theory. I. Theory and application Vol. 21, No. 10/October 2004/J. Opt. Soc. Am. A.
30. Integrating Sphere Design & Applications Copyright© 2007 by SphereOptics LLC.
31. Introduction to Infrared and Raman Spectroscopy By Norman Colthup.
32. Haynes, William M., ed. (2011). CRC Handbook of Chemistry and Physics (92nd ed.). CRC Press.
33. Infrared spectroscopy B Stuart - Kirk-Othmer Encyclopedia of Chemical Technology, 2005.
34. Hari Prasad Reddy Aenugu, D.Sathis Kumar,Srisudharson,N. Parthiban, Som Subhra Ghosh, David Banji Near Infra Red Spectroscopy- An Overview International Journal of ChemTech Research Vol. 3, No.2, pp 825-836, April-June 2011.
35. Introduction to Quantum Mechanics by A.C. Phillips.
36. Band, Y. B., & Avishai, Y. (2013). Angular Momentum and Spherical Symmetry. Quantum Mechanics with Applications to Nanotechnology.
37. Fundamentals of Molecular Spectroscopy by C. N. Banwell.
38. FTIR Basics manual Thermo Fisher Scientific.
39. Introduction to FTIR Spectroscopy manual by MKS.
40. Xiong et al.Photoluminescence and FTIR study of ZnO nanoparticles: the impurity and defect perspective phys. stat. sol. (c) 3, No. 10, 3577–3581 (2006).
41. Gupta et al. FTIR studies of l-I,0 and I&O decomposition on porous silicon surfaces Surface Science 245 (1991) 360-372 North-Holland.

42. Energy Dispersive Spectroscopy on the SEM:A Primer by Bob Hafner.
43. Atoms, Molecules and Photons An Introduction to Atomic-, Molecular and Quantum-Physics by Wolfgang Demtröder.
44. Introduction to Energy Dispersive X-ray Spectroscopy (EDX) of bulk specimens manual by Central facility for advanced microscopy and microanalysis University of California Riverside.

45. Chapter 19 of Handbook of Radioactivity Analysis (Third Edition) 2012, Pages 1209-1242.
46. Energy Dispersive Spectroscopy by AMETEK Materials Science Division edited by Dr Julian Heath.
47. Michael Kotlarchyk Scattering Theory Encyclopedia of Spectroscopy and Spectrometry, 1999, Pages 2074-2084.
48. Chapter 11 Quantum Mechanics Second Edition by Nouredine Zettili Jacksonville State University, Jacksonville, USA.
49. The Physics of Atoms and Quanta Introduction to Experiments and Theory by Haken & Wolf.
50. Quantum Mechanics Non-relativistic theory 2nd edition by Landau & Lifshitz.
51. Introduction to Quantum Mechanics by Griffiths,(2005) 2nd Edition; Pearson Education.
52. ABELE, H. (2008). The neutron. Its properties and basic interactions. Progress in Particle and Nuclear Physics, 60(1), 1–81.
53. Introduction to Small-Angle Neutron Scattering and Neutron Refl.
ectometry by Andrew J Jackson NIST Center for Neutron Research.
54. Neutron scattering a case study by Emma Woodfield & Institute of Physics, Institute of Physics publications 2011.
55. Jobic, H. (2000). Diffusion studies using quasi-elastic neutron scattering. Recent Advances in Gas Separation by Microporous Ceramic Membranes, 109–137.
56. A.C. Hannon Neutron Diffraction, Instrumentation Encyclopedia of Spectroscopy and Spectrometry 1999, Pages 1479-1492.
57. Clive James Chapter 4 Structural Chemistry of Glasses 2002, Pages 137-183.
58. M B´ee, Quasi-elastic neutron scattering (Adam-Hilger, Bristol, 1988).
59. W Press, Single particle rotations in molecular crystals (Springer, Berlin, 1981).
60. Hammouda et al. Small Angle Neutron Scattering at the National Institute of Standards and Technology J Res Natl Inst Stand Technol. 1993 Jan-Feb; 98(1): 31–46.
61. Structure Analysis by small-Angle X-ray and Neutron Scattering by L.A.Feigin and D.I. Svergun Institute of Crystallography Academy of Sciences of the USSR Moscow, USSR.
62. Porod G., Kolloid Zeit., 124 (1951) 83; 125 (1951) 51.

63. Guinier, A. & Fourmet, G. (1955). Small-Angle Scattering of X-rays. New York: John Wiley and Sons.
64. User guide for the SASfit software package A program for fitting elementary structural models to small angle scattering data November 15, 2018.
65. Tongay et al. Defects activated photoluminescence in two-dimensional semiconductors: interplay between bound, charged, and free excitons Scientific Reports volume 3, Article number: 2657 (2013).
66. Materials Science Ch.4 Defects in Crystals by J. W. Morris.
67. Christopher J. Bardeen The Structure and Dynamics of Molecular Excitons Annual Review of Physical Chemistry Vol. 65:127-148.
68. Eric C. Larkins, James S. HarrisJr., in Molecular Beam Epitaxy: Applications to Key Materials, 1995.

Chapter 4: Synthesis of SiO_2 nanoparticles.

4.1 Introduction.

In this chapter, we'll discuss the syntheses of different phases of SiO_2 nanoparticles. The investigation of the ferromagnetism in such nanoparticles is done with the help of SQUID magnetometer. The other characterizations such as P-XRD, photoluminescence spectroscopy, UV visible spectroscopy, fourier transform infrared spectroscopy (FT-IR) & scanning electron microscopy (SEM) are also done to study the origin of ferromagnetism in such nanoparticles.

4.2 Synthesis of SiO_2 nanoparticles of different sizes.

4.2.1 Synthesis of nanoparticles with size~440nm (SiO_2 NP 440).

SiO_2 nanoparticles were synthesized by a method described in chapter 2, i.e., Stober's hydrolysis method [1]. In a typical synthesis procedure [2] two solutions A & B were made. 18.75 ml ethanol was mixed with 1.25 mL tetraethoxysilane (TEOS) to form solution A, and to form solution B 21.5 mL ethanol was mixed with 3.5 mL aqueous ammonia (NH_4OH 25% in water) & 5mL H_2O. Then the solution A was dripped into solution B with a rate lower than 0.05 mL/s with constant stirring. The onset of turbidity was a signature of formation of SiO_2 nanoparticles. The resulting solution was aged for 48h. The solution was then taken for centrifuging and was centrifuged at 10,000 rpm for 5 minutes. The SiO_2 powder thus obtained was washed with ethanol six times and was dried at 60^0 C overnight.

4.2.2 Synthesis of nanoparticles with size~200nm (SiO_2 NP 200).

Although the SiO_2 nanoparticles obtained by the previous method showed ferromagnetic nature, the nature is very weak (as will be seen in the discussions of M vs. H data that will follow), so there is a need to synthesize even smaller particles to enhance the magnetic moment. The idea is that smaller the size of nanoparticles, larger will be the specific surface area and in turn magnetic moment [3-6]. In a typical synthesis procedure [7] 1.25 mL TEOS was added in 30mL of EtOH and stirred vigorously for 5-10 minutes then it was allowed to sonicate for 10 minutes after which 1 mL distilled water was added, and the solution was again stirred for 5-10 minutes. Then it was kept for sonication for 90 minutes, and then 2 mL of NH_4OH was added accompanied by stirring. The turbidity after 3-4 minutes was a clear indication of the formation of nanoparticles. The turbid solution thus obtained was sonicated for 3 hours and aged overnight. After aging, it was centrifuged and washed several times with ethanol and dried for 1-2 days at 60^0 C in a hot air oven.

4.2.3 Synthesis of nanoparticles of size ~ 100 nm. (SiO_2 NP 100).

To make the nanoparticles of even smaller size another protocol is used which uses sodium silicate as a precursor [8]. In these, the two batches are produced one with a lower volume of solvent let's call it batch 1 (B1), and other with a higher amount of volume let's call it batch 2 (B2). In both syntheses, the volume ratio of ammonia: ethanol was kept the same, i.e., 3:1. In case of synthesis of B1 0.5mL sodium silicate solution(SSS) was dissolved in 7mL of distilled H_2O which was added to the solution of 60 mL ammonia and 20mL ethanol. The final solution became more turbid after aging for 48 hours and then was centrifuged and washed with distilled water and dried at 60^0C. For the case of B2 same procedure was implemented except the volume taken was that of 90mL of ammonia and 30mL of ethanol. The reaction process is the same as that of the previous method except that the precursor used is different, i.e., sodium silicate instead of TEOS.

4.2.4 Synthesis of mesoporous nanoparticles (mesoporous SiO_2 NP).

Mesoporous nanoparticles are the ones which are more porous and thus have a high specific surface area (surface area per unit gram) as compared to the conventional nanoparticles (NPs) [9]. These are highly applicable in drug delivery due to the high specific surface area [10]. The aim to prepare such nanoparticles is to enhance the surface area & thus to increase the number of defects present (on the surface) which in turn will increase the magnetic moment. The mesoporous SiO_2 NPs were synthesized as in [11]. In a typical synthesis of mesoporous silica, 32mL of distilled water, 6.5g of ethanol, 5.2g of cetrimonium chloride and 0.1g of diethanolamine (DEA) were mixed and stirred in an oil bath at 60^0C for 30-35 minutes. Then 3.65mL TEOS was quickly added dropwise while stirring. The solution turned white due to the formation of amorphous silica and was kept for stirring for 2 hours. The as-prepared turbid solution was centrifuged and washed 3-4 times with distilled water after each run and dried at 60^0C in hot oven.

4.2.5 Synthesis of hollow nanoparticles (hollow SiO_2 NP).

Micelles were used as a template to synthesize hollow SiO_2 nanoparticles [12]. 0.08g of cetrimonium bromide (CTAB) was dissolved in 50 mL solution of ammonia. Ammonia: water volume ratio being 0.3. Then 0.5 mL TEOS was added followed by addition of 0.5 mL ammonia solution. The turbid solution thus obtained was stirred for additional 6 hours. After which the suspension was centrifuged and washed with water & ethanol after subsequent runs. The as-obtained powder was kept for drying at 60^0C in a hot oven.

4.3 Characterization of Nanoparticles.

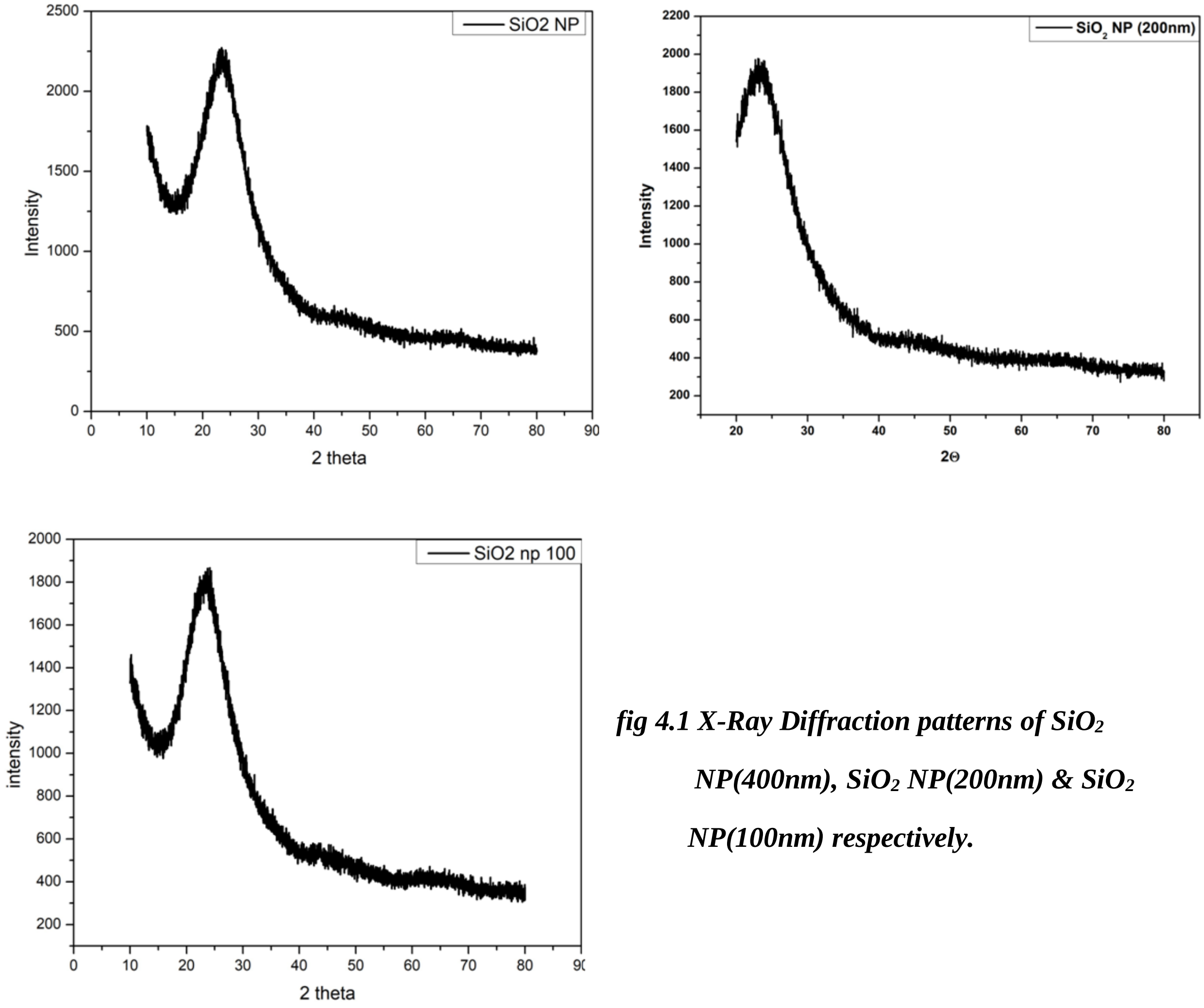

fig 4.1 X-Ray Diffraction patterns of SiO_2 NP(400nm), SiO_2 NP(200nm) & SiO_2 NP(100nm) respectively.

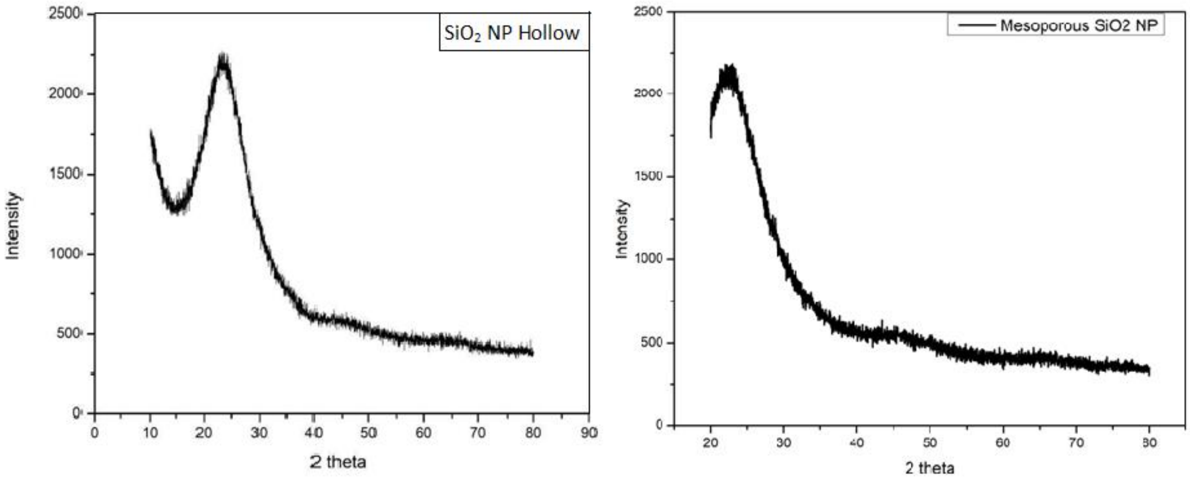

fig 4.2 XRD patterns of both Hollow &Mesoporous SiO_2 Nanoparticles.

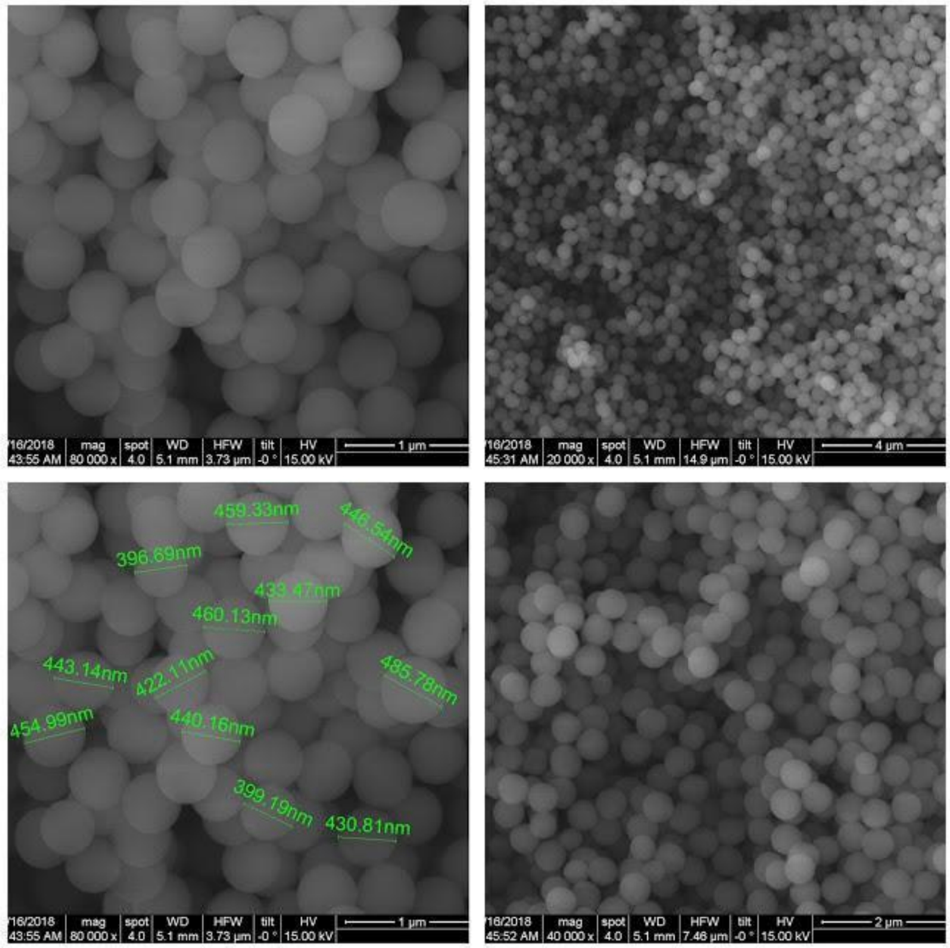

fig 4.3 SEM images of SiO_2 NP(440nm).

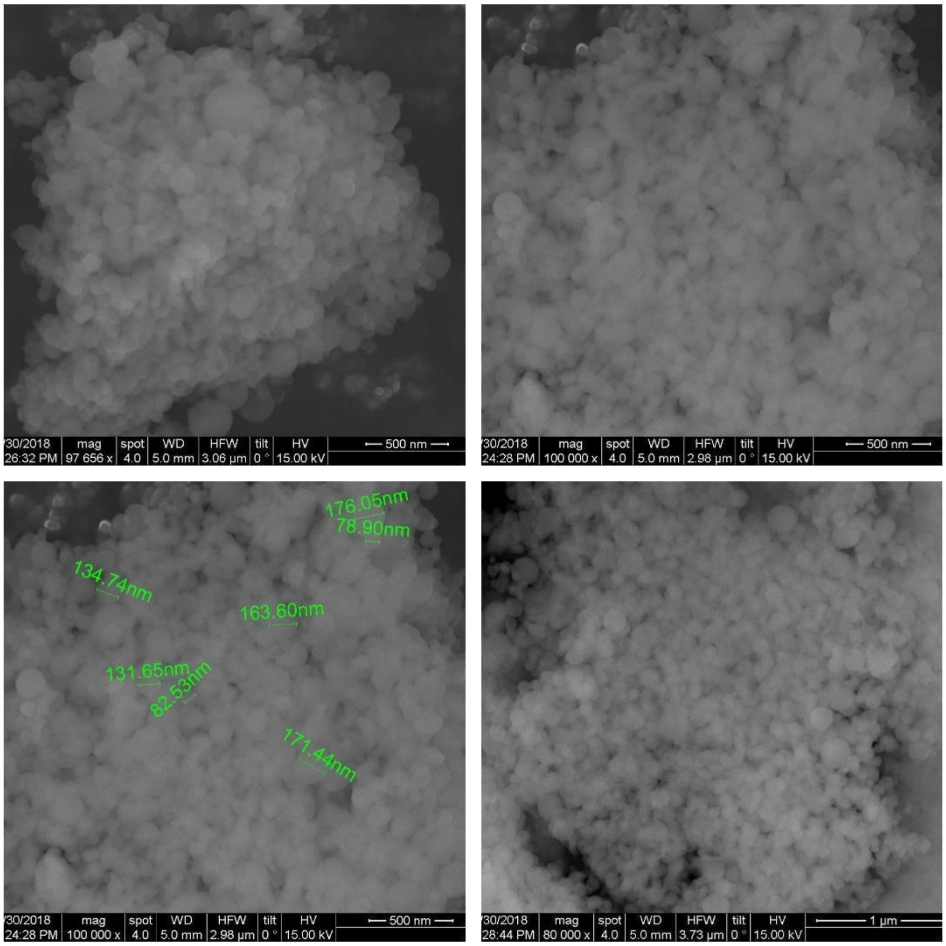

fig 4.4 SEM images of SiO_2 NP (100nm) Batch B1.

The XRD of as-prepared samples were taken with 2θ varying from 10^0 to 80^0. All the prepared nanoparticles were amorphous as evident from figs 4.1 & 4.2.

The absence of distinct sharp peaks shows the amorphous nature of the nanoparticles. For studying the morphology of as-prepared SiO_2 nanoparticles, the SEM was done. The nanoparticles formed were perfectly spherical, uniform in size and monodispersed in the case of SiO_2 NP (440nm) as is shown in fig 4.3. The SiO_2 NP(200nm) are also uniformly sized, spherical & monodispersed (fig 4.6). The batch B1 of SiO_2 NP (100nm) as shown in fig 4.4 doesn’t show uniform spherical & monodispersed nanoparticles. But batch B2 shows much-improved uniformity in size (fig 4.5).

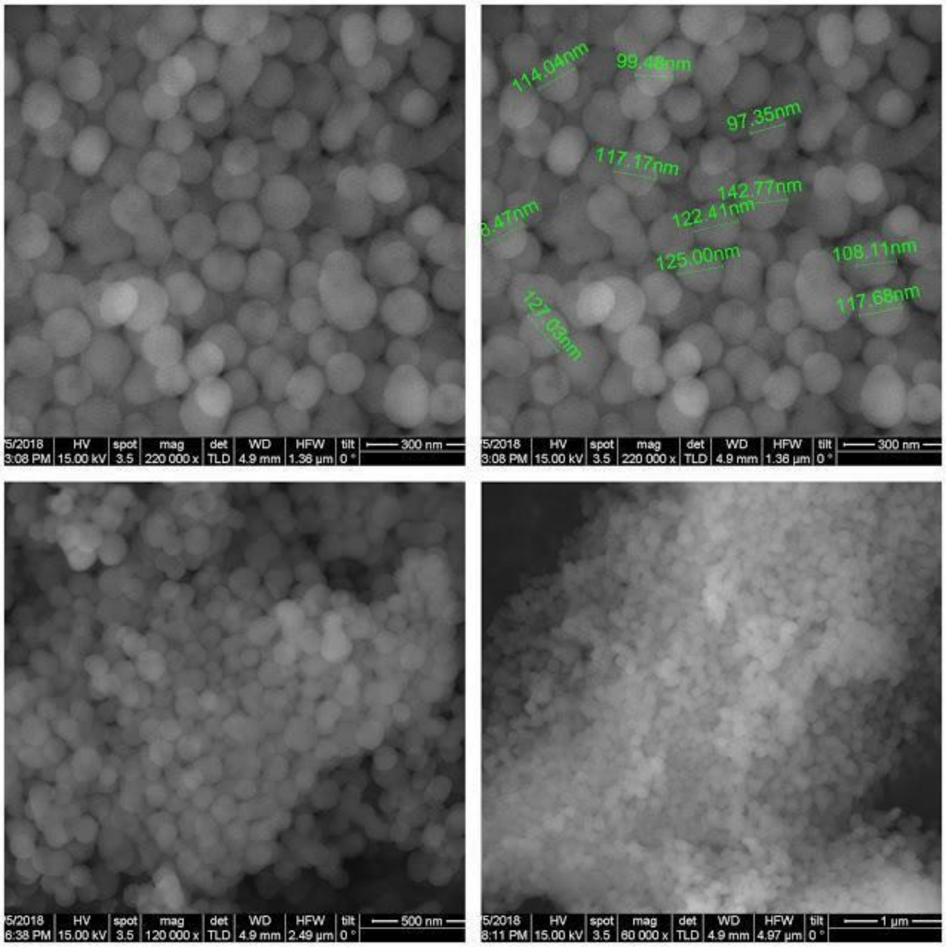

fig 4.5 SEM images of SiO_2 NP (100nm) Batch B2.

The magnetic measurements were done with SQUID magnetometer. M vs. H data was taken for the nanoparticles. The magnetic data shown in fig 4.7 was taken at 300K temperature. The data of both types of NPs clearly show the room temperature ferromagnetism. Both are soft magnetic. The SiO_2 NP (100nm) shows about three times more saturation than that of SiO_2 NP (440nm) which may be due to higher surface area; which is in agreement with previous work by Prof. Sundaresan et al. on other compounds [3-6].

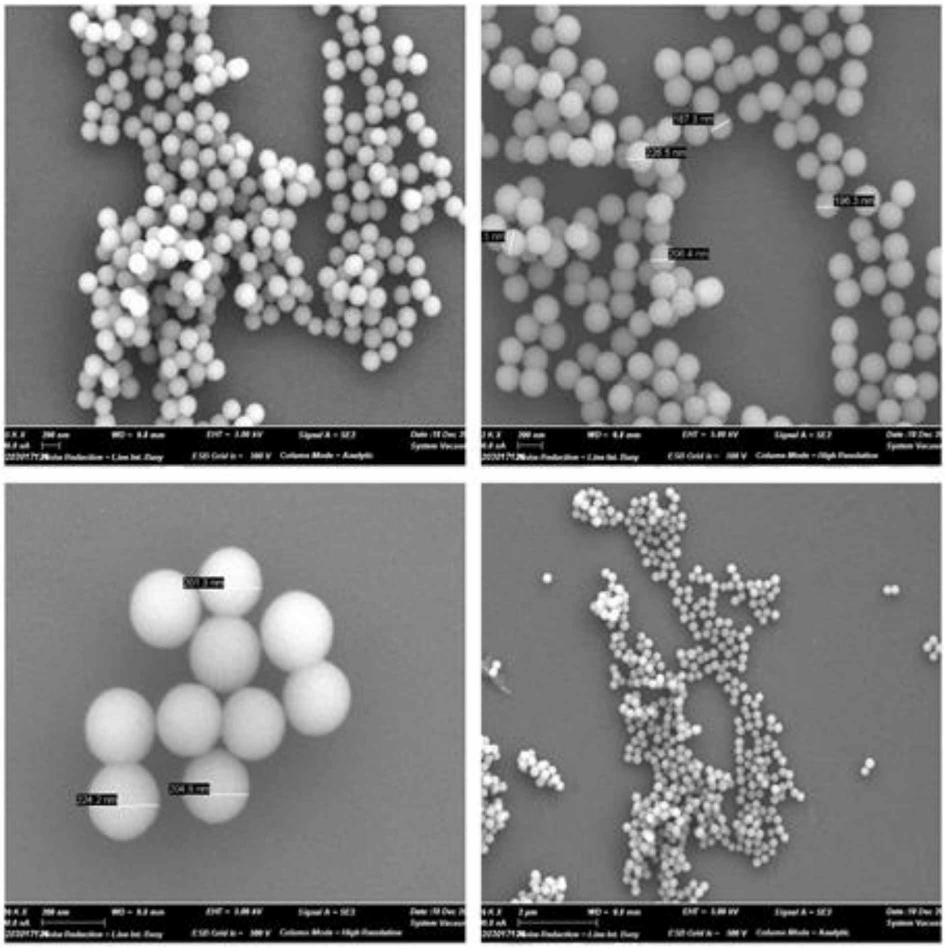

fig 4.6 SEM of SiO_2 NP (200nm).

The more saturation may be due to the higher number of concentration (per gram) of oxygen vacancies due to the higher surface area. In the case of mesoporous SiO_2 nanoparticles magnetic moment is too low as can be seen in fig 4.8. The result is rather surprising and against general expectation, because the moment anticipated was very high because of the high BET surface area of about 722 m^2/g [11]. While the hollow nano spheres show much higher moment as compared to SiO_2NP(440nm) as can be seen in fig 4.9 but yet lower than that of SiO_2 NP(100nm) still it is a relatively good result for estimated size of 250-500nm [12].

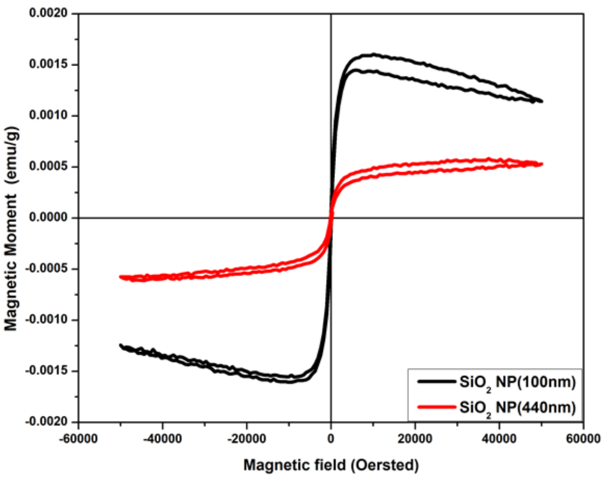

fig 4.7 M vs H data of SiO_2 NP (440nm) & SiO_2 NP (100nm).

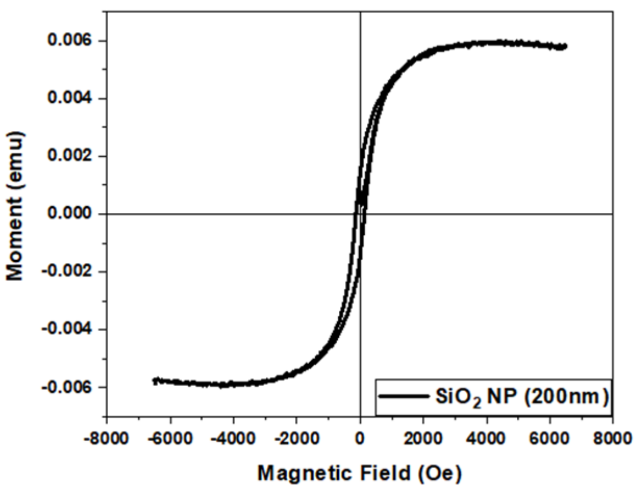

fig 4.33 M vs. H of SiO_2 NP (200nm).

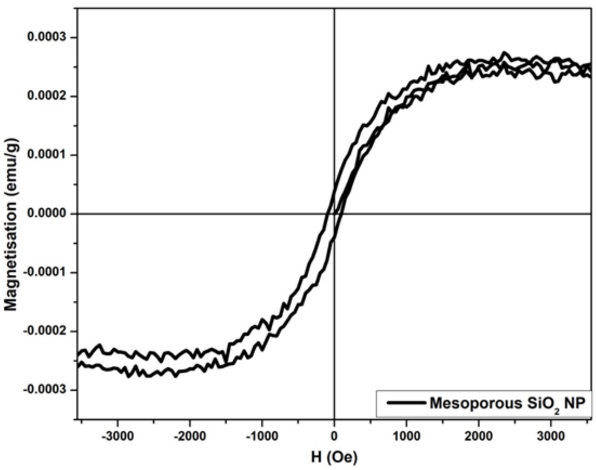

fig 4.8 M vs. H data of Mesoporous SiO_2 NP.

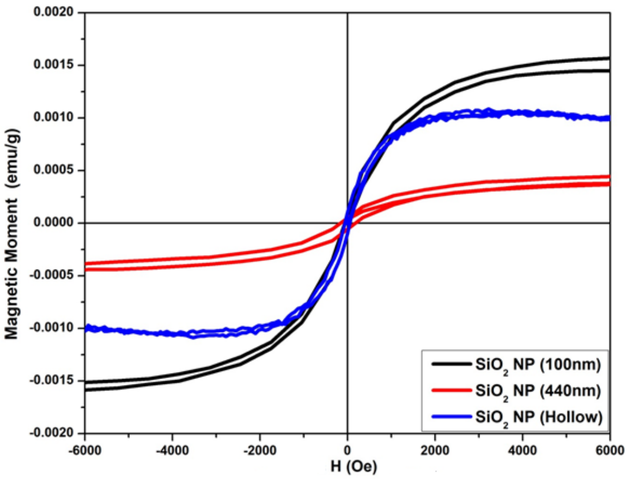

fig 4.9 M vs. H data of Hollow SiO_2 NPs compared to both 100nm & 440 nm sized nanoparticles.

SiO_2 NP (200nm) shows nearly six times higher magnetic moment than SiO_2 NP (100nm) (fig 4.33) which is surprising given its relatively bigger size. It may be due to the ultrasonication involved in its synthesis. After annealing, the magnetic moment goes down to half of its initial value.

UV visible studies were also done to find the band gap of as-prepared nanoparticles. Fig 4.10 & fig 4.11 shows the UV visible data of as prepared SiO_2 nanoparticles. The band gap was calculated by using the Tauc plot method.

4.3.1 Tauc Plots.

The valence electrons of atoms which are lower in energy are called valence band electrons, while the ones which are higher in energy and mostly responsible for conduction are conduction band electrons [14]. On the incidence of light with a particular frequency, electrons undergo a transition from valence band to conduction band [15]. The method usually used in the determination of band gap of materials from UV Visible spectra is known as Tauc plot.

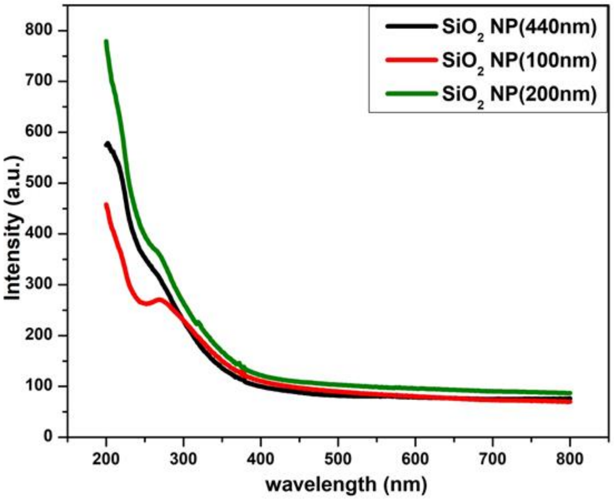

fig 4.10 Size dependence on UV visible spectra of SiO_2 Nanoparticles.

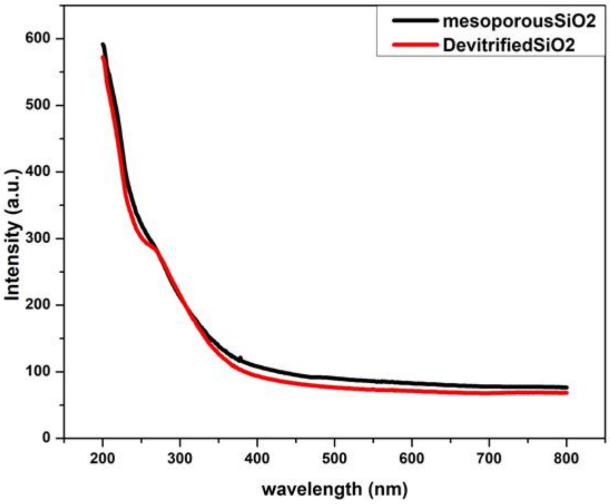

fig 4.11 UV Visible spectra of Mesoporous& Hollow SiO_2 NP.

To determine the band gap; understanding of Kubleka-Munk (KM) theory is essential. It assumes that diffuse reflection is a result of both scattering and absorption as evident from KM equation [13];

$$\mathbf{F}(\boldsymbol{R}_\infty) = \frac{(\mathbf{1} - \boldsymbol{R}_\infty)^{\mathbf{2}}}{\mathbf{2}\boldsymbol{R}_\infty} = \frac{\boldsymbol{K}}{\boldsymbol{S}}$$

Where $F(R_\infty)$ is KM function, R_∞ is absolute Remittance, K is absorption coefficient & S is the scattering coefficient. After knowing $\mathrm{F}(R_\infty)$ band gap can be determined by the equation [16],

$$(\mathrm{F}(R_\infty)hv)^2 = A^2(hv - E_g)$$

Where $\boldsymbol{hv}$ is energy, $\boldsymbol{E_g}$ is band gap.

So the first thing done was to convert 'x' axis of wavelength (nm) to energy(eV). The y-axis was changed from R to $\mathrm{F}(R_\infty)$ & the graph was plotted. Then the extrapolation was done as shown in figs 4.12,4.13 & 4.14. The intercept on the x-axis is the bandgap of the material. The results of the band gap calculations are shown in Table 4.1.

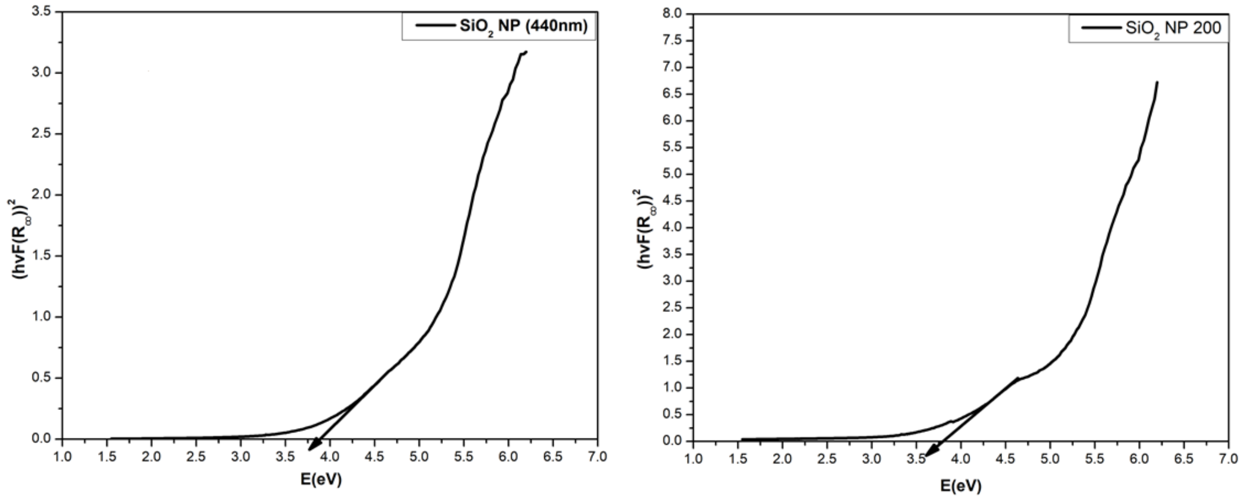

fig 4.12 Tauc plots of SiO2 NP (440nm) & SiO_2 NP (200nm).

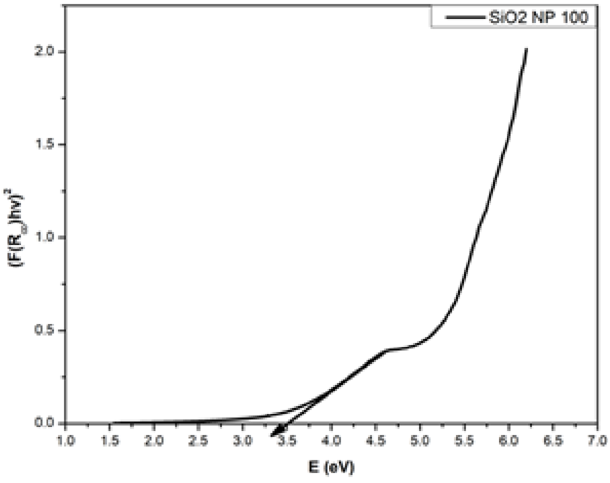

fig 4.13 Tauc plot of SiO_2 NP (100nm).

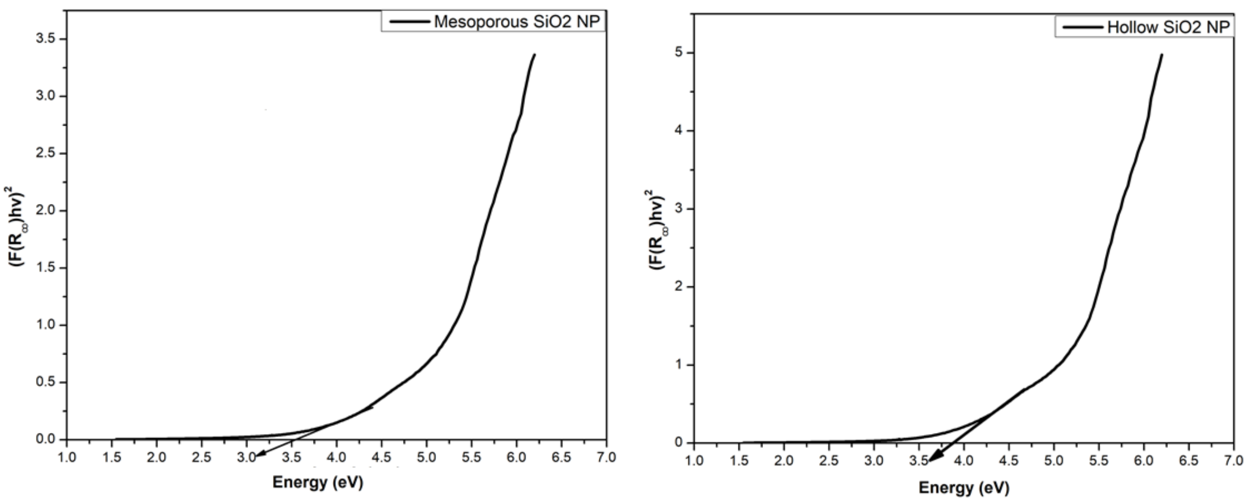

fig 4.14 Tauc Plots of Hollow & Mesoporous SiO_2 NP.

As can be seen from Table 4.1 band gap of nanoparticles decrease as the particle size decrease. The Mesoporous & Hollow nanoparticles both show a band gap of 3.56 eV & 3.88 eV respectively.

Sample Name	**Band Gap (eV)**
SiO_2 NP (440nm)	**3.88**
SiO_2 NP (200nm)	**3.79**
SiO_2 NP (100nm)	**3.54**
Mesoporous SiO_2 NP	**3.56**
Hollow SiO_2 NP	**3.88**

Table 4.1 Band gap of as prepared SiO_2 Nanoparticles.

The IR spectra of the nanoparticles were also taken to see the types of chemical bonds present in the nanoparticles. Figs 4.15 & 4.16 both show the FT-IR (Fourier transform infrared) spectra of the nanoparticles. The bond characterization is done as follows;

4.3.2 Bond Characterization.

4.3.2.1 Si-OH stretching vibrations.

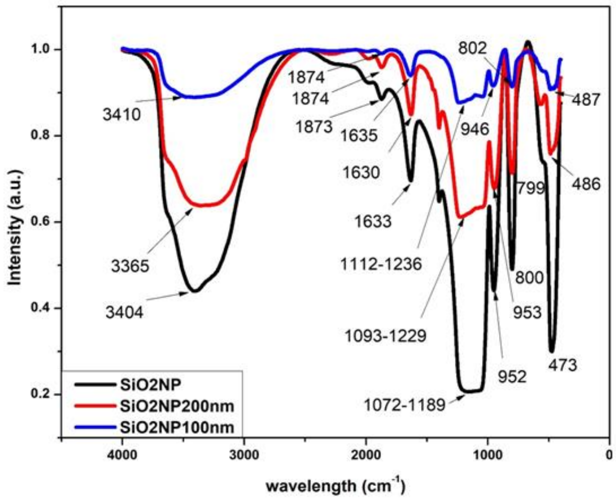

fig 4.15 Infra-red spectra of different sizes of SiO_2 Nanoparticles.

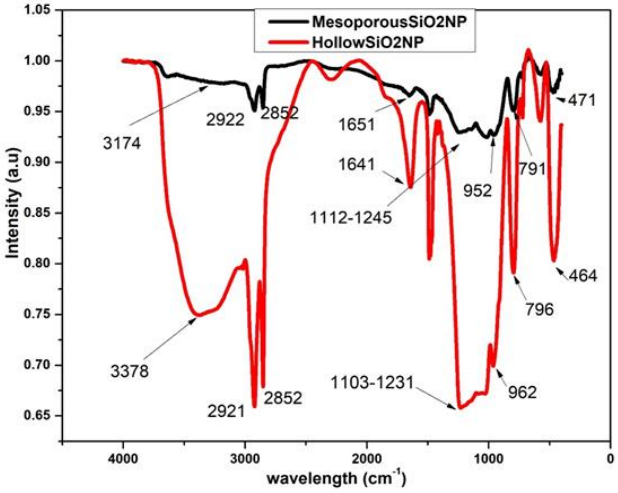

fig 4.16 Infra-red spectra of Hollow &Mesoporous SiO_2 Nanoparticles.

The characteristic band of SiO_2 NP (440nm), SiO_2 NP (200nm) & SiO_2 NP (100nm) at 3404, 3365 & 3410 cm^{-1} respectively is speculated to be from Si-OH stretching mode [17-19]. The same band occurs at 3174 & 3378 cm^{-1} for mesoporous & Hollow nanoparticles respectively.

Sample Name	**Peak Position (cm^{-1})**
SiO_2 NP (440nm)	**3404**
SiO_2 NP (200nm)	**3365**
SiO_2 NP (100nm)	**3410**
Mesoporous SiO_2 NP	**3174**

Hollow SiO_2 NP	**3378**

Table 4.2 Peak positions of Si-OH stretching.

But for mesoporous nanoparticles, it is nearly nonexistent. The band origin may be due to H_2O molecules adsorbed on nanoparticle surface [20]. But some contribution to this band can also be from bridging hydrogen between the water molecules given its broadness [21] which indicates the presence of moisture which may be absorbed by KBr while making pellets. The number of silanols per unit gram decrease as the nanoparticle size of the sample decreases. And in the case of mesoporous nanoparticles, there may be negligible numbers of silanol groups.

4.3.2.2 O-H Bending.

The existence of Si-OH stretching can be confirmed by the O-H bending bands. These bands can be located as shown in table 4.3. The band is due to water molecule [22], which confirms the existence of Si-OH on the surface.

Sample Name	**Peak Position (cm^{-1})**
SiO_2 NP (440nm)	**1633**
SiO_2 NP (200nm)	**1630**
SiO_2 NP (100nm)	**1635**
Mesoporous SiO_2 NP	**1651**
Hollow SiO_2 NP	**1641**

Table 4.3 Peak positions for OH bending.

4.3.2.3 Si-O-Si Asymmetric vibration.

The Si-O-Si Asymmetric modes are as assigned in Table 4.4 [23-25].

Sample Name	**Peak Position (cm^{-1})**
SiO_2 NP (440nm)	**1072-1189**
SiO_2 NP (200nm)	**1093-1229**
SiO_2 NP (100nm)	**1112-1236**
Mesoporous SiO_2 NP	**1112-1245**
Hollow SiO_2 NP	**1103-1231**

Table 4.4 Peak positions of Si-O-Si Asymmetric stretch.

4.3.2.4 Si–OH bending vibration.

Sample Name	**Peak Position (cm^{-1})**
SiO_2 NP (440nm)	**952**
SiO_2 NP (200nm)	**946**
SiO_2 NP (100nm)	**953**
Mesoporous SiO_2 NP	**952**
Hollow SiO_2 NP	**962**

Table 4.5 Peaks assigned for Si-OH bending vibrations.

The Si–O–H bending vibrations are assigned as can be seen in table 4.5 [26].

4.3.2.5 Si-O Bending Vibrations.

Sample Name	**Peak Position (cm^{-1})**
SiO_2 NP (440nm)	**800**
SiO_2 NP (200nm)	**799**
SiO_2 NP (100nm)	**802**
Mesoporous SiO_2 NP	**791**
Hollow SiO_2 NP	**796**

Table 4.6 Peaks assigned for Si-O bending vibrations.

The peak positions of Si-O bending vibrations are shown in Table 4.6[27-29].

4.3.2.6 Si-O Rocking Vibrations.

Sample Name	**Peak Position (cm^{-1})**
SiO_2 NP (440nm)	**473**
SiO_2 NP (200nm)	**486**
SiO_2 NP (100nm)	**487**
Mesoporous SiO_2 NP	**471**
Hollow SiO_2 NP	**464**

Table 4.7 Peaks assigned for Si-O Rocking Vibrations.

The Si-O rocking vibrations are shown in table 4.7 [30-32].

4.3.2.7 –O-CH_3 stretching Vibrations.

Sample Name	**Peak Position (cm^{-1})**
Mesoporous SiO_2 NP	**2922**
Hollow SiO_2 NP	**2921**

Table 4.8 Peaks assigned for -O-CH_3 stretching vibrations.

The -O-CH_3 stretching vibrations are shown in table 4.8 [33,34]. The –O-CH_3 bands are only observed for mesoporous & hollow SiO_2 NP. The presence of -CH_3 may be due to involvement of ethanol on the surface of nanoparticles.

4.3.2.8 Symmetric C=O stretching.

Sample Name	**Peak Position (cm^{-1})**
SiO_2 NP (440nm)	**1873**
SiO_2 NP (200nm)	**1874**
SiO_2 NP (100nm)	**1874**

Table 4.9 Peaks assigned for symmetric C=O stretching.

The symmetric C=O stretching is only observed for samples depicted in table 4.9. Their peak positions are also shown [35-37].

4.3.2.9 Symmetric CH_2 stretching.

Sample Name	**Peak Position (cm^{-1})**
Mesoporous SiO_2 NP	**2852**
Hollow SiO_2 NP	**2852**

Table 4.10 Peaks for symmetric CH_2 stretching.

Due to the presence of ethanol as solvent, there may be some aliphatic hydrocarbon moieties present which give rise to symmetric CH_2 stretching as shown in table 4.10 [38-40].

The photoluminescence (PL) spectra of as-prepared nanoparticles of sizes 440nm, 100nm, & hollow SiO_2 NP is as shown in fig 4.17. The excitation wavelength was 325 nm, and emission was observed in the range of 340nm to 575nm of wavelength. The two sharp peaks which are present in both the spectra are not to be considered because those have originated from the sample holder & are very tough to eliminate. In fig 4.18 The Photoluminescence of SiO_2 NP (200nm) is shown in the range 300-500nm, excitation wavelength being 290nm. Its PL intensity is not to be compared with other nanoparticles since it is measured from a different instrument. The mesoporous SiO_2 shows a single broad peak centered at around 388 nm which is almost three times more than SiO_2 NP (440nm), SiO_2 NP (100nm) & Hollow SiO_2 NP (fig 4.19).

In the semiconductors, the anion vacancy or the interstitial can trap electrons to give rise to what is known as excitons [41]. When the light with equal or higher energy is incident on such compounds the electrons trapped in the defects get excited, and upon relaxation they come to ground state only to radiate energy in the form of light or phonons, the former refers to the photoluminescence if the relaxation doesn’t last for more than ten seconds. Otherwise, it comes under the category of Phosphorescence. The bands observed for SiO_2 NP (440nm) & SiO_2 NP (100nm) at 431 nm translate to the energy of 2.87 eV.

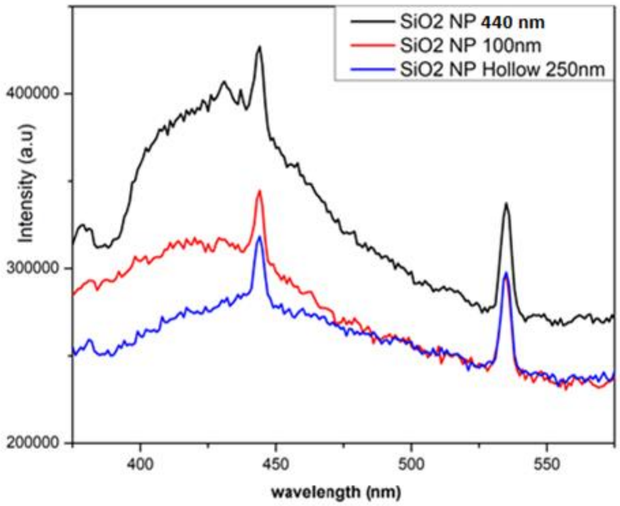

fig 4.17 Photoluminescence of SiO$_2$ NP (440nm), SiO$_2$ NP (100nm) & Hollow SiO$_2$ NP excited at 325nm wavelength.

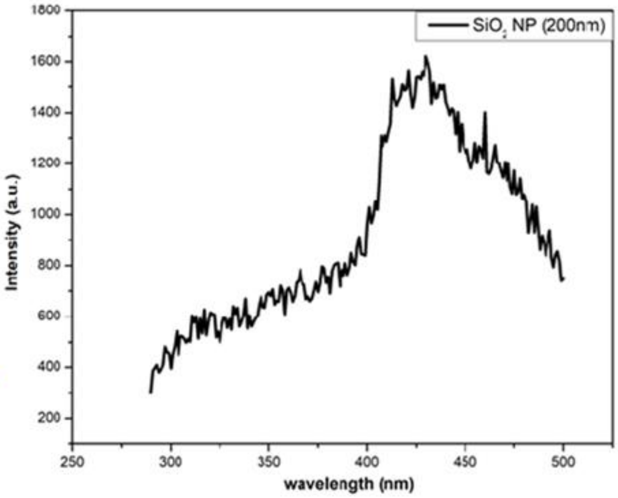

fig 4.18 Photoluminescence of SiO$_2$ NP (200nm) excited at 290nm.

In the case of SiO$_2$ NP (200nm), the band is evident at 430nm, i.e., 2.88 eV. The band observed in all cases is due to the excitons and oxygen deficiency E'γ centers [42-45]. For the mesoporous nanoparticles, the band is shifted to 3.1eV, i.e., to higher energy.

4.4 Effect of annealing.

SiO$_2$ NP (440nm), SiO$_2$ NP (100nm) & SiO$_2$ NP (200nm) were annealed at 500^0 C in hot air oven. The effect of annealing on magnetic properties was studied by SQUID, PL, UV visible spectroscopy & FT-IR.

4.5 Characterization of nanoparticles after annealing.

UV visible spectra of annealed nanoparticles were studied to investigate the effect on the bandgap. Fig 4.20 depicts the UV visible spectra of SiO$_2$ nanoparticles before and after annealing. The band gap was again calculated using the Tauc plot method.

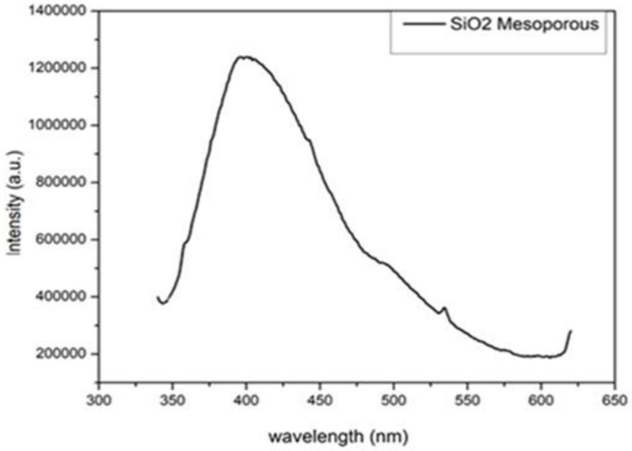

fig 4.19 PL of Mesoporous SiO_2 NP excited at 325 nm showing a broad peak around 388 nm.

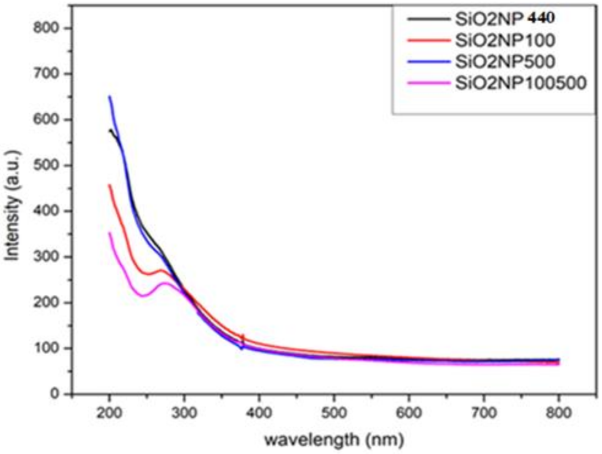

fig 4.20 UV Visible spectra of SiO_2 NPs before and after annealing.

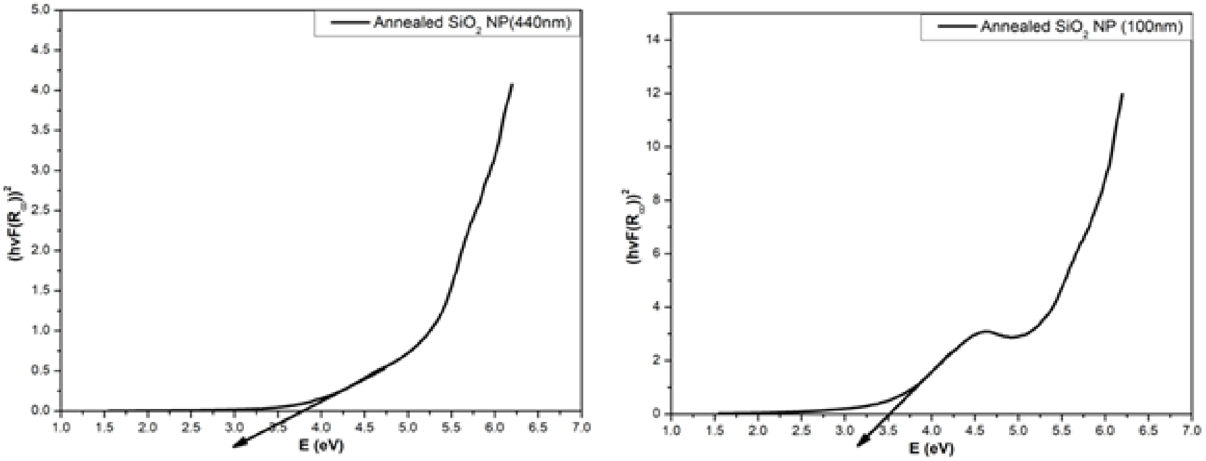

fig 4.21 Tauc plots of annealed SiO_2 NP(440nm) & SiO_2 NP (100nm).

Sample Name	**Band gap before annealing**	**Band gap after annealing**
SiO_2 NP (440nm)	**3.88**	**3.79**
SiO_2 NP (100nm)	**3.54**	**3.52**

Table 4.11 Band gaps before and after annealing.

The band gap has decreased after annealing as can be seen in Table 4.11.

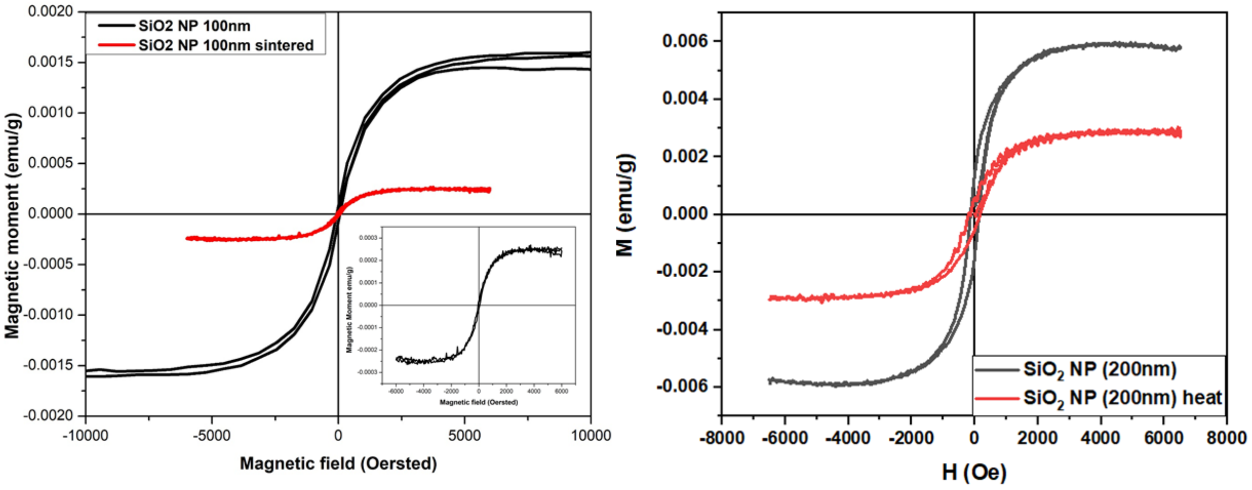

fig 4.22 M vs. H of SiO_2 NP (100nm) before and after annealing (left). The inbox shows the magnified image of M vs. H of annealed SiO_2 NP. While the right figure is that of M vs. H of SiO_2 NP (200nm) before and after annealing.

As can be seen from fig 4.22 after annealing of SiO_2 NP (100nm) the saturation magnetism went down from 0.00175 emu/g to 0.00025 emu/g i.e., the magnetism was decreased by a staggering seven times. While in the case of SiO_2 NP (200nm) the magnetic moment has nearly halved after annealing.

The FT-IR of annealed SiO_2 NP (440nm) shows the presence of only four tiny peaks as compared to the original.

SiO_2 NP (440nm)	**Peak Position (cm^{-1}) (before annealing)**	**Peak Position (cm^{-1}) (after annealing)**
Si-O-Si asymmetric vibration	**1072-1189**	**1248**
Si-OH bending vibration	**952**	**1015**
Si-O Bending	**800**	**805**
Si-O Rocking	**473**	**476**

Table 4.12 Peak positions SiO_2 NP (440nm) before and after annealing.

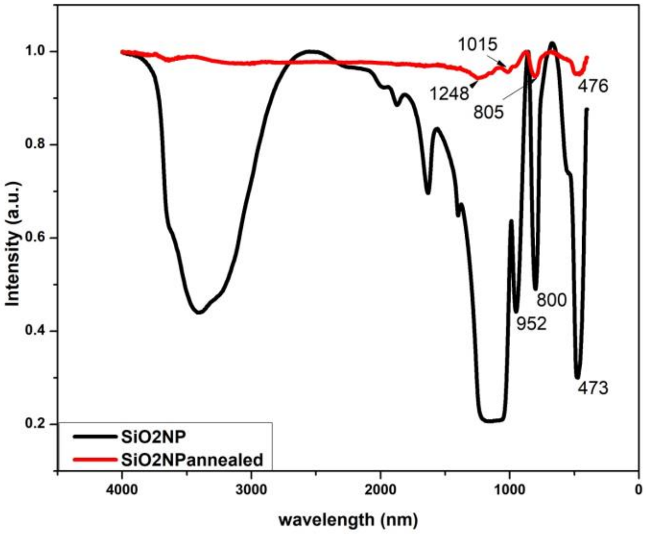

fig 4.23 FT-IR of SiO_2 NP (440nm) before and after annealing.

Only four IR peaks are detected after annealing that too with much lesser intensity as can be seen in fig 4.23. All the peaks shifted to higher energies after annealing which indicates higher energy transitions have occurred after heat treatment. There is a reduction of oxygen functionalities after annealing [46]. The Si-OH (Silanol) concentration has gone down because of the dehydroxylation process as suggested in the equation below [47].

$$\mathbf{(Si–H) + (HO–Si) \rightarrow (Si–O–Si) + H_2O}$$

So because of the higher temperature, the water in Silanols evaporates. The high energy shift of Si-O-Si asymmetric vibration shows that the oxygen vacancies are indeed filled out [48,67]. This may have little bit reflected in Si-O bending & rocking mode also.

The Photoluminescence (PL) was done by exciting at 325 nm wavelength.

As can be seen in fig 4.24 & fig 4.25 the PL of SiO_2 NP (440nm) & SiO_2 NP (100nm) after annealing shows lower intensity than the original which indicates decreased oxygen vacancies.

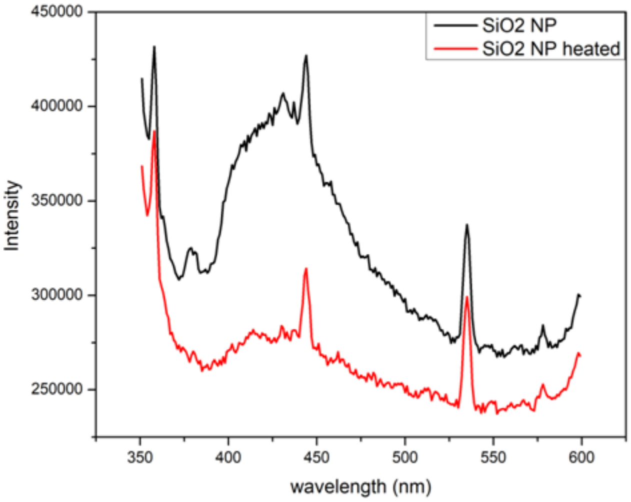

fig 4.24 PL images of SiO_2 NP (440nm) before and after annealing.

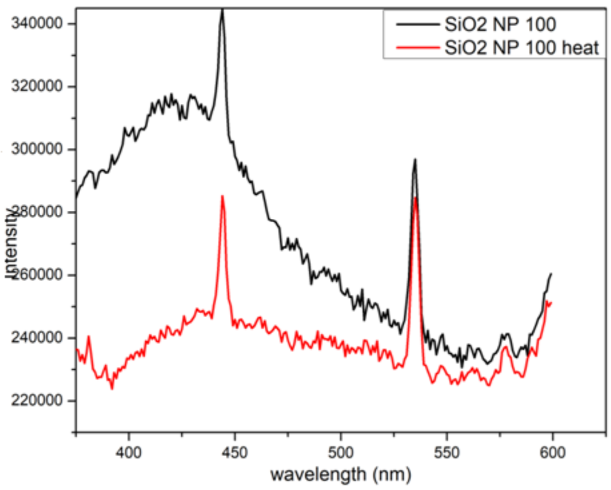

fig 4.25 PL of SiO_2 NP (100nm) before and after annealing

4.6 Results & Discussions.

We have successfully synthesized SiO_2 nanoparticles of sizes 440 nm, 200 nm & 100 nm. We also synthesized hollow & mesoporous SiO_2 nanoparticles. The idea behind synthesizing mesoporous and hollow nanoparticles was to increase the surface area and thus the magnetic moment [3-6].

We've thus investigated the dependence of the magnetism of SiO_2 nanoparticles on the size and temperature treatment. The characterizations such as XRD, SEM, photoluminescence, FT-IR, Diffuse reflectance UV was done to understand the mechanism. As the size of the nanoparticles decreased, the magnetism increased. We know that smaller nanoparticles have a bigger surface area so, in turn, more surface oxygen vacancies so we speculate that the origin of magnetism may be due to oxygen vacancies. After annealing of SiO_2 nanoparticles, the photoluminescence went down and the magnetic moment too went down in case of SiO_2 NP (100nm); so we may conclude that the oxygen vacancies is the reason for the magnetism. The much higher magnetic moment of SiO_2 NP (200nm) (i.e., six times than SiO_2 NP (100nm)) may be because of the synthesis procedure which was involved in its synthesis. About 3 hours and 90 minutes of ultrasonication during synthesis may have introduced defects and oxygen vacancies in the nanoparticles as seen in its PL spectra. The band gap has decreased with the decrease in nanoparticles size which contradicts consensus [66-67].

4.6.1 Why SiO_2 NP (200nm) has higher magnetic moment than SiO_2 NP (100nm) which has more specific surface area?

The report from Jorge Mejia et al. [68] (which is the study of effect of ultrasonication on the surface composition of nanoparticles in contrast to simple stirring) has shown that the sonication indeed creates C deficiencies on the surface of TiC nanoparticles (XPS studies). While their TEM results also showed the increase in surface roughness in both SiC & TiC nanoparticles after the sonication. Similar must have happened in the case of SiO_2 NP (200nm). The oxygen deficiencies might have been induced on the surface of the SiO_2 nanoparticles due to ultrasonication.

The number of oxygen vacancies in SiO_2 NP (200nm) are so high that they have outnumbered the oxygen vacancies present in SiO_2 NP (100nm) which has more specific surface area than SiO_2 NP (200nm).

4.7 Devitrification & fluorination.

The only ways to enhance the magnetic properties until now are to lower the size or to induce oxygen vacancies by doping (discussed in the next chapter) with other non-magnetic materials, but there can be other ways to enhance magnetism (rather than relying on oxygen vacancies) which are to utilize pairing interactions between the dopant atoms. It is already known that doping with C or N makes group II oxides which are usually nonmagnetic, ferromagnetic [49-50]. The DFT calculations demonstrate the increase in magnetism is due to pairing interactions of dopants itself [51]. We also can try to induce such pairing interactions in SiO_2 nanoparticles but the theoretical calculations done in [51] are only applicable to crystalline solids. Hence we can try to crystallize the amorphous SiO_2 nanoparticles. The process of such crystallization is called devitrification [52]. To crystallize the amorphous SiO_2, we have to break the bridging bonds so SiO_4 molecules can align in their preferred crystalline orientation. So the as-prepared mesoporous SiO_2 nanoparticles were kept in 1M $Sr(NO_3)_2$ solution for 2-3 hours and then was calcined at 750^0C only to obtain crystallized SiO_2 nanoparticles as can be seen in fig 4.27 [53].

As already stated in chapter 1; studies by Gregory Kopnov et al. have shown that the etching of the silicon wafers by HF and KOH have shown relatively large magnetic moment. Their studies suggest that the magnetism is co-related to surface roughness [54]. But the hole-bridge structures which were obtained by etching the already sintered Nano spherical array with HF show weak ferromagnetism [2]. It is speculated that HF-etching may have contributed to weak ferromagnetism in these Nano spherical arrays [2]. But instead of HF, we have used NH_4F. 0.0067 g of NH_4F was dissolved in H_2O, and 0.03 g of mesoporous SiO_2 sample was added to it. We know on an average 4.9 OH groups per nm^2 exist on the surface of SiO_2 nanoparticles [55]. We also know that BET surface area of as-prepared mesoporous SiO_2 nanoparticles is 722 m^2/g. So from this information, we have calculated how much OH groups per gram are present on nanoparticle surface and in turn how much moles NH_4F is required to fluorinate the surface.

4.7.1 Characterization of devitrified and fluorinated SiO_2 nanoparticles.

The X-ray diffraction pattern after devitrification shows the onset of crystallinity as can be seen in fig 4.27. While fluorinated SiO_2 nanoparticles show crystalline nature (fig 4.26). The peaks are of $(NH_4)_2SiF_6$. UV visible spectra are shown in fig 4.28. The band gap of mesoporous SiO_2 nanoparticles increased from 3.56 eV to 3.78 eV & 3.89 eV for devitrified & fluorinated nanoparticles respectively.

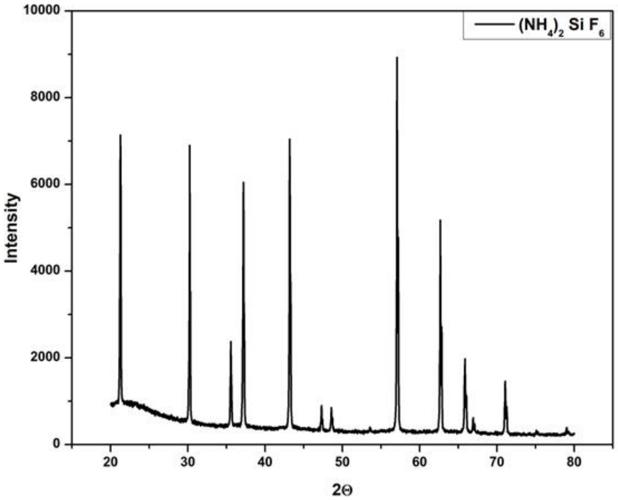

fig 4.26 XRD after fluorination. $(NH_4)_2SiF_6$ has formed.

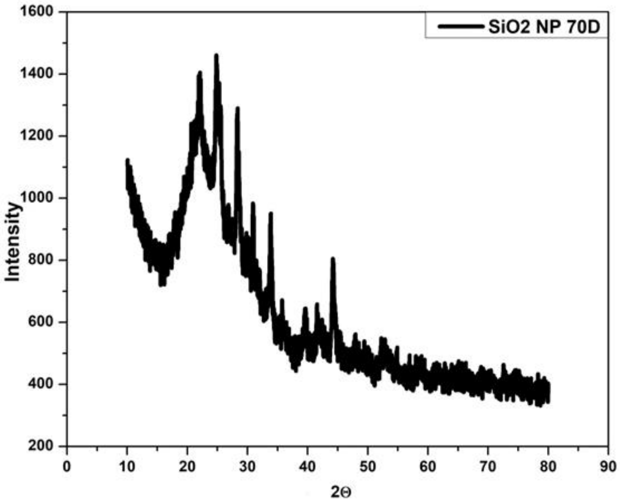

fig 4.27 XRD pattern shows onset of crystallinity although amorphous phase is still present.

The FT-IR spectra of both the devitrified and fluorinated SiO_2 nanoparticles as compared to mesoporous nanoparticles are shown in fig 4.30 & fig 4.31. The peaks are characterized in table 4.13 & table 4.14 [56-65].

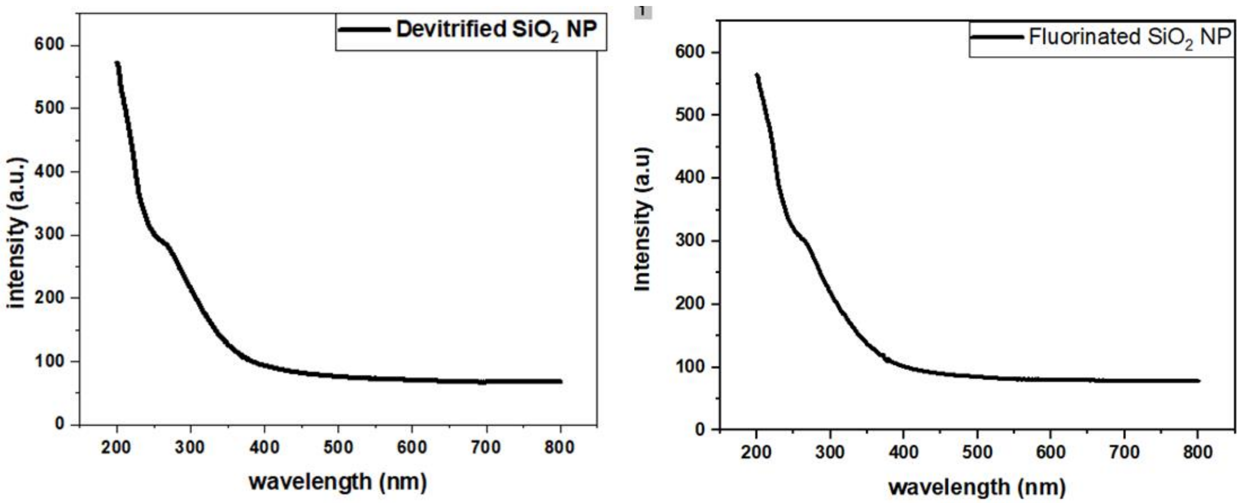

fig 4.28 UV Visible spectra of Devitrified & Fluorinated SiO_2 NPs.

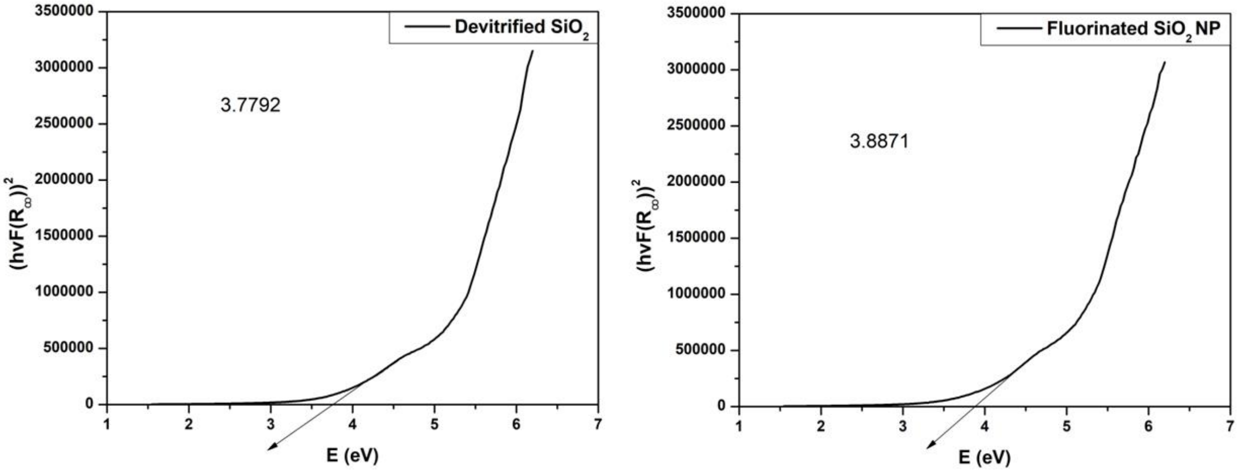

fig 4.29 Tauc plots of Devitrified & fluorinated nanoparticles respectively.

In the case of devitrified SiO_2 nanoparticles, the peaks of Si-O rocking vibrations, Si-O bending vibrations, Si-OH bending vibrations shifted to higher energies which may be because of heat treatment. The absence of 952 cm^{-1} peak shows that Si-OH indeed has been vanished after devitrification due to dehydroxylation [47]. Also, the absence of free water peak (3414 cm^{-1}) shows that water has been vaporized due to high-temperature treatment. There is also the absence of C-H bonds.

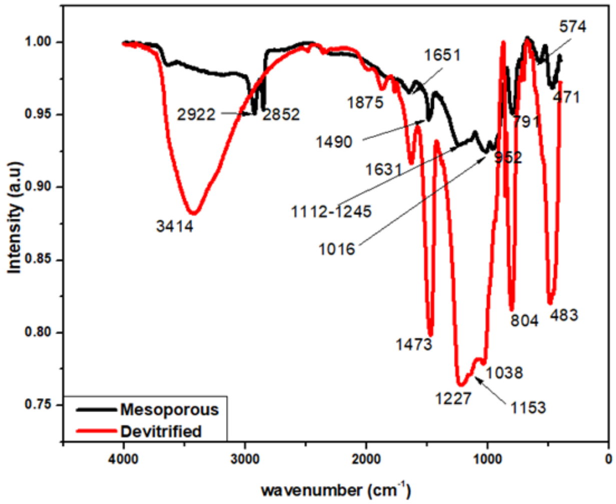

fig 4.30 FT-IR of Devitrified SiO_2 NP as compared to Mesoporous SiO_2 NP.

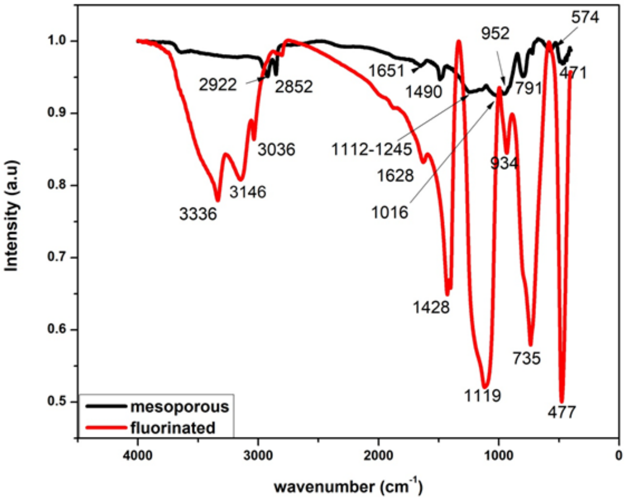

fig 4.31 FT-IR of Fluorinated SiO_2 NP as compared to original mesoporous one.

In the newly formed $(NH_4)_2SiF_6$ the new peaks have been originated shown in table 4.14 along with their positions.

M vs. H data as seen in fig 4.32 doesn't show any significant change. Now the devitrified sample can be doped with the anion to induce magnetism via pairing effect as stated earlier.

Bond nature	**Peak position before devitrification (cm^{-1})**	**Peak position after devitrification (cm^{-1})**
Si-O Rocking Vibrations	**471**	**483**
	574	
Si-O Bending Vibrations	**791**	**804**
Si-OH Bending Vibrations	**952**	
	1016	**1038**

Si-O-Si Asymmetric Vibrations	**1112-1245**	**1227**
	1490	**1473**
OH Bending	**1651**	**1631**
		1875
CH_2 Symmetric Stretch [63-65]	**2852**	
$-O-CH_3$Stretching Vibrations	**2922**	
Free water peak	**3414**	

Table 4.13 IR peak positions before and after Devitrification.

Bond Nature	**Peak position before Fluorination (cm^{-1})**	**Peak position after Fluorination (cm^{-1})**
Free water Peak	**3414**	
Si-F stretching [56-57]		**934**
NH Stretching[58-60]		**3336**
Ammonia ions [61]		**3146**
Ammonium ions [61]		**3036**
NH_4^+Bending mode [62]		**1428**

Table 4.14 Peak positions before and after fluorination.

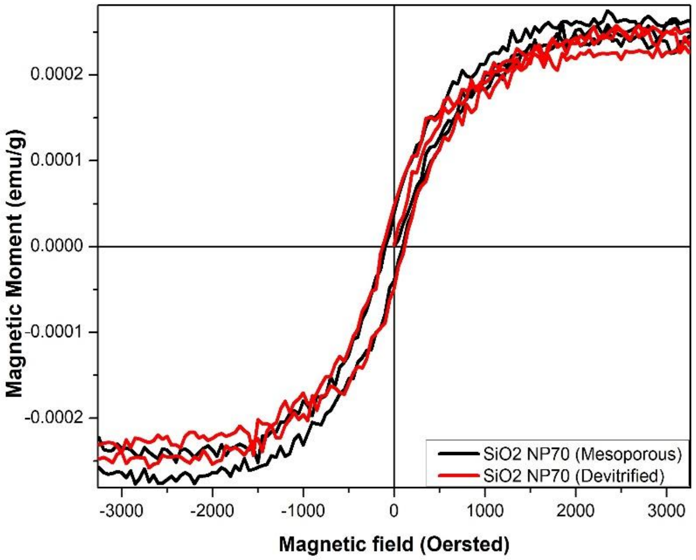

fig 4.32 M vs. H data of Mesoporous and Devitrified SiO_2 NPs.

4.10 Results & Discussions.

The devitrification hasn't affected the magnetic moment. But the future direction will be to dope with C or N or both to induce pairing effect between dopants and in turn to maximize the magnetic moment. The attempt of fluorination has failed because of the formation of ammonium fluorosilicate ($(NH_4)_2 Si F_6$).

References

1. W. Stober, A. Fink, and E. Bohn, J. Coll. Interf. Sci. 26 (1968) 62.
2. Xing Wang, Cong Mian Zhen, Xiao Wei Liu, Xiu Min Liu Li Ma, Cheng Fu Pan, Deng Lu Hou A new hole-bridge structure based on a SiO2 nanoarray and its ferromagnetism Colloids and Surfaces A: Physicochemical and Engineering Aspects Volume 446, 5 April 2014, Pages 151-155.
3. A. Sundaresan, R. Bhargavi, N. Rangarajan, U. Siddesh, and C. N. R. Rao Ferromagnetism as a universal feature of nanoparticles of the otherwise nonmagnetic oxides PHYSICAL REVIEW B 74, 161306 (R) (2006).
4. A. Sundaresan, C.N.R. Rao Ferromagnetism as a universal feature of inorganic nanoparticles Nano Today (2009) 4, 96—106.

5. Nitesh Kumar a, D. Sanyal b, A. Sundaresan Defect induced ferromagnetism in MgO nanoparticles studied by optical and positron annihilation spectroscopy Chemical Physics Letters 477 (2009) 360–364.
6. R V K Mangalam, Mahuya Chakrabrati, D Sanyal2,A Chakrabati and A Sundaresan Identifying defects in multiferroic nanocrystalline BaTiO3 by positron annihilation techniques J. Phys.: Condens. Matter 21 (2009) 445902 (5pp).
7. Synthesis of Ultrafine SiO2 NanoparticlesThrough Ultrasonication-Assisted Sol–Gel Technique Journal of Advanced Physics Vol. 3, pp. 1–4, 2014.
8. Zulfiqar, U., Subhani, T., & Wilayat Husain, S. (2016). Synthesis of silica nanoparticles from sodium silicate under alkaline conditions. Journal of Sol-Gel Science and Technology, 77(3), 753–758.
9. Mesoporous Silica Nanoparticles: A Review Mehmood et al., J Develop Drugs 2017, 6:2
10. Mesoporous Silica Nanoparticles as Drug Delivery Vehicles in Cancer Nanomaterials (Basel). 2017 Jul: 7(7):189.
11. Synthesis and Physicochemical Characterization of Mesoporous SiO2 Nanoparticles Journal of Nanomaterials Volume 2014, Article ID 176015, 12 pages.
12. Micelle-template synthesis of hollow silica spheres for improving water vapor permeability of waterborne polyurethane membrane Scientific Reports 7, Article number: 46638 (2017).
13. Haixin Bai, Xiaohua Liu Low temperature solvothermal synthesis, optical and electric properties of tetragonal phase BaTiO3 nanocrystals using BaCO3 powder Materials Letters 100 (2013) 1–3.
14. Energy bands in solids by Milman Halkias.
15. Fundamentals of electronic materials and devices, lecture notes by Prof. Parasuraman Swaminathan.
16. R.Bhatt, I.Bhaumik, S.Ganesamoorthy, A.K.Karnal, M.K.Swami, H.S.Patel, P.K.Gupta, Physics Status Solidi A, 209, 1, 176-180, 2012.
17. Dusica B.Stojanovic et al. PMMA/silica nanocomposites containing silica nanoparticles coating under supercritical conditions April 2013 Progress in Organic Coatings 76(4):626–631.

18. R.Sumathi, R.Thenmozhi. “Synthesis and characterization of spherical silica nanoparticles by Sol-Gel method.” International Conference on Systems, Science, Control,Communication, Engineering and Technology (2015): 204-208. Print.
19. Aldona Beganskiene FTIR, TEM and NMR Iinvestigations of Stöber Silica Nanoparticles ISSN 1392–1320 materials science (medžiagotyra). Vol. 10, No. 4. 2004.
20. Pedro Hoffmann novel aspects of mid and far ir fourier spectroscopy applied to surface and adsorption studies on sio2 Surface Science 188 (1987) 181-198 North-Holland, Amsterdam.
21. Barbara L Mojet et al. ChemInform Abstract: Light at the Interface: The Potential of Attenuated Total Reflection Infrared Spectroscopy for Understanding Heterogeneous Catalysis in Water December 2010Chemical Society Reviews 39(12):4643-55.
22. © 2019 Database of ATR-FT-IR spectra of various materials Institute of Chemistry University of Tartu, Estonia.
23. Sven C Feifel and Fred Lisdat Silica nanoparticles for the layer-by-layer assemblyof fully electro-active cytochrome c multilayers December 2011 Journal of Nanobiotechnology 9(1):59.
24. Jean-Denis Brassard et al. Fluorine Based Superhydrophobic Coatings December 2012Applied Sciences 2(4).
25. Li W et al. Silica nanoparticles functionalized via click chemistry and ATRP for enrichment of Pb(II) ion Nanoscale Res Lett (2012).
26. H. Banu Yener, Sßerife Sß. Helvaci Effect of synthesis temperature on the structural properties and photocatalytic activity of TiO2/SiO2 composites synthesized using rice husk ash as a SiO2 source Separation and Purification Technology 140:84-93 · January 2015.
27. Feng Gao One-Step Synthesis and Characterization of Silica Nano-/Submicron Spheres by Catalyst-Assisted Pyrolysis of a Preceramic Polymer Journal of Nanomaterials 2013(3) · July 2013.
28. E. San Andre´s et al. Rapid thermal annealing effects on the structural properties and density of defects in SiO2and SiNx:H ?lms deposited by electron cyclotron resonance JOURNAL OF APPLIED PHYSICS VOLUME 87, NUMBER 3 1 FEBRUARY 2000.

29. Sabari Saka et al. Nonlinear optical properties of Ag@SiO 2 core-shell nanoparticles investigated by continuous wave He-Ne laser Materials Chemistry and Physics 212 · March 2018.
30. F. Ay, A. Aydinli Comparative investigation of hydrogen bonding in silicon based PECVD grown dielectrics for optical waveguides Optical Materials 26 (2004) 33–46.
31. Emerson Carlos Mansaneira Sugar cane bagasse ash as a pozzolanic material Dyna rev.fac.nac.minas vol.84 no.201 Medellín Apr./June 2017.
32. J. Schäfer et al.Tetrakis(trimethylsilyloxy)silane for nanostructured SiO2-like lmsdeposited by PECVD at atmospheric pressure Surface & Coatings Technology 295 (2016) 112–118.
33. Bohdan Schneider Stretching and deformation vibrations of CH2, C(CH3) and O(CH3) groups of poly(methyl methacrylate) Schneider, B., Štokr, J., Schmidt, P., Mihailov, M., Dirlikov, S., & Peeva, N. (1979). Stretching and deformation vibrations of CH2, C(CH3) and O(CH3) groups of poly(methyl methacrylate). Polymer, 20(6), 705–712.
34. Chapter - III: Spectral Studies INFRARED SPECTROSCOPY by Shodhganga.
35. The C=O Bond, Part IV: Acid Anhydrides Mar 01, 2018 By Brian C. Smith Spectroscopy Volume 33, Issue 3, pg 16–20.
36. Infrared Spectral Interpretation: A Systematic Approach by Brian C. Smith.
37. Chapter 11 - Anhydrides Interpreting Infrared, Raman, and Nuclear Magnetic Resonance Spectra Volume 1, 2001, Pages 205-212.
38. Gupta et al. Application of ATR-FTIR Spectroscopy to Compare the Cell Materials of Wood Decay Fungi with Wood Mould Fungi International Journal of Spectroscopy Volume 2015, Article ID 521938, 7 pages.
39. Handbook of Plastics Analysis edited by Hubert Lobo, Jose V. Bonilla.
40. Viana et al. Infrared Spectroscopy of Anionic, Cationic, and Zwitterionic Surfactants Abstract Advances in Physical Chemistry Volume 2012, Article ID 903272, 14 pages.
41. Tongay et al. Defects activated photoluminescence in two-dimensional semiconductors: the interplay between bound, charged, and free excitons Scientific Reports volume 3, Article number: 2657 (2013).
42. Rahman et al.Size-dependent physicochemical and optical properties of silica nanoparticles March 2009 Materials Chemistry and Physics 114(1):328-332.

43. Giri et al. Intense Ultraviolet-Blue Photoluminescence from SiO2 EmbeddedGe Nanocrystals Preparedby Different Techniques Journal of Nanoscience and Nanotechnology Vol.9, 1–7, 2009.
44. Nishikawa et al. Photoluminescence from defect centers in high-purity silica glasses observed under 7.9-eV excitation Physical review b volume 45, number 2 1 January 1992-II.
45. Glinka et al.Size effect in self-trapped exciton photoluminescence from SiO2-based nanoscale materials physical review b, volume 64, 085421.
46. Sai Gourang Patnaik et al. BIAN Based Electroactive Polymer with De?ned Active Centers asMetal-Free Electrocatalysts for Oxygen Reduction Reaction (ORR) inAqueous and Nonaqueous Media ACS Appl. Energy Mater. XXXX, XXX, XXX-XXX© XXXX American Chemical Society ADOI: 10.1021/acsaem.7b00293ACS Appl. Energy Mater. March 2018.
47. Abadi et al Effects of Annealing Temperature on Infrared Spectra of SiO2 Extracted From Rice Husk J. Ceram. Sci. Tech., 06 [01] 41-46 (2015).
48. Wang et al. Thermal Annealing Effect on Optical Properties of Binary TiO2-SiO2 Sol-Gel Coatings materials ISSN 1996-1944.
49. K. Kenmochi, M. Seike, K. Sato, A. Yanase, and H. Katayama-Yoshida, Jpn. J. Appl. Phys. 43, L934 (2004); K. Kenmochi, V. A. Dinh, K. Sato, A. Yanase, and H. Katayama-Yoshida, J. Phys. Soc. Jpn. 73, 2952 (2004).
50. I. S. Elfimov, A. Rusydi, S. I. Csiszar, Z. Hu, H. H. Hsieh, H.-J. Lin, C. T. Chen, R. Liang, and G. A. Sawatzky, Phys. Rev. Lett. 98, 137202 (2007).
51. Magnetism in C or N-doped MgO and ZnO: density-functional study of impurity pairs Article in Physical Review Letters · December 2010.
52. Werner Vogel: "Glass Chemistry"; Springer-Verlag Berlin and Heidelberg GmbH & Co. K; 2nd revised edition (November 1994).
53. Crystallization of hollow mesoporous silica nanoparticles Chem. Commun., 2015, 51, 4164.
54. G.Kopnov, Z. Vager, and R.Naaman, “New magnetic properties of silicon/silicon oxide interfaces,” Advanced Materials, vol. 19, no. 7, pp. 925–928, 2007.

55. Sol-Gel Science: The Physics and Chemistry of Sol-Gel Processing Book by C. Jeffrey Brinker and George W. Scherer.
56. Tetsuya Homma Properties of Fluorinated Silicon Oxide Films Formed Using Fluorotriethoxysilane for Interlayer Dielectrics in Multilevel Interconnections Homma, T. (1996). Properties of Fluorinated Silicon Oxide Films Formed Using Fluorotriethoxysilane for Interlayer Dielectrics in Multilevel Interconnections. Journal of The Electrochemical Society, 143(3), 1084.
57. Yamazaki et al. The In?uence of Fluorinated Silicon Nitride Gate Insulatoron Positive Bias Stability toward Highly Reliable AmorphousInGaZnO Thin-Film Transistors ECS Journal of Solid State Science and Technology,3(2) Q20-Q23 (2014).
58. Matsumoto Y, Honma K. NH stretching vibrations of pyrrole clusters studied by infrared cavity ringdown spectroscopy J Chem Phys. 2007 Nov 14;127(18):184310.
59. Greve et al. N-H Stretching Excitations in Adenosine-Thymidine Base Pairs in Solution: Base Pair Geometries, Infrared Line Shapes and Ultrafast Vibrational Dynamics J Phys Chem A. 2013 Jan 24; 117(3): 594–606.
60. Biswal et al.Strength of NH···S Hydrogen Bonds in Methionine Residues Revealed by Gas-Phase IR/UV Spectroscopy Biswal, H. S., Gloaguen, E., Loquais, Y., Tardivel, B., & Mons, M. (2012). Strength of NH···S Hydrogen Bonds in Methionine Residues Revealed by Gas-Phase IR/UV Spectroscopy. The Journal of Physical Chemistry Letters, 3(6), 755–759.
61. Ramis et al. Ammonia activation over catalysts for the selective catalytic reduction of NO, and the selective catalytic oxidation of NH 3. An FT-IR study Catalysis Today 28 (1996) 373-380.
62. Sun et al. Direct in situ ATR-IR spectroscopy of structural dynamics of NH4H2PO4 in aqueous solution CrystEngComm, 2013, 15, 7783.
63. Pietralik Z et al. Structure and conformational dynamics of DMPC/dicationic surfactant and DMPC/dicationic surfactant/DNA systems Int J Mol Sci (2013).
64. Trivedi et al. Fourier Transform Infrared and Ultraviolet-Visible Spectroscopic Characterization of Ammonium Acetate and Ammonium Chloride: An Impact of Biofield Treatment Mod Chem appl 2015, 3:3.

65. Tsai et al. Feasibility of rapid quantitation of stratum corneum lipid content by Fourier transform infrared spectrometry Journal of spectroscopy Volume 18, Issue 3, Pages 423-431.
66. Singh et al. Size and shape effects on the band gap of semiconductor compound nanomaterials Journal of Taibah University for Science Volume 12, 2018 - Issue 4.
67. Avinash et al. Effect of particle size on band gap and DC electrical conductivity of TiO2 nanomaterial AIP Conference Proceedings 1728, 020426 (2016).
68. Jorge Mejia et al. Are stirring and sonication pre-dispersion methods equivalent for in vitro toxicology evaluation of SiC and TiC? J Nanopart Res (2012) 14:815.

Chapter 5: Synthesis of doped SiO_2 nanoparticles.

5.1 Introduction.

As we know that vacancies and defects are somewhat correlated to magnetic properties of nanoparticles [1-8], we can induce these defects by artificially creating vacancies or introducing interstitials. The dopants will be Al, Mg, and Li. In the case of SiO_2 NP (440nm) doping with Al is done both on the surface and in bulk.

5.2 Synthesis of 2% bulk & surface doped SiO_2 NP (440nm).

We've used the same protocol as was followed for the synthesis of undoped nanoparticles [9] except making slight modifications to dope the nanoparticles [10-16]. The solution A was prepared by mixing 18.75 mL ethanol, 1.22 mL TEOS & 0.042 g of $Al(NO_3)_3.9H_2O$. The solution B was prepared by mixing 3.5 mL NH_4OH (25% in H_2O) 21.5 mL ethanol & 5 mL H_2O. The solution A was then added dropwise in Solution B with the rate of less than 0.05 mL/sec. The onset of turbidity was a clear indication of the formation of silica nanoparticles. The colloidal solution thus formed was allowed to age for 48 hours after which it was centrifuged and washed six times with ethanol after each runs and then dried at 60^0C in a hot oven overnight.

The synthesis of 2% surface Al-doped nanoparticles was done with the same method as discussed earlier but with a difference that 0.042 g of $Al(NO_3)_{3.}9H_2O$ was dissolved in sufficient amount of ethanol (0.1-0.5 ml) and was added after completely adding solution A in solution B [17-20]. The reason for adding it later in the reaction was to deposit most of the defect on the surface of nanoparticles contrary to the bulk case.

5.3 Synthesis of 5% Li, Mg & Al-doped SiO_2 NP (200nm).

The procedure employed was similar to the synthesis of SiO_2 NP (200nm) [21]. Required amount of TEOS & required amount of $Al(NO_3)_{3.}9H_2O/Mg(NO_3)_2/LiNO_3$ was added in 30 mL of EtOH and stirred vigorously for 5-10 minutes then it was allowed to sonicate for 10 minutes after which 1 mL distilled water was added, and the solution was again stirred for 5-10 minutes. Then it was kept for sonication for 90 minutes, and then 2 mL of NH_4OH was added accompanied by stirring. The turbidity after 3-4 minutes was apparent and was a clear indication of the formation of nanoparticles. The turbid solution thus obtained was sonicated for 3 hours and aged overnight. After aging, it was centrifuged and washed several times with ethanol and dried for 1-2 days at 60^0 C in a hot air oven.

5.4 Characterization.

XRD, FT-IR, SEM, Diffuse reflectance UV & SQUID are the techniques employed in characterizations. The XRD of all the doped particles shows amorphous nature as can be seen in figs 5.1-5.2.

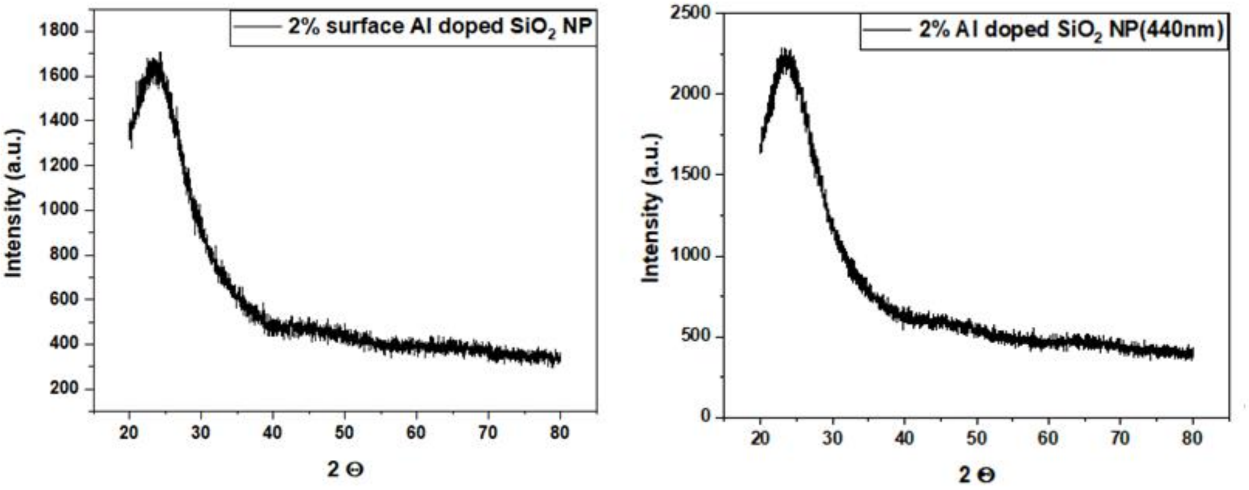

fig 5.1 XRD of 2% surface and bulk-doped (Al) SiO_2 NP (440nm).

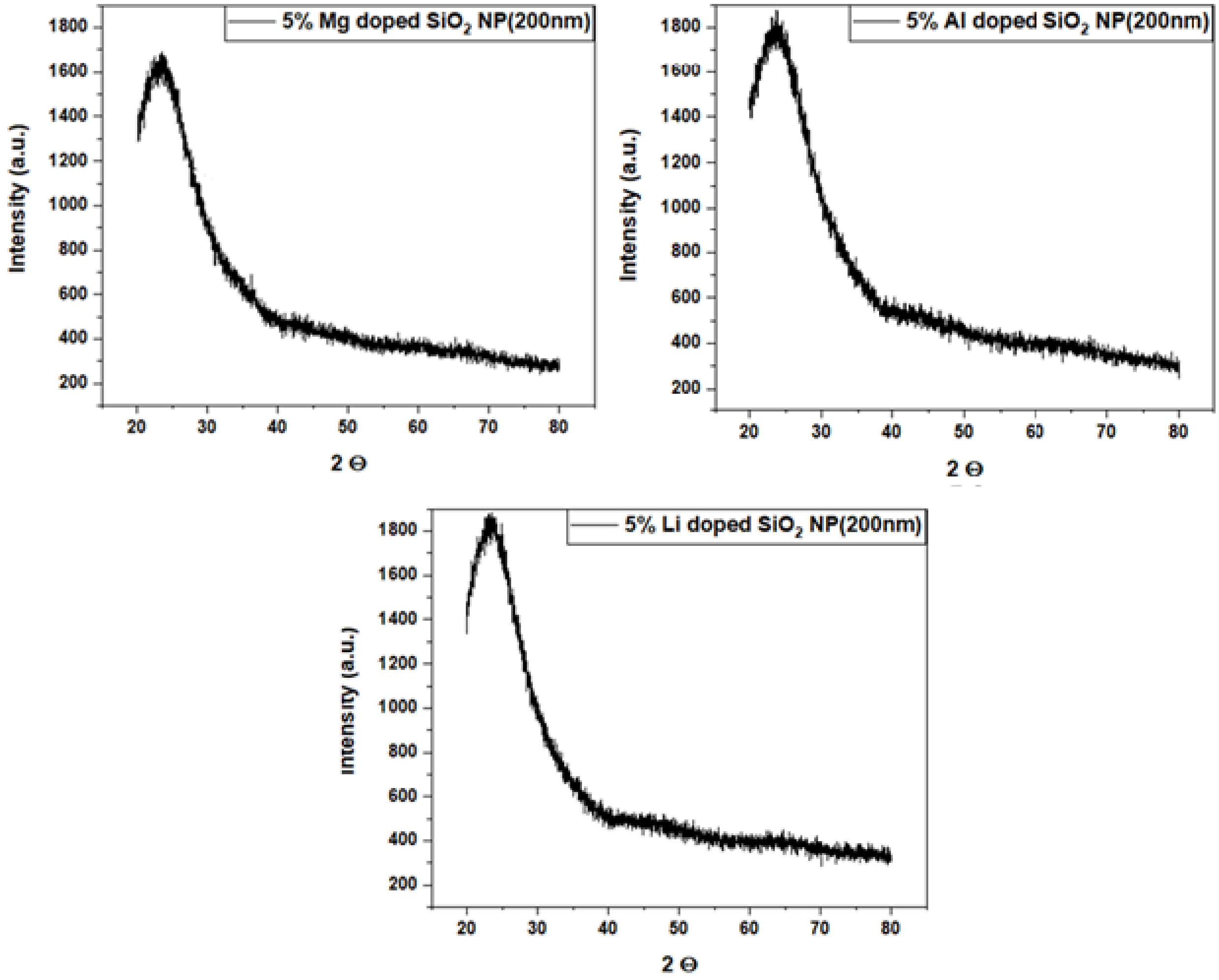

Error! No text of specified style in document. ***fig 5.2 XRD of 5% Mg, Al, Li-doped SiO_2 NP (200nm) respectively.***

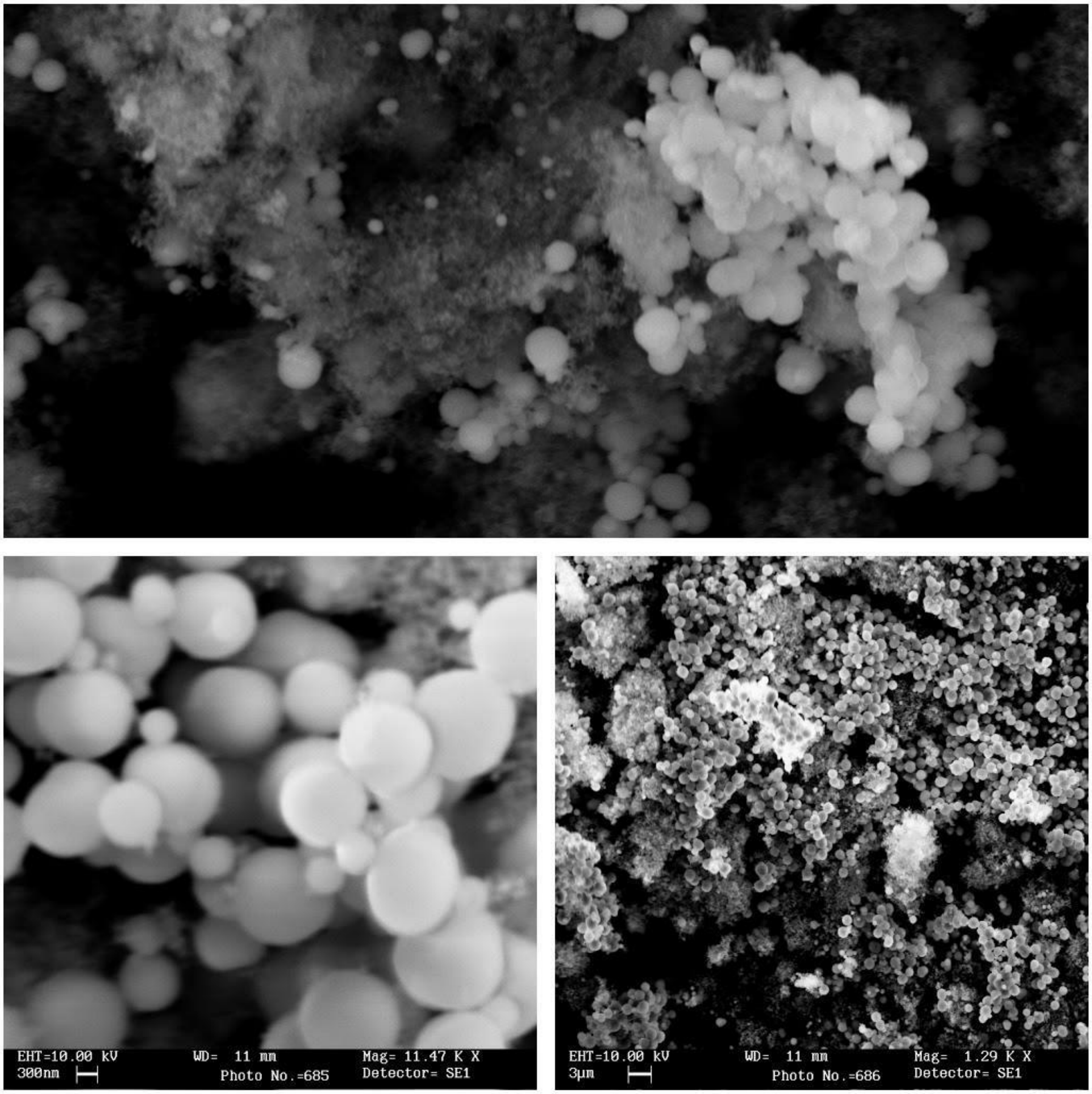

fig 5.3 SEM images of 2% Al-doped SiO_2 Nanoparticles.

As can be seen in figs 5.3-5.5 the nanoparticles are not monodispersed and uniform in size. The dopant salts which are added may be interfering with nuclei formation and growth. The SEM of both 5% Mg & 5% Li-doped SiO_2 NP (200nm) show non-spherical particles too in majority. The EDS (Energy dispersive x-ray spectroscopy) shows the presence of Mg peak (fig 5.7, Table 5.1). Even though elemental mapping shows presence of Mg, there is no clear way to tell if Mg cation is effectively doped into nanoparticles (fig 5.6).

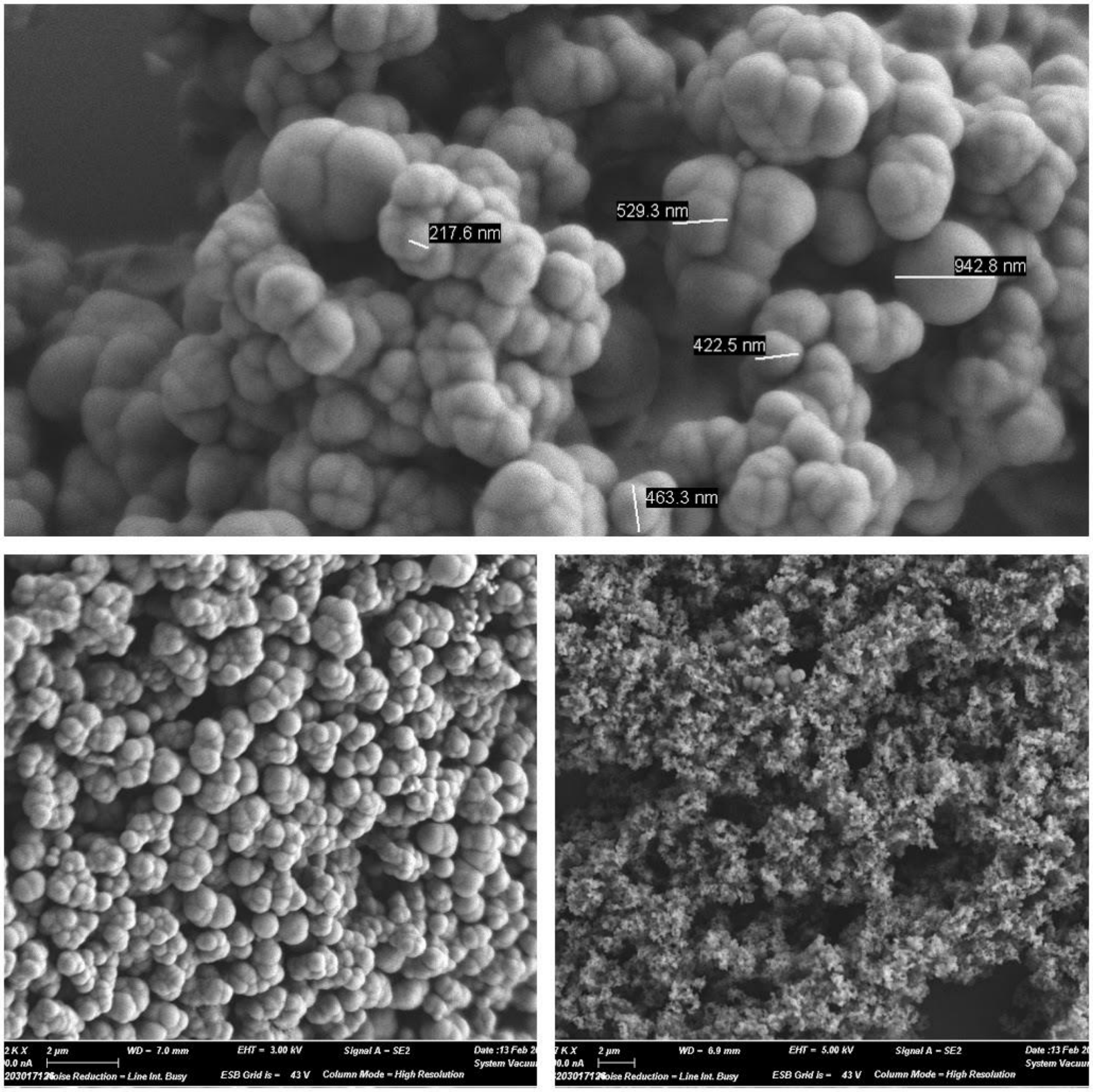

fig 5.4 SEM of 5% Li doped SiO_2 NP(200nm).

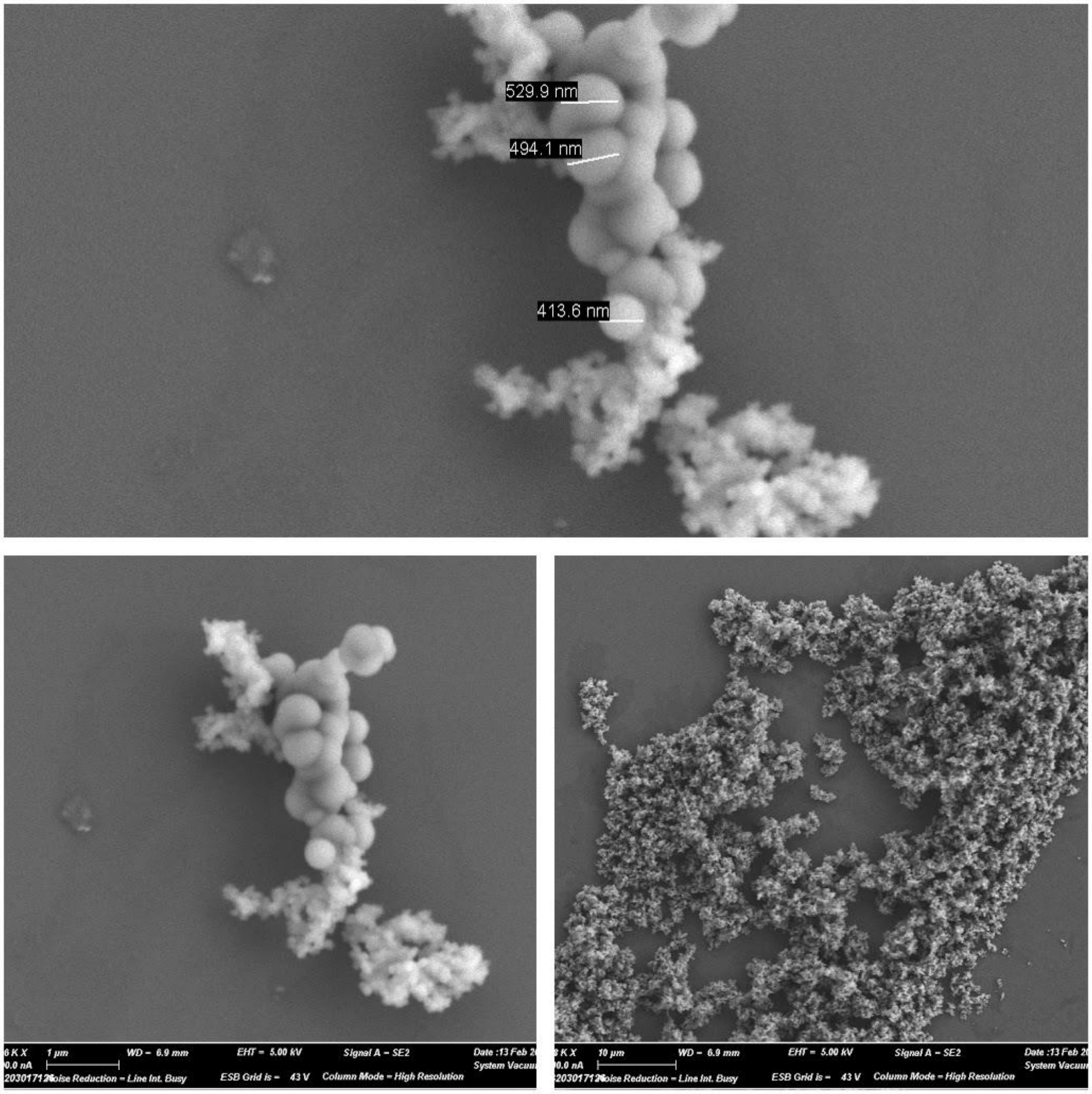

fig 5.5 SEM of 5% Mg-doped SiO_2 NP (200nm).

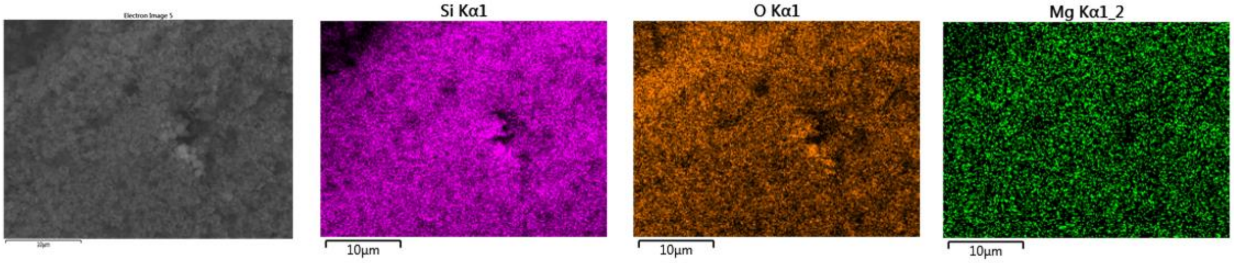

fig 5.6 Elemental Mapping of 5% Mg-doped SiO2 NP (200nm).

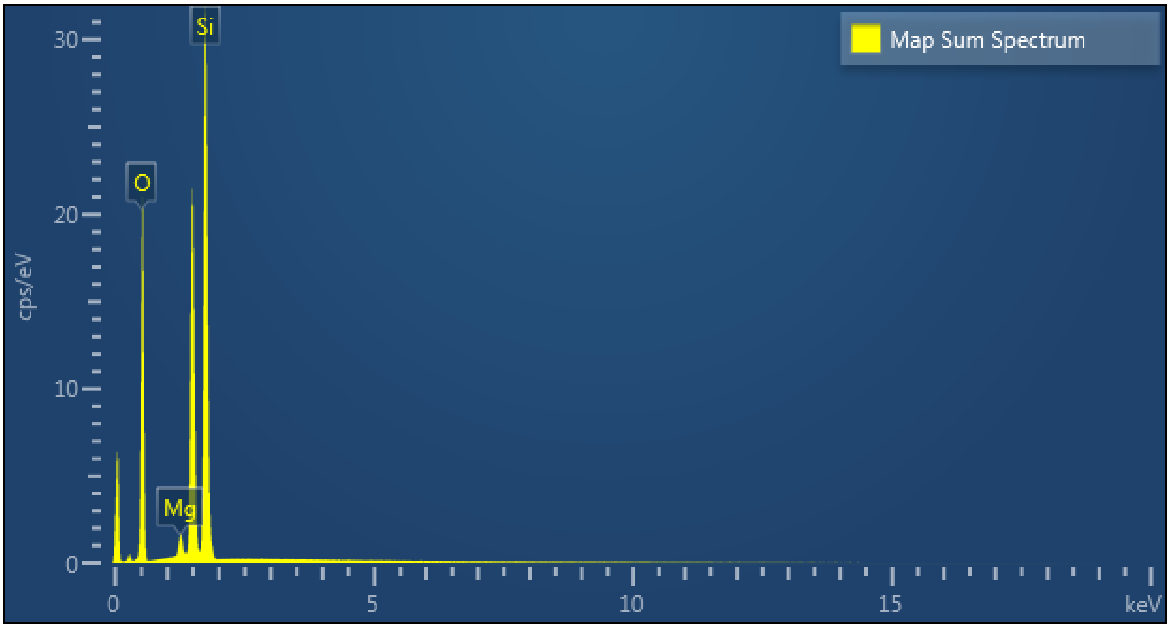

fig 5.7 EDS of 5% Mg-doped SiO2 NP (200nm).

Element	Line Type	Apparent Concentration	k Ratio	Wt%	Wt% Sigma	Standard Label	Factory Standard	Standard Calibration Date
O	K series	36.46	0.12268	59.00	0.12	SiO2	Yes	
Mg	K series	1.08	0.00714	2.42	0.04	MgO	Yes	
Si	K series	20.07	0.15905	38.57	0.12	SiO2	Yes	
Total:				100.00				

Table 5.1 The result of EDS of 5% Mg doped SiO_2 NP (200nm).

M vs. H were measured to see the effect of doping on ferromagnetism. The higher magnetic moment of bulk Al-doped SiO_2 NP than the surface Al-doped SiO_2 NP may be because of more efficient doping or incorporation of the Al ions in the former case (fig 5.8). Since when we dissolve the salt of dopant in solution before the addition of TEOS; the dopant ions are already present in the solvent and can be incorporated in the nanoparticle in high numbers as compared to adding dopant salt after adding TEOS. M vs. H data (fig 5.9) of both Li & Mg-doped SiO_2 NP (200nm) shows six times less magnetic saturation than un-doped SiO_2 NP (200nm). This suggests that doping hasn't occurred efficiently.

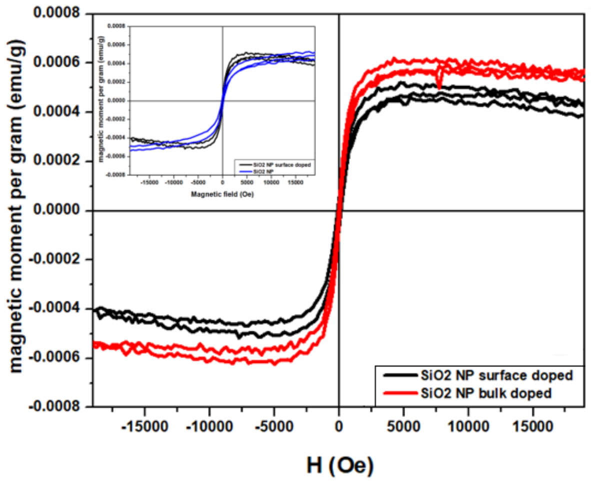

fig 5.8 M vs. H of surface & bulk Al-doped SiO_2 NPs (440nm). The box inside shows that surface Al doped & undoped particles have nearly the same magnetic moment.

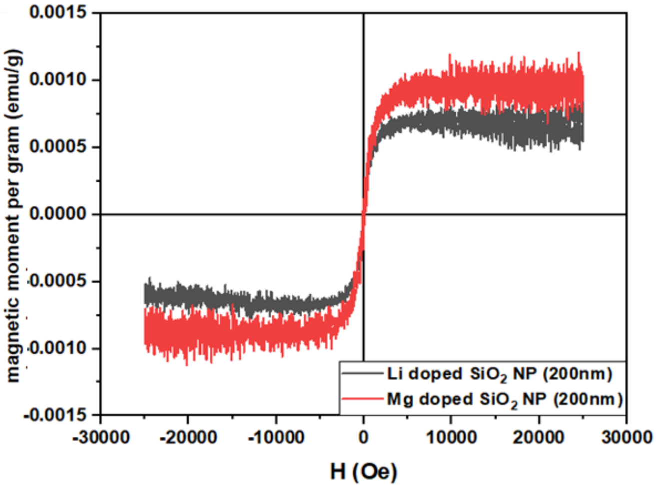

fig 5.9 M vs. H data of both Li & Mg-doped nanoparticles.

5.5 Results & Discussions.

Defects are induced more efficiently in the case of bulk Al-doped SiO_2 NP (440nm) than surface doped one. By looking at fig 5.9 & figs 5.4-5.6, we speculate that Li & Mg doping is too much inefficient meaning there is too less incorporation of dopant ions in nanoparticles. It seems that to enhance the magnetic properties of the nanoparticles; up to 10-15%, Al doping should be employed that too in sub 100nm particles to find their applications in the biomedical field [22].

References

1. Vladislav G. Il'ves, Michael G. Zuev, and Sergey Yu. Sokovnin Hindawi Publishing Corporation Journal of Nanotechnology Volume 2015, Article ID 417817, eight pages.
2. G.Kopnov, Z. Vager, and R.Naaman, "New magnetic properties of silicon/silicon oxide interfaces," Advanced Materials, vol. 19, no. 7, pp. 925–928, 2007.
3. Li et al. Rise and fall of defect induced ferromagnetism in SiC single crystals Applied Physics Letters 98, 222508 (2011).

4. A. Sundaresan, N. Rangarajan, R. Bhargavi, U. Siddesh C. N. R. Rao, Ferromagnetism as a universal feature of nanoparticles of the otherwise nonmagnetic oxides, Phys. Rev. B 74, 161306 (R) (2006).

5. A. Sundaresan and C. N. R. Rao, Ferromagnetism as a universal feature of nanoparticles, Nanotoday 4, 96- 106 (2009).

6. Nitesh Kumar, D. Sanyal, and A. Sundaresan, Defect Induced ferromagnetism in MgO nanoparticles studied by optical and positron annihilation spectroscopy, Chem. Phys. Lett., 477, 360 – 364 (2009).
7. A. Sundaresan and C. N. R. Rao, Implications and consequences of ferromagnetism universally exhibited by inorganic nanoparticles, Solid State Commun., 149, 1197 – 1200 (2009).
8. L. S. Panchakarla, Y. Sundarayya, S. Manjunatha, A. Sundaresan and C. N. R. Rao, On the defect origin of room-temperature magnetism exhibited by metal oxide nanoparticles, ChemPhsChem., 11, 1673 -1679 (2010).
9. X. Wang, C. Zhen, X. Liu et al., “A new hole-bridge structure based on a SiO2 nanoarray and its ferromagnetism,” Colloids and Surfaces A: Physicochemical and Engineering Aspects, vol.446, pp. 151–155, 2014.
10. Moran et al. Synthesis and Characterization of Lanthanide-Doped Silica Microspheres Langmuir 2001, 17, 8376-8379.
11. Kim et al. Kim, M. Y., Chu, M. C., Cho, S. J., & Bae, D. S. (2010). Synthesis and Characterization of Ga Doped SiO2 Nanoparticles by a Reverse Micelle and Sol–Gel Processing. Journal of Nano Research, 11, 151–157.
12. Park et al. Synthesis and Characterization of Erbium-doped SiO2 Nanoparticles Fabricated by Using Reverse Micelle and Sol-gel Processing Journal of the Korean Physical Society, Vol. 61, No. 9, November 2012, pp. 1481~1484.
13. Bae et al. Fabrication of phosphor thin film by surface modification for photonics eccm15 - 15th european conference on composite materials, Venice, Italy, 24-28 June 2012.
14. Aware et al. Synthesis, characterization and photocatalytic applications of Zn-doped TiO2 nanoparticles by sol–gel method.

15. Kim et al. Synthesis and Characterization of Yttrium-doped Core-Shell SiO2 Nanoparticles by Reverse Micelle and Sol-gel Processing Journal of the Korean Ceramic Society Vol. 45, No. 9, pp. 512~517, 2008.
16. Petit et al. Luminescence properties of Eu3+ or Dy3+/Au co-doped SiO2 nanoparticles Materials Letters 61 (2007) 2879–2882.
17. Koao et al. Synthesis and characterization of Ce3 + doped silica (SiO2) nanoparticles Journal of Luminescence 131 (2011) 1249–1254.
18. Koao et al. Effects of aluminum co-doping on photoluminescence properties of Ce3+-doped SiO2 glasses JOURNAL OF RARE EARTHS, Vol. 28, Spec. Issue, Dec. 2010, p. 206.
19. Kim et al. Preparation and Characterization of the Antibacterial Cu Nanoparticle Formed on the Surface of SiO2 Nanoparticles J. Phys. Chem. B 2006, 110, 24923-24928.
20. Kawashita et al. Preparation of antibacterial silver-doped silica glass microspheres. Journal of Biomedical Materials Research, 66A (2), 266–274.
21. Synthesis of Ultrafine SiO2 NanoparticlesThrough Ultrasonication-Assisted Sol–Gel Technique Journal of Advanced Physics Vol. 3, pp. 1–4, 2014.
22. Applications of magnetic nanoparticles in biomedicine J. Phys. D: Appl. Phys. 36 (2003) R167–R181.

Chapter 6: Magnetism in $BaTiO_3$.

6.1 Introduction.

The materials that exhibit both magnetic & electric order are among the class of materials called multiferroic materials [1-10]. These types of materials are extensively used for data storage applications by assigning two opposing ferroelectric dipole moments or magnetic dipole moments as 0's and 1's [11]. They also find applications in magnetoelectric sensor, data storage, multifunctional materials, energy saving technologies & memory devices [12-17]. The multiferroicity till date has been found in boracites, fluorides, manganites of perovskites structures [18]. It is known that ferroelectric properties of $BaTiO_3$ nanoparticles diminish as the size reduces while oxygen vacancies & defects induced ferromagnetism increases [19]. But there are intermediate sizes at which these two properties can be successfully tuned making the $BaTiO_3$ nanocrystallites multiferroic [19]. The $BaTiO_3$ nanoparticles are thus synthesized. The samples are also annealed at several temperatures. The cubic $BaTiO_3$ nanoparticles (non-ferroelectric) were also synthesized. SEM, XRD, EDS, SQUID characterizations were also done.

6.2 Synthesis of cubic $BaTiO_3$ nanoparticles.

The cubic $BaTiO_3$ was prepared by precipitation reaction [20]. 1g of NaOH was added to 5 mL of 0.2 mmol/L $Ba(NO_3)_2$ solution with continuous stirring and heating in an oil bath. After the temperature of the oil bath reached 80^0C, 0.3 mL titanium isopropoxide was added, and the resultant white colored turbid solution was kept for stirring for 24 hours after which it was centrifuged and washed with distilled water 3 times after each run. The as-obtained powder was later dried in a hot air oven.

6.3 Synthesis of tetragonal $BaTiO_3$ nanoparticles.

Tetragonal $BaTiO_3$ nanoparticles were synthesized by the polymeric precursor process [19]. 180 mL ethanol & 60 mL acetic acid was mixed to which 0.88 mL of titanium isopropoxide ($Ti(OR)_4$) was added and kept for stirring for 2 hours to form solution A. To prepare solution B 0.592 g $Ba(CO)_3$ & 2.3054 g citric acid were dissolved in 20 mL de-ionized water. Then after completion of stirring solution A, solution B was added and immediately after the addition of solution B poly vinyl alcohol (PVA) solution (2.5 g PVA dissolved in 96.35 mL) was added. The onset of turbidity was an indication of the formation of nanoparticles. The solution was then centrifuged and was dried in a hot air oven at 60^0C for more than 1-2 days. And the dried powder was calcined in air at 700^0C for 1 hour to remove the organic materials.

6.4 Characterization.

The XRD peaks are without any impurity as evident in fig 6.1. tetragonal $BaTiO_3$ was annealed at several temperatures. The annealing temperature is indicated as BTO700 (for 700^0C) & so on for different temperatures. The EDS as well as elemental mapping of both BTO 1000 & BTO 1300 confirms the presence of Ba, Ti & O as shown in figs 6.4-6.5 & figs 6.7-6.8 & tables 6.1 & 6.2. The SEM of BTO1300 shows increased in particles size (than BTO1000) which is due to the annealing.

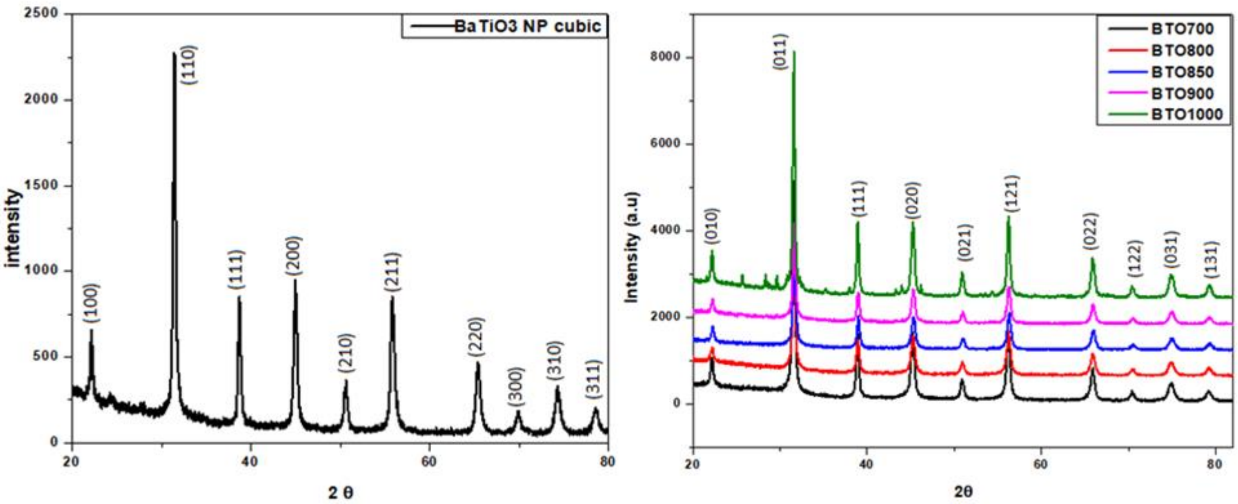

fig 6.1 XRD of Cubic & Tetragonal BaTiO3. Latter was annealed at several temperatures.

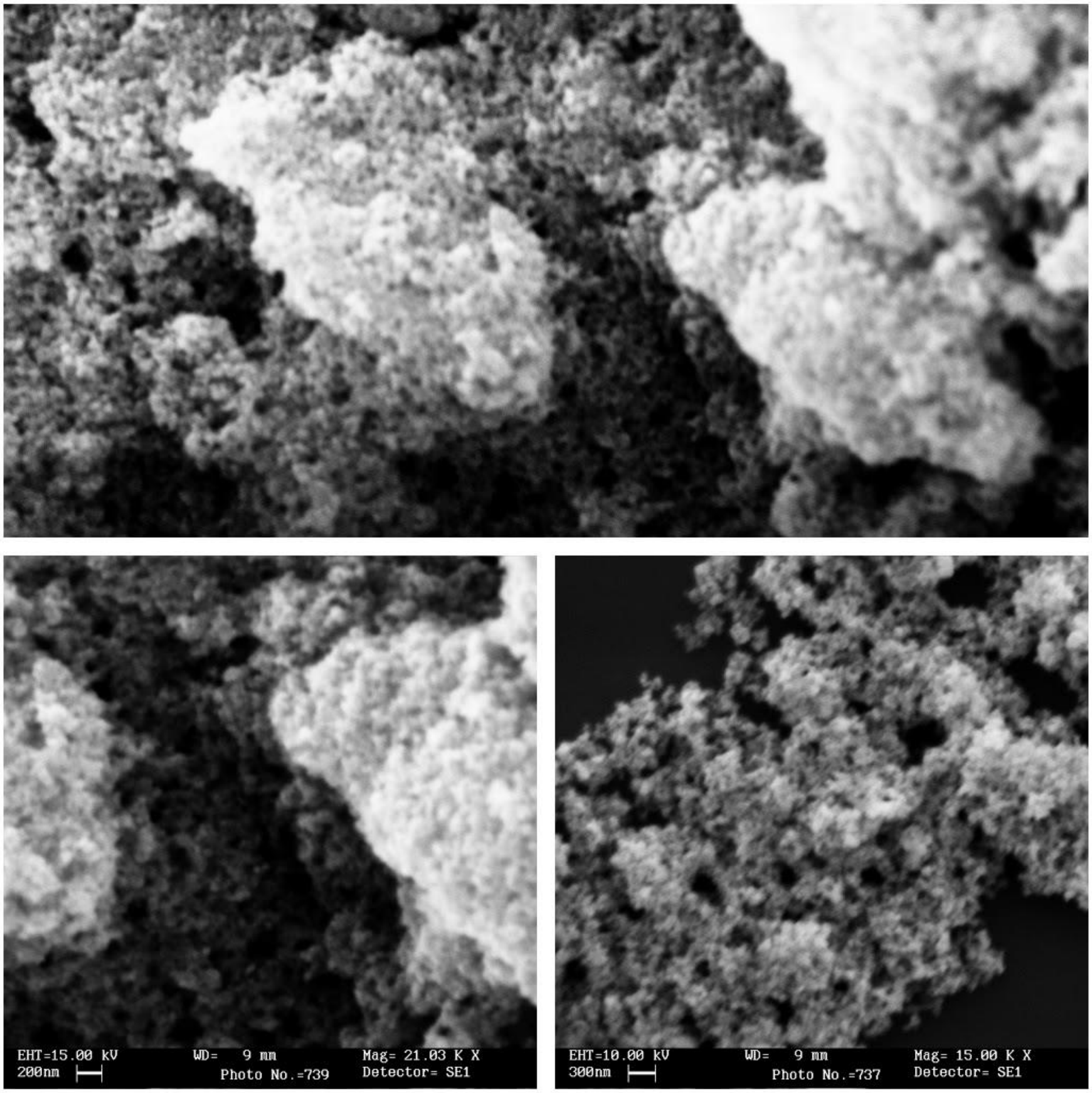

fig 6.2 SEM of BTO 700.

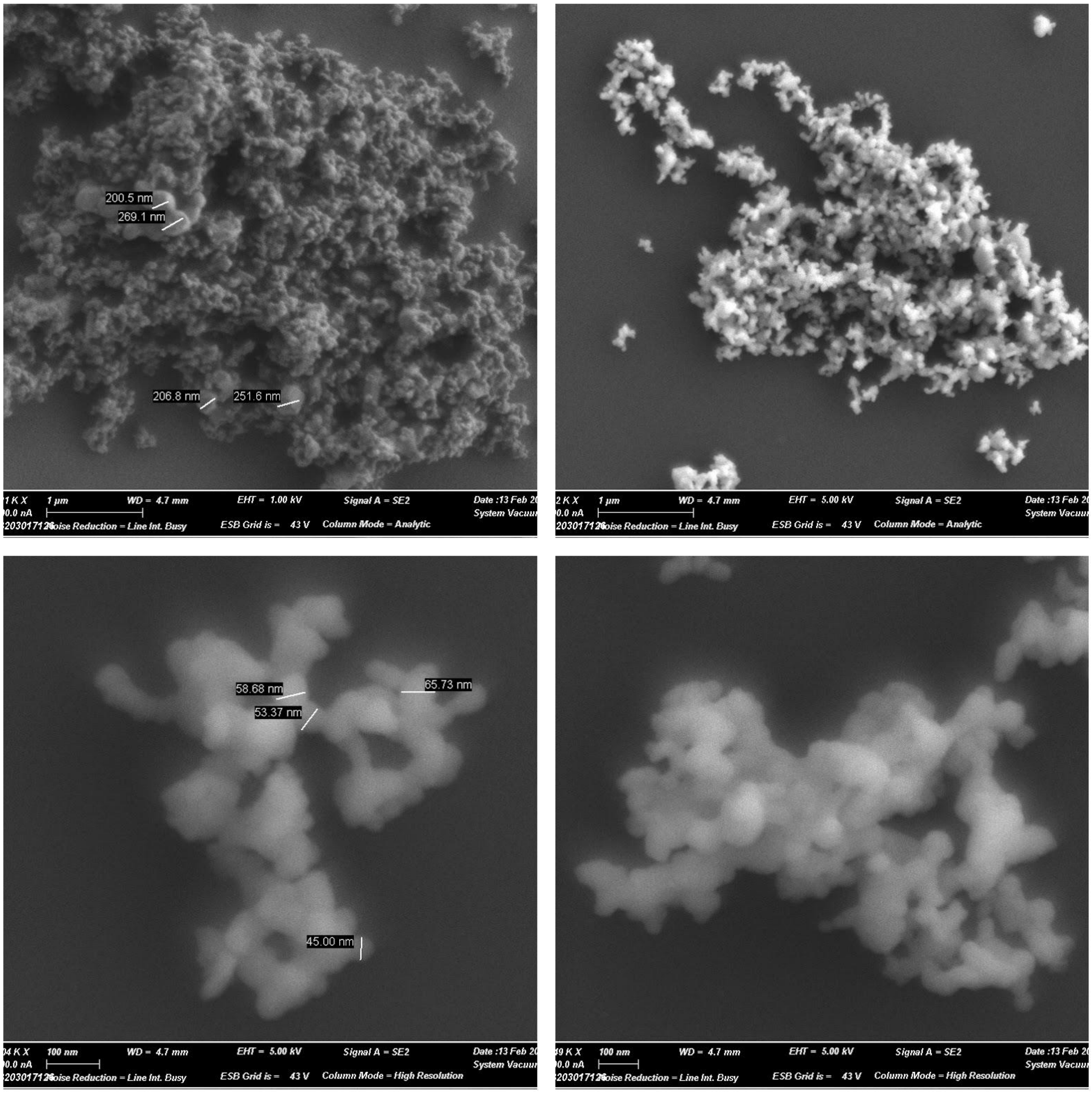

fig 6.3 SEM images of BTO 1000.

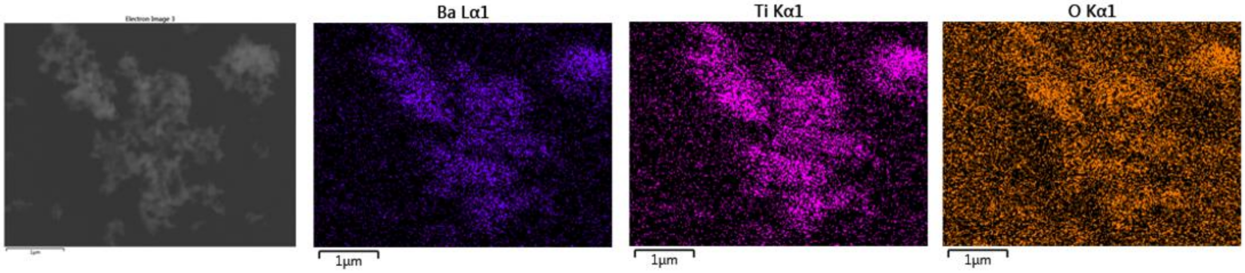

fig 6.4 Elemental mapping of BTO 1000.

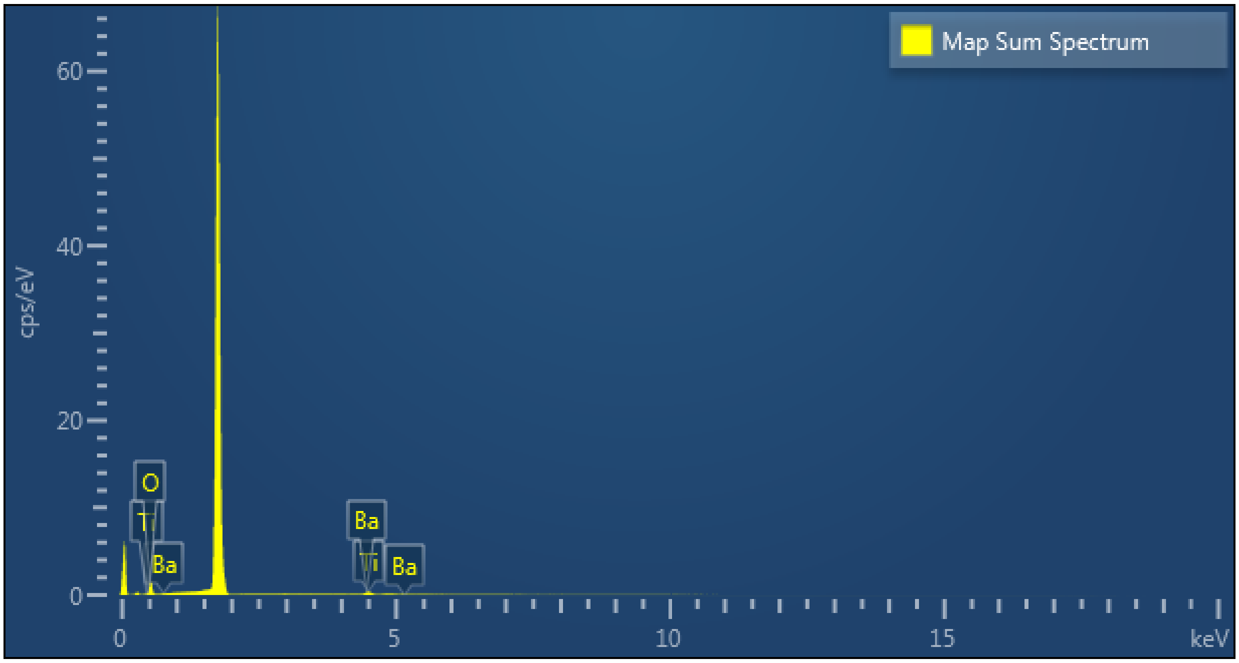

fig 6.5 EDS of BTO 1000.

Element	Line Type	Apparent Concentration	k Ratio	Wt%	Wt% Sigma	Standard Label	Factory Standard	Standard Calibration Date
O	K series	2.93	0.00987	70.27	0.82	SiO2	Yes	
Ti	K series	0.27	0.00272	9.79	0.42	Ti	Yes	
Ba	L series	0.53	0.00496	19.94	0.83	BaF2	Yes	
Total:				100.00				

Table 6.1 Elemental composition (by wt%) of BTO 1000.

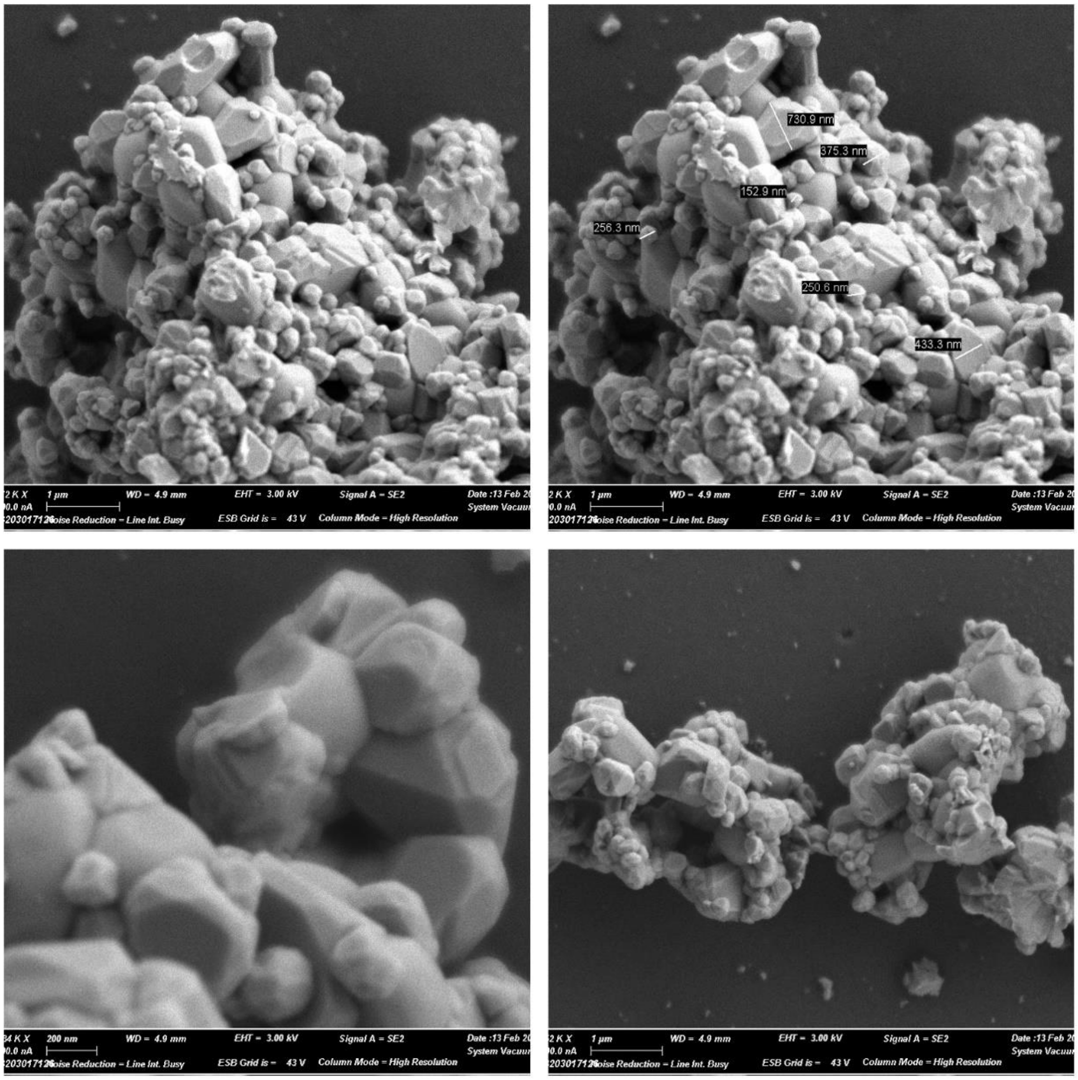

fig 6.6 SEM of BTO 1300.

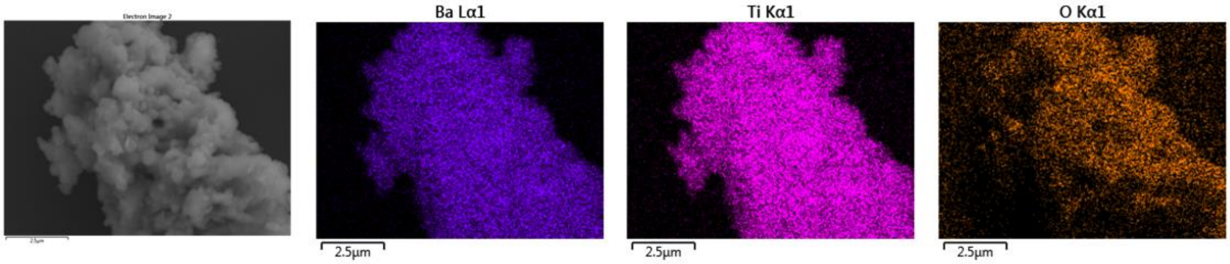

fig 6.7 Elemental Mapping of BTO 1300.

Element	Line Type	Apparent Concentration	k Ratio	Wt%	Wt% Sigma	Standard Label	Factory Standard	Standard Calibration Date
O	K series	5.36	0.01803	28.54	0.33	SiO2	Yes	
Ti	K series	5.00	0.05005	21.62	0.23	Ti	Yes	
Ba	L series	11.05	0.10348	49.83	0.33	BaF2	Yes	
Total:				100.00				

Table 6.2 Elemental composition (by wt%) of BTO 1300.

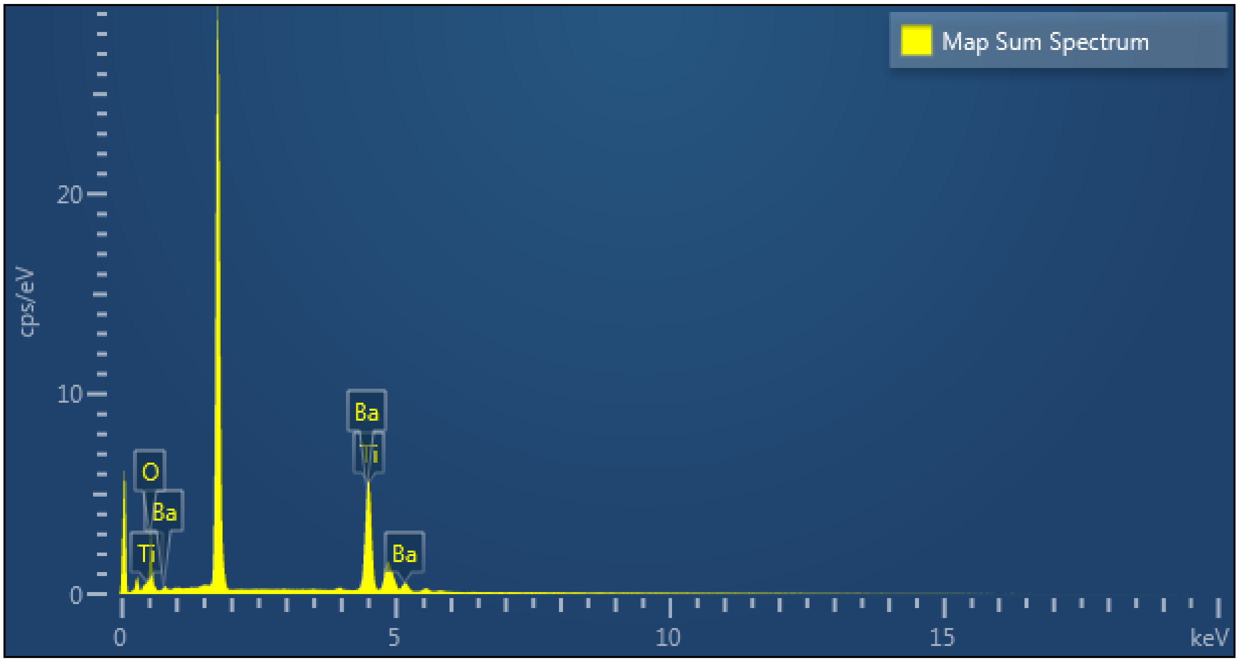

fig 6.8 EDS of BTO 1300.

As can be seen in fig 6.9 the tetragonal $BaTiO_3$ shows much more saturation magnetic moment than the cubic $BaTiO_3$. The saturation of both cubic & tetragonal nanoparticles are 0.0004 emu/g & 0.007 emu/g respectively. Annealing has reduced the magnetic moment by seven times.

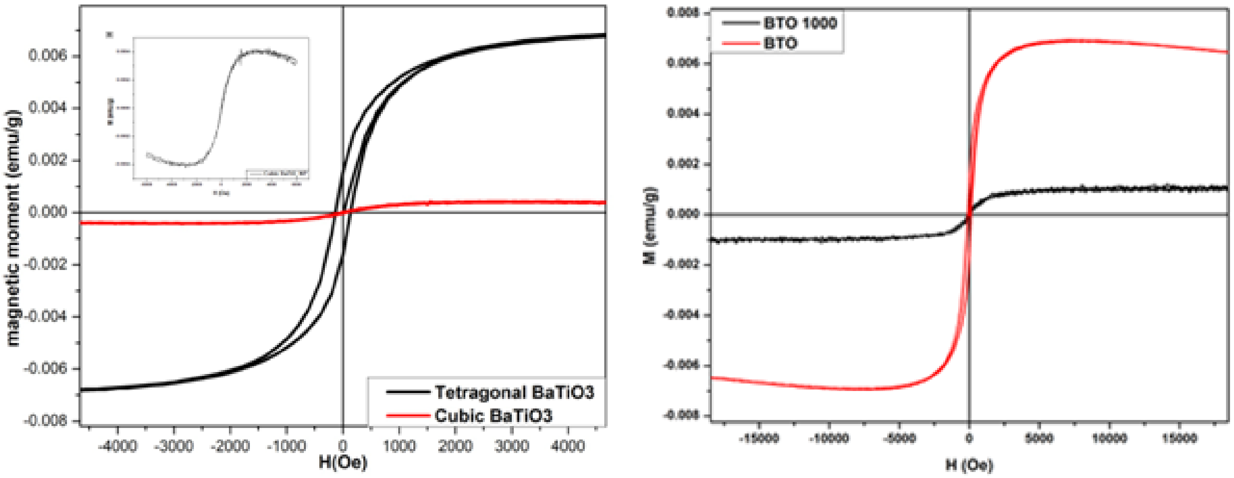

fig 6.9 M vs. H data of both Tetragonal & Cubic $BaTiO_3$ (left). The inside box shows M vs. H of cubic $BaTiO_3$. While on right M vs. H data before & after annealing is shown.

SANS (small angle neutron scattering) data of $BaTiO_3$ nanoparticles is shown in fig 6.10. The data taken is I(Q) vs. Q. I is intensity & Q is the wave vector. If the nanoparticles were simple the, I(Q) vs. Q would have been a straight line (Porod's law) [21], but it's not the case. The line is humped. The hump is due to magnetic scattering. Magnetic scattering is the scattering due to the interaction of the magnetic moment of neutrons with the electronic moments in the sample [22]. The humped line is fitted to a spherical shell model which indicates that the core is nonmagnetic and the shell is magnetic. Thus the magnetism indeed exists on the nanoparticle surface. This is in agreement with the previous studies [23-29].

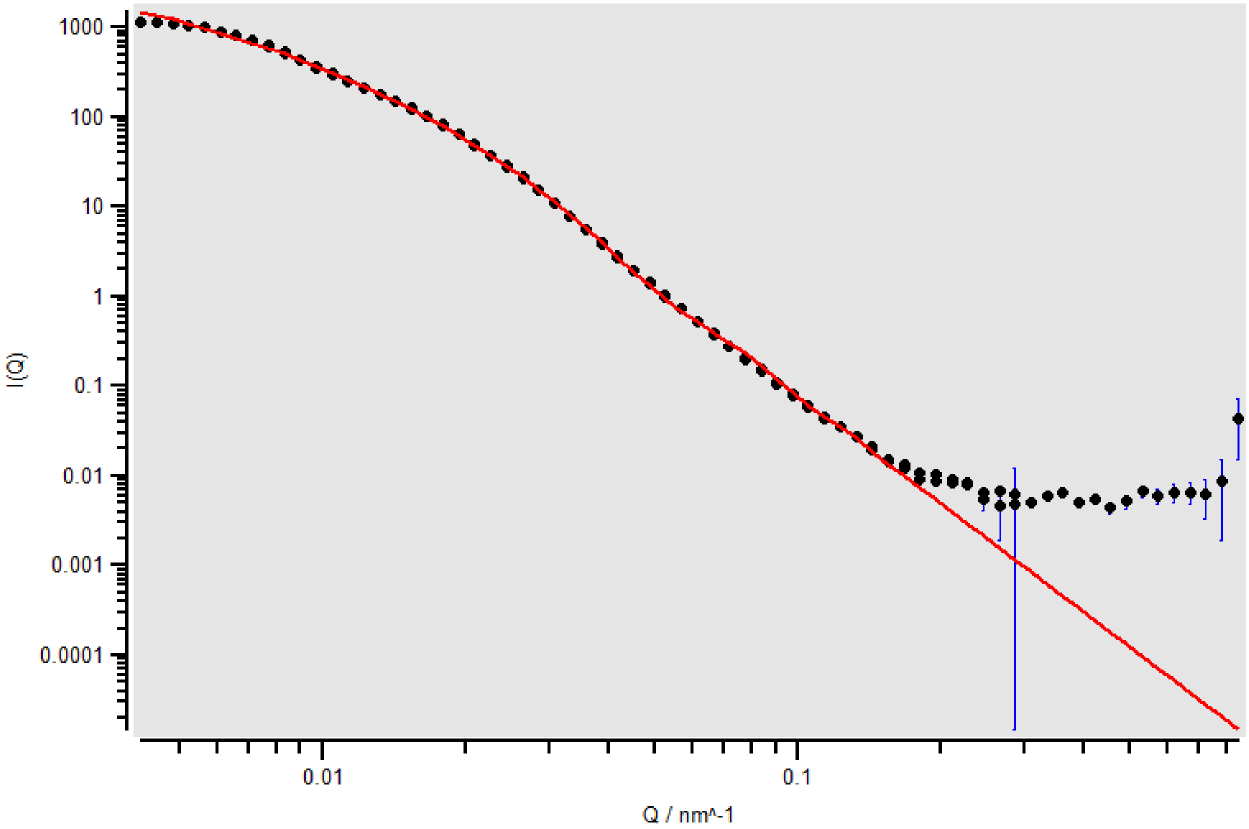

fig 6.10 I vs. Q data of $BaTiO_3$ Nanoparticles fitted as a Spherical Core Shell Model.

The particle size distribution is a lognormal distribution (fig 6.12) with an average core of 44.2 nm & the average shell of 10 nm. The shell's 10 nm size corresponds to magnetic order along with its actual physical size.

fig 6.11 The structure of $BaTiO_3$ can be visualized as dark nonmagnetic core (99nm) and outer shell exhibiting magnetic order (fuzzy surface).

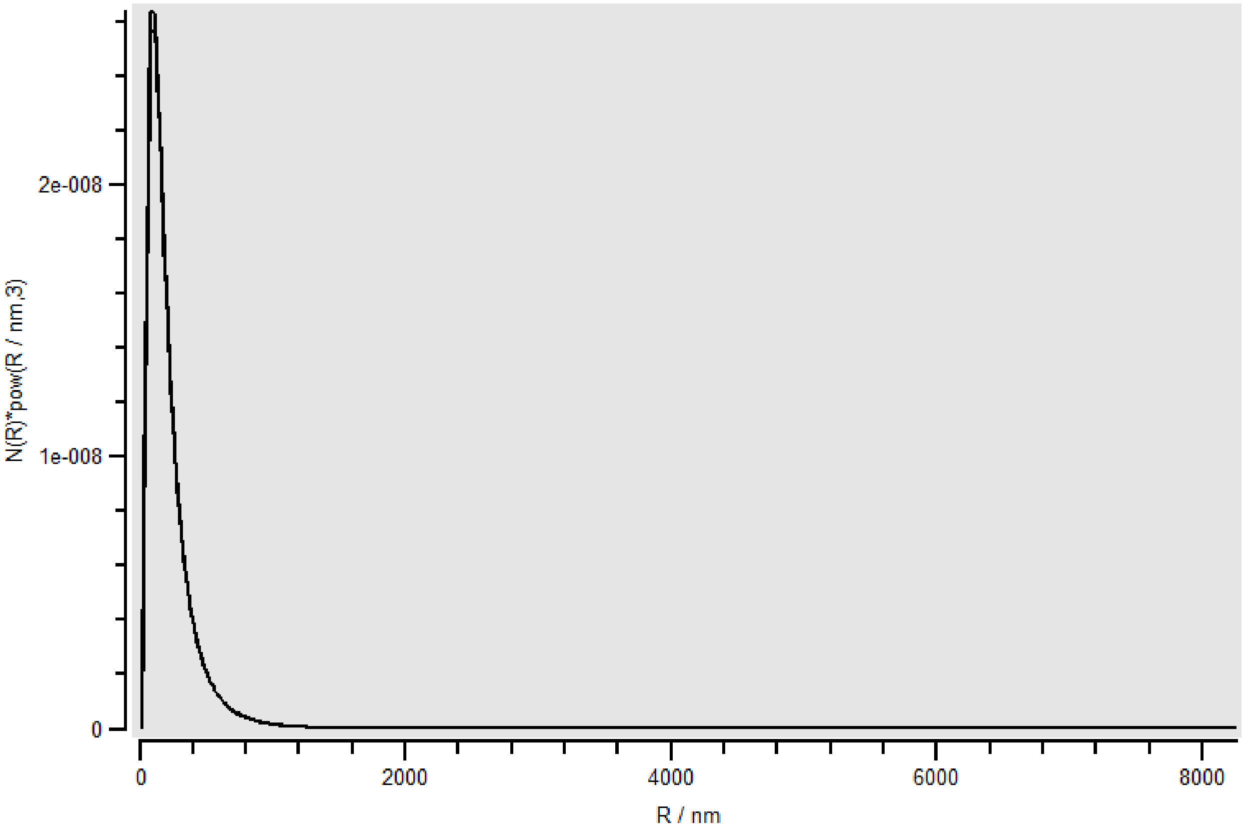

fig 6.12 Lognormal distribution of the core size of nanoparticles.

6.5 Results & Discussions.

The as-synthesized Tetragonal $BaTiO_3$ nanoparticles show nearly seven times more saturation than that of previously reported [19] although the same synthesis route was followed. The reason for this may be due to annealing carried out in the air rather than oxygen (the latter may have been detrimental to magnetic moment). The tetragonal $BaTiO_3$'s higher magnetic moment than the cubic $BaTiO_3$ may be due to its more specific surface area than cubic $BaTiO_3$. The tetragonal $BaTiO_3$ is stable until 1000^0 C of heating. The ferromagnetism (in tetragonal $BaTiO_3$) has originated from the surface as can be seen from the analysis of SANS data. The annealing in the air brings down the magnetic moment which may be due to a decrease in concentration of oxygen vacancies.

References

1. The evolution of multiferroics Nature Reviews Materials volume 1, Article number: 16046 (2016).
2. W. Eerenstein et al. Multiferroic and magnetoelectric materials Nature volume 442, pages 759–765 (17 August 2006).
3. G. A. Smolenskii, I. Chupis, Sov. Phys. Usp. 25, 475 (1982).
4. E. K. H. Salje, Phase Transitions in Ferroelastic and Co-elastic Crystals (Cambridge Univ. Press, Cambridge, 1990).
5. Zheng et al. Multiferroic BaTiO3-CoFe2O4 Nanostructures Science 30 Jan 2004: Vol. 303, Issue 5658, pp. 661-663.
6. Nan et al. Multiferroic magnetoelectric composites: Historical perspective, status, and future directions Journal of Applied Physics 103, 031101 (2008).
7. Fiebig M, Eremenko V V and Chupis I E (ed) 2004 Magnetoelectric Interaction Phenomena in Crystals.
8. Cheong, S.-W. & Mostvoy, M. Multiferroics: A magnetic twist for ferroelectricity. Nature Mater. 6, 13–20 (2007).
9. Gajek et al. Tunnel junctions with multiferroic barriers Nature Materials volume 6, pages 296–302 (2007).
10. N. Hur et al. Electric polarization reversal and memory in a multiferroic material induced by magnetic fields Nature volume 429, pages 392–395 (27 May 2004).
11. Multiferroics: Past, present, and future Phys. Today 63(10), 38 (2010).
12. Khomskii Trend: Classifying multiferroics: Mechanisms and effects Physikalisches Institut, Universität zu Köln, Zülpicher Strasse 77, 50937 Köln, Germany March 9, 2009.
13. Achary et al. 4 - Multiferroic Materials Functional Materials Preparation, Processing and Applications 2012, Pages 155-191.
14. Ma et al. Recent Progress in Multiferroic Magnetoelectric Composites: from Bulk to Thin Films Advanced Materials 04 February 2011.
15. A P Pyatakov et al. Volume 55 (2012) Number 6 Pages 557–581 Physics-Uspekhi.
16. Priya et al. Recent advances in piezoelectric and magnetoelectric materials phenomena Composite Magnetoelectrics, 2015.

17. J. F. Scott Multiferroic memories Nature Materials volume 6, pages 256–257 (2007).
18. Multiferroicity: the coupling between magnetic and polarization orders Advances in Physics Vol. 58, No. 4, July–August 2009, 321–448.
19. Mangalam et al. Multiferroic properties of nanocrystalline BaTiO3 Solid State Communications Volume 149, Issues 1–2, January 2009, Pages 1-5.
20. Xinzhou Wu, Zheng Chen, & Zheng Cui. (2013). Low temperature synthesis of cubic BaTiO3 nanoparticles. The 8th Annual IEEE International Conference on Nano/Micro Engineered and Molecular Systems.
21. Introduction to Small-Angle Neutron Scattering and Neutron Reflectometry Andrew J Jackson NIST Center for Neutron Research May 2008.
22. Magnetic neutron scattering Jeffrey W. Lynn NIST Center for Neutron Research, National Institute of Standards and Technology, Gaithersburg, Maryland.
23. A. Sundaresan, N. Rangarajan, R. Bhargavi, U. Siddesh C. N. R. Rao, Ferromagnetism as a universal feature of nanoparticles of the otheriwise nonmagnetic oxides, Phys. Rev. B 74, 161306 (R) (2006).
24. C. Madhu, A. Sundaresn and C. N. R. Rao, Room-temperature ferromagnetism in undoped GaN and CdS semiconductor nanoparticles, Phys. Rev. B 77, 201306 (R) (2008).
25. A. Sundaresan and C. N. R. Rao, Ferromagnetism as a universal feature of nanoparticles,Nanotoday 4, 96- 106 (2009).
26. Nitesh Kumar, D. Sanyal and A. Sundaresan, Defect Induced ferromagnetism in MgO nanoparticles studied by optical and positron annihilation spectroscopy, Chem. Phys. Lett., 477, 360 – 364 (2009).
27. A. Sundaresan and C. N. R. Rao, Implications and consequences of ferromagnetism universally exhibited by inorganic nanoparticles,Solid State Commun., 149, 1197 – 1200 (2009).
28. R. V. K. Mangalam, M. Chakrabrathi, D. Sanyal, A. Chakrabti and A. Sundaresan, Identifying defects in multiferroicnanocrystalline BaTiO3 by positron annihilation techniques,J. Phys. Condens. Mater. 21, 445902 -445906 (2009).
29. A. M. Stoneham, Theory of defects in solids: Electronic structure of defects in insulators and semiconductors, Oxford University Press, Oxford, 2001.

Chapter 7: Conclusion & Outlook.

7.1 Conclusion.

The study to understand the ‘origin of ferromagnetism in otherwise nonmagnetic oxides’ was focused on two systems i.e. nanoparticles of SiO_2 & $BaTiO_3$. In both the cases we are successful in inducing a reasonable amount of magnetic moment i.e. as high as 0.006 emu/g. The SiO_2 system has proven contradictory in case of the mesoporous SiO_2 nanoparticles which show more oxygen vacancies (as seen in photoluminescence spectra) but show lesser magnetic moment than SiO_2 nanoparticles of 440nm size (which exhibits too less oxygen vacancies than mesoporous SiO_2 nanoparticles). SiO_2 nanoparticles with size 200nm show about six times more magnetic moment than those with size of 100nm.The higher magnetic moment in 200nm sized SiO_2 nanoparticles is because of their different mode of syntheses which involved ultrasonication of about 3 hours and 90 minutes. In synthesis of SiO_2 NP (200nm); after the initiation of nuclei formation (i.e. appearance of turbidity of solution) the solution was kept for 3 hours under continuous sonication which has resulted in more oxygen vacancies & defects on the surface of nanoparticles and thus increased the magnetic moment. This result is in agreement with the studies of Jorge Mejia et al. which has compared effect of ultrasonication on nanoparticle surface as opposed to stirring [4].

Doping of Al in SiO_2 nanoparticles proves to be very efficient way to enhance ferromagnetism than that of Li or Mg doping. The latter two cations were harder to incorporate in SiO_2 nanoparticles in first place.

Annealing the nanoparticles decreases oxygen vacancies and thus magnetic moment in both SiO_2 & $BaTiO_3$ cases.

The band gap of SiO_2 nanoparticles decreased after annealing and also with decreasing size.

Small angle neutron scattering (SANS) analysis of $BaTiO_3$ nanoparticles shows that the core is nonmagnetic while the surface has magnetic moments which confirms that the origin of ferromagnetism is indeed due to surface defects.

7.2 Future Work.

The current SANS data of $BaTiO_3$ (taken under incidence of unpolarized neutron beam and in absence of magnetic field) shows only the evidence of presence of magnetic structure. But the same measurements should be done in presence of magnetic field and using polarized neutron source in order to obtain the magnetic structure [1]. Similarly for SiO_2 NP (200nm) the SANS data should be taken in order to analyze its magnetic structure.

The ion beams can be made incident on SiO_2 nanoparticles to induce defects and vacancies and thus enhancing the ferromagnetism.

Since we have succeeded in devitrification of SiO_2 nanoparticles; the anion doping (e.g. C or N) can be tried in order to increase the magnetic moment of SiO_2 nanoparticles (i.e. by inducing pairing interactions between dopants) [2]. Fluorination is another way by which ferromagnetism can be enhanced.

Since SiO_2 NP (200nm) (which was prepared by employing ultrasonication) shows more magnetic moment than SiO_2 NP (100nm) the effect of ultrasonication on the surface of nanoparticles should be studied in more detail using XPS (x-ray photoelectron spectroscopy), TEM (transmission electron microscopy) etc. If the ultrasonication is utilized for the synthesis of sub 100nm nanoparticles the magnetic moment will be highly enhanced.

Muon spin resonance spectroscopy (μSR) which can probe local magnetic moment can be used to investigate this type of ferromagnetism.

References

1. K. Krycka, A. Jackson, C. Dennis Magnetic Structure of Iron Oxide Nanoparticles Using SANS Summer School on Small Angle Neutron Scattering and Neutron Reflectometry NIST Center for Neutron Research.
2. Wu et al. Magnetism in C- or N-doped MgO and ZnO: A Density-Functional Study of Impurity Pairs Phys. Rev. Lett. **105**, 267203 – Published 27 December 2010.

3. Quantum magnetism probed with muon-spin relaxation thesis by Andrew J. Steele University of Oxford.
4. Jorge Mejia et al. Are stirring and sonication pre-dispersion methods equivalent for in vitro toxicology evaluation of SiC and TiC? J Nanopart Res (2012) 14:815.